Reconciling the long-term growth of the Northeastern Tibetan Plateau and the upstream Yellow River profile

Xiang He[1], Xiaoping Yuan[1], Chuanqi He[2], Xianyan Wang[3], and Xiaoming Shen[4]

[1]China University of Geosciences
[2]Massachusetts Institute of Technology
[3]Nanjing University
[4]National Institute of Natural Hazards, Ministry of Emergency Management of China

April 16, 2024

Abstract

The growth history of the Northeastern Tibetan Plateau (NETP) is enigmatic, with debates on when and how the NETP significantly uplifted. Here, we use a numerical landscape evolution model to quantitatively investigate the ˜20 Ma growth history of the NETP by studying the formation history of the upstream Yellow River (UYR). Compared to the observed river profiles, erosion rates, the trend of acceleration time of deformation, and paleo-elevation, our modeling results suggest that the long-term growth history of the NETP consists of an early block uplift (˜20-12 Ma) and a late outward propagation uplift (˜12-0 Ma). Before ˜12 Ma (middle Miocene), the NETP was uplifted via a block growth, with major uplift in the south part. Subsequently, the high (˜5 km) NETP has been uplifted via a northward propagation growth until the present-day time. We further suggest that pure headward erosion unlikely formed the observed river profile of the UYR over the past few million years. Our modeling thus reconciles the long-term outward growth of the NETP and the UYR profile, suggesting a downstream migration of high erosion rates, which is fundamentally different from the headward erosion of small mountain rivers. The downstream propagation of fluvial erosion may commonly occur in the outward-growing plateau on Earth.

Reconciling the long-term growth of the Northeastern Tibetan Plateau and the upstream Yellow River profile

X. He[1], X. P. Yuan[1*], C. Q. He[2], X. Y. Wang[3], and X. M. Shen[4]

[1]Hubei Key Laboratory of Critical Zone Evolution, School of Earth Sciences, China University of Geosciences, Wuhan, China.

[2]Department of Earth, Atmospheric and Planetary Science, Massachusetts Institute of Technology, Cambridge, USA.

[3]School of Geography and Ocean Science, Nanjing University, Nanjing, China.

[4]National Institute of Natural Hazards, Ministry of Emergency Management of China, Beijing, China

[*]Corresponding author: Xiaoping Yuan (yuanxiaoping@cug.edu.cn)

Key Points:

- The long-term growth of the Northeastern Tibetan Plateau is investigated by a landscape evolution model with two growth scenarios.
- The Northeastern Tibetan Plateau experienced an early block uplift (~20-12 Ma) and a late outward propagation uplift (~12-0 Ma).
- Our model results reconcile the long-term growth of the Northeastern Tibetan Plateau and the upstream Yellow River profile.

Abstract

The growth history of the Northeastern Tibetan Plateau (NETP) is enigmatic, with debates on when and how the NETP significantly uplifted. Here, we use a numerical landscape evolution model to quantitatively investigate the ~20 Ma growth history of the NETP by studying the formation history of the upstream Yellow River (UYR). Compared to the observed river profiles, erosion rates, the trend of acceleration time of deformation, and paleo-elevation, our modeling results suggest that the long-term growth history of the NETP consists of an early block uplift (~20-12 Ma) and a late outward propagation uplift (~12-0 Ma). Before ~12 Ma (middle Miocene), the NETP was uplifted via a block growth, with major uplift in the south part. Subsequently, the high (~5 km) NETP has been uplifted via a northward propagation growth until the present-day time. We further suggest that pure headward erosion unlikely formed the observed river profile of the UYR over the past few million years. Our modeling thus reconciles the long-term outward growth of the NETP and the UYR profile, suggesting a downstream migration of high erosion rates, which is fundamentally different from the headward erosion of small mountain rivers. The downstream propagation of fluvial erosion may commonly occur in the outward-growing plateau on Earth.

Plain Language Summary

Mountain rivers with their river profiles can record the long-term growth history of orogen. The Yellow River, the sixth longest river in the world, flows through the Northeastern Tibetan Plateau. The upstream Yellow River profile provides an opportunity to quantitatively investigate the controversial growth history of the Northeastern Tibetan Plateau. We study the formation history of the Northeastern Tibetan Plateau by a numerical landscape evolution model combining with two possible growth scenarios. Reconciling the long-term growth of the Northeastern Tibetan Plateau and the upstream Yellow River profile, our modeled results show that the Northeastern Tibetan Plateau experienced an early block uplift (~20-12 Ma) and a late outward propagation uplift (~12-0 Ma). Furthermore, the observed upstream Yellow River profile is unlikely formed by pure headward erosion over the past few million years indicated by previous studies. This work further suggests that the downstream migration pattern of high erosion rates commonly exists in tectonically active outward-growing plateaus on Earth.

1 Introduction

The Indian-Eurasian continent-continent collision (since ~55 Ma) controls the long-term growth history of the Tibetan Plateau (Yin and Harrison, 2000), influencing Asian climate change (An et al., 2001; Kutzbach et al., 1993), landscape evolution in Asia (Law and Allen, 2020; Shen et al., 2022; Yuan et al., 2021), biodiversity (Klaus et al., 2016), and carbon cycle (Guo et al., 2021; Märki et al., 2021). The critical evidence for the above research is related to when and how the Tibetan Plateau grew. However, the timing of reaching the present-day high elevations (Fang et al., 2020; Rowley and Currie, 2006; Su et al., 2019) and the mechanism of the plateau growth (Clark and Royden, 2000; England and Houseman, 1989; Royden et al., 1997; Tapponnier et al., 2001) remain highly debated.

With the growth of the Tibetan Plateau, the growth history of the NETP is still in dispute. Some researchers suggest that the Indian-Eurasian collision (since ~55 Ma) influenced the NETP soon after the collision (Clark et al., 2010; Dupont-Nivet et al., 2004), but the influences are thought to be only an immediate response to the far-field effect of collision (Dayem et al., 2009). Significant tectonic deformation and uplift of the NETP did not occur long time after the collision (Dai et al., 2006; Wang et al., 2017, 2022). For example, various sediment accumulation rates indicate that the Xining basin (Figure 1b) initiated at 55-52.5 Ma, but most tectonic activities occurred after 17 Ma (Dai et al., 2006). In the Qaidam Basin (Figure 1b), Cenozoic sediments initiated at ~25.5 Ma based on magnetostratigraphy and mammalian biostratigraphy (Wang et al., 2017), and ~30 Ma based on magnetostratigraphies combined with detrital apatite fission-track ages (Wang et al., 2022). Moreover, the initially significant activity ages in the NETP were near the Miocene (~23-5.3 Ma) (Duvall et al., 2013; Lease et al., 2011; Li et al., 2019, 2022; Yuan et al., 2011; Zhang et al., 1991; Zheng et al., 2006), and became younger to the northeast (Figure 1b, c). Additionally, how the NETP uplifted is still unclear, with contrasting views including the stepwise block extrusion and uplift to the north (Tapponnier et al., 2001) and the progressive propagation uplift to the north via the lower crustal flow (Clark and Royden, 2000).

Mountain rivers form along with the growth of orogens, thus the longitudinal river profiles can record the long-term orogenic growth history (Allen, 2008; Goren et al., 2014; Kirby et al., 2003; Pritchard et al., 2009; Whipple and Tucker, 1999). Examples include the southeastern Tibetan Plateau (Yuan et al., 2022), the Andes Orogen (Fox et al., 2015), the Anatolian Plateau (Racano et al., 2021), and the Colorado Plateau (Roberts et al., 2012). The Yellow River, the sixth longest river in the world, flows through the NETP (Figure 1), and the UYR likely recorded the long-term growth history of the NETP. Although there are still some debates on the formation time (Craddock et al., 2010; Lin et al., 2001) and the formation process (Craddock et al., 2010; Lin et al., 2001) of the UYR, its longitudinal profile offers an opportunity to reconstruct the NETP growth history by reproducing the UYR river profile.

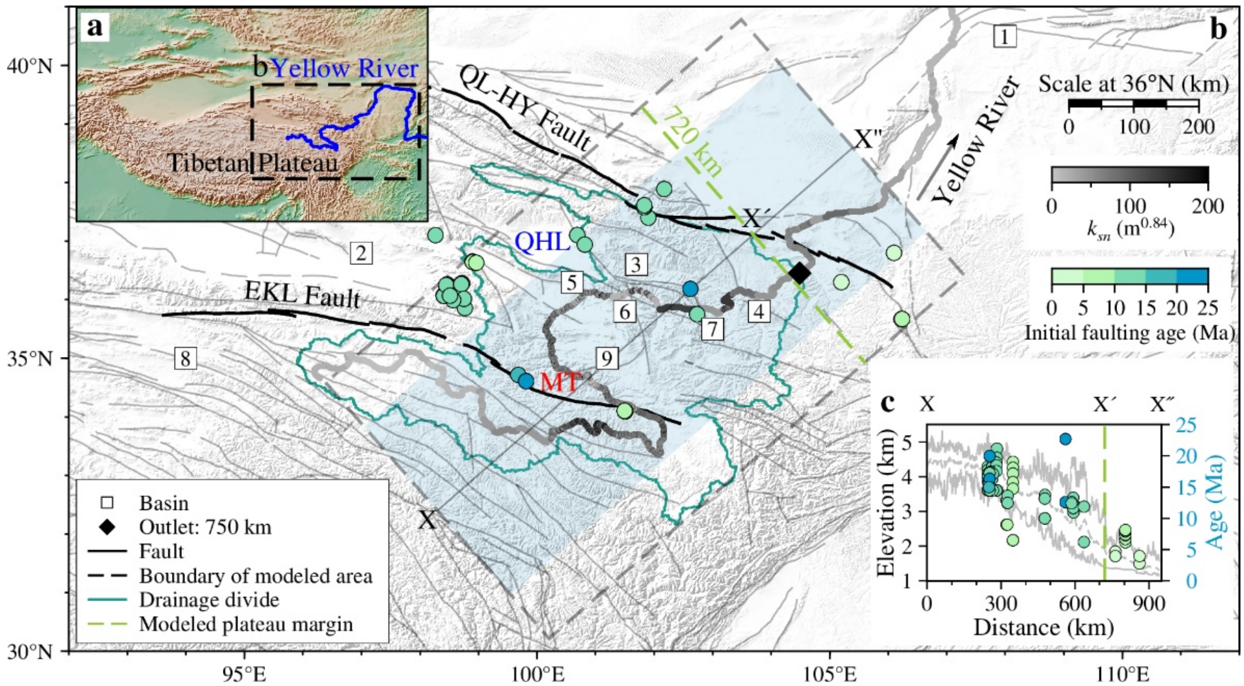

Figure 1. Geological and topographical background of the study area. (a) Topography of the Tibetan Plateau. (b) Closer view of the study area with the Yellow River in the Northeastern Tibetan Plateau. The trunk of the Yellow River is colored with the channel steepness $k_{sn} = SA^{m/n}$ with $m/n = 0.42$ (Harkins et al., 2007). QL-HY Fault: Qilian-Haiyuan Fault; EKL Fault: East Kunlun Fault; QHL: Qinghai Lake; MT: Anyemaqen Shan. Basins (square with black frames) are in (b): (1) Hetao Basin, (2) Qaidam Basin, (3) Xining Basin, (4) Lanzhou Basin, (5) Gonghe Basin, (6) Guide Basin, (7) Linxia Basin, (8) Hoh Xil Basin, and (9) Zeku Basin. The initially significant activity ages (Table S1) are from references (Duvall et al., 2013; Lease et al., 2011; Li et al., 2019, 2022; Yuan et al., 2011; Zhang et al., 1991; Zheng et al., 2006). (c) The swath profile plots (maximum, average, and minimum elevations) are based on the blue shading area in (b) with initially significant activity ages. The modeled area is 950 × 600 km^2. The width of the swath profile is 400 km. The green dashed line at 720 km indicates the plateau margin. The black arrow shows the direction of river flow.

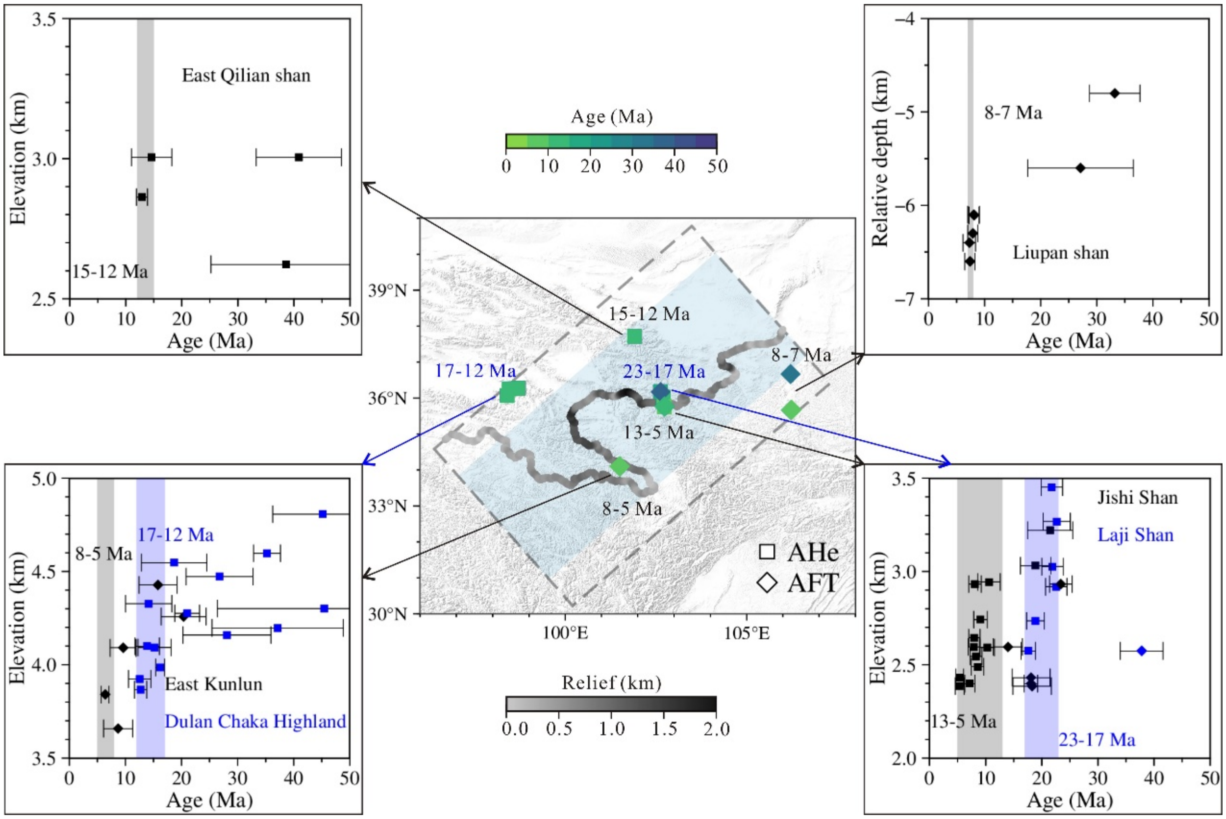

Figure 2. Thermochronometric ages and age-elevation relationships in the Northeastern Tibetan Plateau. AHe: Apatite (U-Th)/He; AFT: Apatite Fission Track. Thermochronometric ages (Table S2) are from references (Duvall et al., 2013; Lease et al., 2011; Wang et al., 2020; Zheng et al., 2006). The relief is calculated based on the difference between maximum and minimum elevations in the blue shading area.

This work aims to quantitatively study the ~20 Ma NETP growth history and the UYR formation history based on a numerical landscape evolution model (FastScape) (Braun and Willett, 2013; Yuan et al., 2019). In the NETP, we collected geomorphic data (e.g., river profile, swath profile, and relief), erosion rates, and the trend of acceleration times of deformation (e.g., initially significant activity ages and thermochronometric age-elevation relationships; Figures 1c and 2). In section 2, we propose two potential growth scenarios for the NETP growth, and then modify the numerical model to combine with two growth scenarios and several free parameters. In section 3, we test 2352 simulations with three free parameters to extract the modeled river profiles of each model. Based on the match of the observed and modeled river profiles, we obtain one of the best-fit modeled results in each growth model. Section 4 shows the NETP growth model by comparing the observed and modeled results, including the longitudinal river profiles, swath profiles, erosion rates, and the trend of acceleration times of deformation (e.g., initially significant activity ages and thermochronometric age-elevation relationships). Based on the modeled and observed results, we discuss the NETP growth history together with the UYR formation history. Furthermore, we test our results against a possibly formed UYR with a retreat process and period of pure headward erosion.

2. Methods

2.1 Landscape evolution model

The landscape evolution model FastScape (Braun and Willett, 2013; Yuan et al., 2019) is used to simulate the uplift, fluvial erosion, and sediment transport and deposition processes in the drainage basin of the UYR as

$$\frac{\partial h}{\partial t} = U - K_f \tilde{p}^m A^m S^n + \frac{G}{\tilde{p}A}\int_A \left(U - \frac{\partial h}{\partial t}\right) dA \,, \qquad (1)$$

where h is the elevation, t is the time, U is the tectonic uplift rate, K_f is the erodibility, A is the drainage area, S is the local slope in the steepest-descent direction of water flow, m is the area exponent, and n is the slope exponent. Dimensionless $\tilde{p}$ represents any spatial or temporal variation in precipitation relative to the mean precipitation rate. Dimensionless G scales the deposition coefficient. To simplify the model, the dimensionless $\tilde{p}$ is assumed uniform ($\tilde{p}$ = 1), and the dimensionless G is assumed uniform (G = 1; Guerit et al., 2019; Yuan et al., 2019). We use the slope exponent $n = 1$ and $m = 0.42$ (i.e., m/n = 0.42) based on previous studies (e.g., Harkins et al., 2007). Although Harkins et al. (2007) suggest the slope exponent n is less than unity, for values of $n \neq 1$, there are some trade-offs between K_f and n (Goren et al., 2014), which should not influence the main results of our modeling (Yuan et al., 2022).

2.2 Two growth models for the Northeastern Tibetan Plateau

We apply two double-stage growth models, including a two-block stage (block-block) growth model and a block-propagation growth model (Figure 3), to explore the ~20 Ma NETP growth history. The first model is consistent with the two-stage stepwise uplift in the NETP (Tapponnier et al., 2001). The latter model is inspired by various orogenic growth models, which suggest mountain belts growing to a certain height, and then expanding laterally in an outward growth sequence characterized by a more successive marginal uplift (Jammes and Huismans, 2012; Wolf et al., 2022; Yuan et al., 2021), e.g., the outward growth of the Tibetan Plateau (Wang et al., 2014). The two growth models for the NETP with several free parameters simulate various uplift cases that predict different topographic evolutions (Figure 3). The two double-stage growth models for the NETP are likely the simplest plausible scenarios to produce our modeled results, without taking into account the complexities of the NETP, such as the influences of the strike-slip faults on the rock uplift (Tapponnier et al., 2001).

We use a logistic function of elevation (h_f) from the previous study (Yuan et al., 2021) to match the present-day maximum topography of the NETP as

$$h_f(x, L) = \frac{h_0}{1+e^{[(x-L)/W]}}, \tag{2}$$

where h_0 is the present-day maximum elevation, W is the characteristic width of the plateau margin, L is the total length of the plateau, and x is the distance to the plateau margin.

For the first stage of block uplift (Figure 3a, b), the uplift rate is

$$U_{1\mathrm{B}} = (h_{1\mathrm{B}}(x, L_{1\mathrm{B}}) - h_i)/t_{1\mathrm{B}}\,, \text{ with } h_{1\mathrm{B}}(x, L_{1\mathrm{B}}) = \frac{h_0}{1+e^{(x-L_{1\mathrm{B}})/W}}, \tag{3}$$

where h_i is the initial elevation before the block uplift, $L_{1\mathrm{B}}$ and $t_{1\mathrm{B}}$ are the length and duration of the first block uplift stage, respectively. For the second stage of block uplift (Figure 3a), the uplift rate is

$$U_{2\mathrm{B}} = \left[h_f(x, L) - h_{1\mathrm{B}}(x, L_{1\mathrm{B}})\right]/t_{2\mathrm{B}}\,, \tag{4}$$

where $t_{2\mathrm{B}}$ is the duration of the second block uplift stage. For the second stage of propagating uplift (Figure 3b), the uplift rate modified from Yuan et al. (2021) is

$$U_{2\mathrm{P}} = \frac{h_0 v_0 e^{(x-x_0)/W}}{W\left[1+e^{(x-x_0)/W}\right]^2}, \text{ with } x_0 = L_{1\mathrm{B}} + v_0 t\,, \tag{5}$$

where x_0 and v_0 are the growth length and growth velocity ($v_0 = (L - L_{1\mathrm{B}})/t_{2\mathrm{B}}$), respectively.

The uplift rate U in equation (1) is replaced by $U_{1\mathrm{B}}$, $U_{2\mathrm{B}}$, and $U_{2\mathrm{P}}$ for the block growth and propagation growth model. According to the above equations, uplift rates ($U_{1\mathrm{B}}$, $U_{2\mathrm{B}}$, and $U_{2\mathrm{P}}$) depend much on the growth duration ($t_{1\mathrm{B}}$) and distance ($L_{1\mathrm{B}}$). Thus, there are only three free parameters (i.e., K_f, $x_{1\mathrm{B}}$, and $t_{1\mathrm{B}}$) for each growth model.

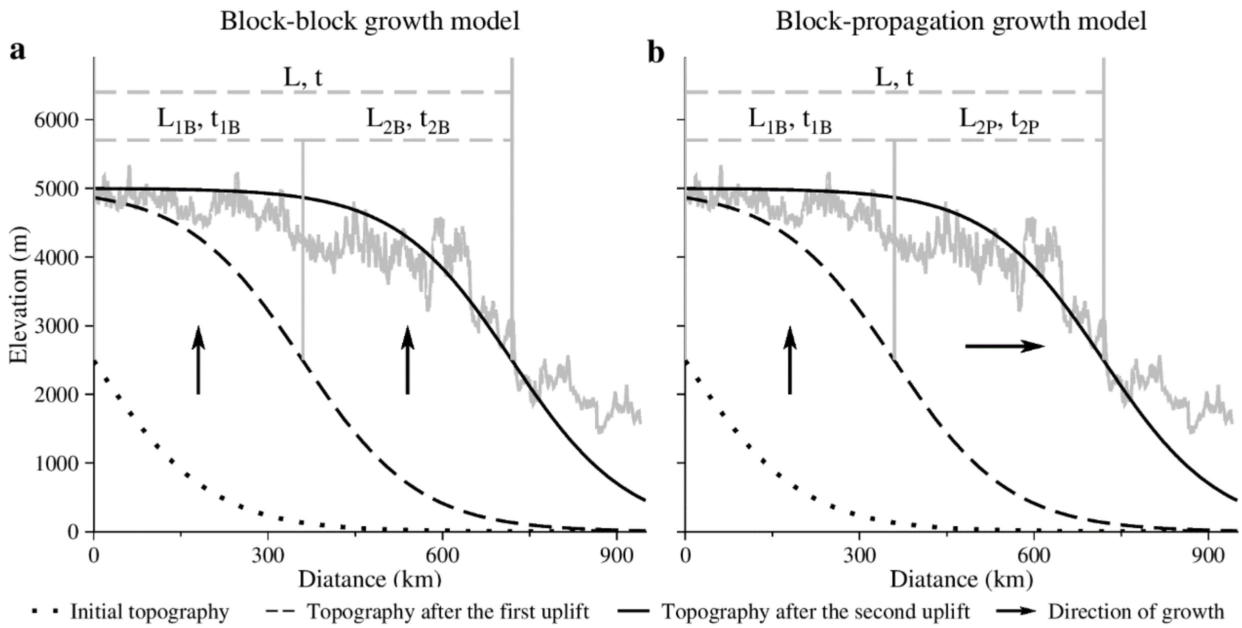

Figure 3. Diagrams for two growth models. (a) Block-block growth model. (b) Block-propagation growth model. Grey curves are the observed maximum topography within the blue shading area in Figure 1b. The present-day topography can be matched by a function in equation (2) (dark solid curve). L_{1B} and t_{1B} are the distance and duration of the first block growth, respectively. L_{2B} and t_{2B} are the distance and duration of the second block growth, respectively. L_{2P} and t_{2P} are the distance and duration of the second propagation growth, respectively. The block growth uplifts vertically, and the propagation model grows horizontally.

2.3 Model setup

In the NETP, the initially significant activity ages are younger than ~20 Ma (Figure 1b, c) (Duvall et al., 2013; Lease et al., 2011; Li et al., 2019, 2022; Yuan et al., 2011; Zhang et al., 1991; Zheng et al., 2006), and the modern high elevation was reached within ~23-11 Ma (Ding et al., 2022; Miao et al., 2022). Thus, we set the total growth duration of the two-stage uplift to 20 Myr ($t = t_1 + t_2 = 20$ Myr) cover the maximum growth age of the NETP. The total growth distance of the two-stage uplift is set to 720 km ($L = L_1 + L_2 = 720$ km) in our growth models, based on the present-day topography from the plateau interior to the plateau margin (near the Haiyuan Fault, Figure 1b, c).

To fit the present-day maximum topography of the NETP (equation 2), we set the maximum elevation to 5 km (i.e., $h_0 = 5$ km), and the characteristic width of propagation uplift to 100 km (i.e., $W = 100$ km). To model landscape evolution in the NETP, we define a rectangular domain size of 950 × 600 km (Figure 1b) with each node size of 1 × 1 km, and run the model for 20 Myr. To increase modeling efficiency, we use a time step length of 100,000 years to find one of the best-fit models and a time step length of 10,000 years to extract information from the best-fit model. The modeled river profiles are similar by testing different time steps from 10,000 to 100,000 years (Figure S1). In the NETP, initial elevations (0-2500 m) with maximum elevations in the model south boundary (Figure 3) and random white noise (≤ 500 m) are assumed, based on the maximum elevations were ~2500 ± 500 m at ~20 Ma near the south of the modeled area (Polissar et al., 2009; Sun et al., 2015).

2.4 Misfit function

The forward analyses of the landscape evolution model are used to explore the multidimensional space of free parameters (i.e., K_f, $x_{1\mathrm{B}}$, and $t_{1\mathrm{B}}$). Optimum values are found when the modeled river profile best matches the observed river profile of the UYR in the NETP. A parameter of χ was used to normalize the river profiles (Perron and Royden, 2013) at the point x:

$$\chi(x) = \int_{x_b}^{x} \left(\frac{A_0}{A(x)}\right)^{m/n} dx\,, \tag{4}$$

where x_b is the base level (outlet: 750 km; Figure 1b), A_0 (= 1 m^2) is a reference drainage area, and $A(x)$ is the drainage area of the point x. We first calculate the observed χ_i^{obs} values of the UYR at each elevation bin h_i (i = 1, 2, …, N). Then, at the final step of the model, we obtain the modeled trunks (i.e., the longest channel of each modeled basin), and calculate the modeled χ_i^{mod} values at the corresponding elevation bin h_i.

Table 1. Free parameters range in the forward analysis.

Growth model	K_f (× 10^{-7} m$^{0.16}$/yr)		L_{1B}(km)		t_{1B}(Myr)	
	Model range	Interval	Model range	Interval	Model range	Interval
Block-block growth model (Figure 3a)	15-41	2	0-700	100	0-20	1
Block-propagation growth model (Figure 3b)	15-41	2	0-700	100	0-20	1

An average misfit (μ) function compared the χ of modeled and observed river profiles:

$$\mu = \frac{1}{N_t}\sqrt{\frac{1}{N}\sum_{i=1}^{N}\frac{\left(\chi_i^{obs}-\chi_i^{mod}\right)^2}{(\delta_x)^2}}, \tag{5}$$

where δ_x (= 8 m) is the uncertainty for the χ comparison set arbitrary, N_t is the total number of all modeled trunks in the final step. For each growth model, 2352 (14 × 8 × 21) forward process models are used to constrain the best-fit sets of three free parameters (Table 1).

3 Results

We plot the misfit values μ ($log_{10}(\mu) < 2.0$) of the two growth models for three free parameters (K_f, $x_{1\mathrm{B}}$, and $t_{1\mathrm{B}}$) with different colors (Figures 4 and S2). The best-fit value of the block-block growth model is higher than that of the block-propagation growth model. In the low $log_{10}(\mu) < 0$ values (i.e., the best-fit models within uncertainty) of the block-block growth model, the distances (L_{1B}) and durations (t_{1B}) are less than 500 km and 15 Myr, respectively. The smallest $log_{10}(\mu)$ value is −0.335 marked by the black box in Figure 4a (K_f = 29 × 10^{-7} $\mathrm{m}^{0.16}/\mathrm{yr}$, L_{1B} = 100 km, and t_{1B} = 5 Myr). There is no modeled river profile (χ-elevation plots) matching well the observed river profile for the block-block growth model, even the best-fit modeled results (Figure 5a). In the low $log_{10}(\mu) < 0$ of the block-propagation growth model, the distances (L_{1B}) and the durations (t_{1B}) are less than 500 km and 17 Myr, respectively. The smallest $log_{10}(\mu)$ value is −0.439 marked by the black box in Figure 4b (K_f = 21 × 10^{-7} $\mathrm{m}^{0.16}/\mathrm{yr}$, L_{1B} = 100 km, and t_{1B} = 8 Myr). Several best-fit modeled river profiles matched the observed river profile well for the block-propagation growth model (Figure 5b).

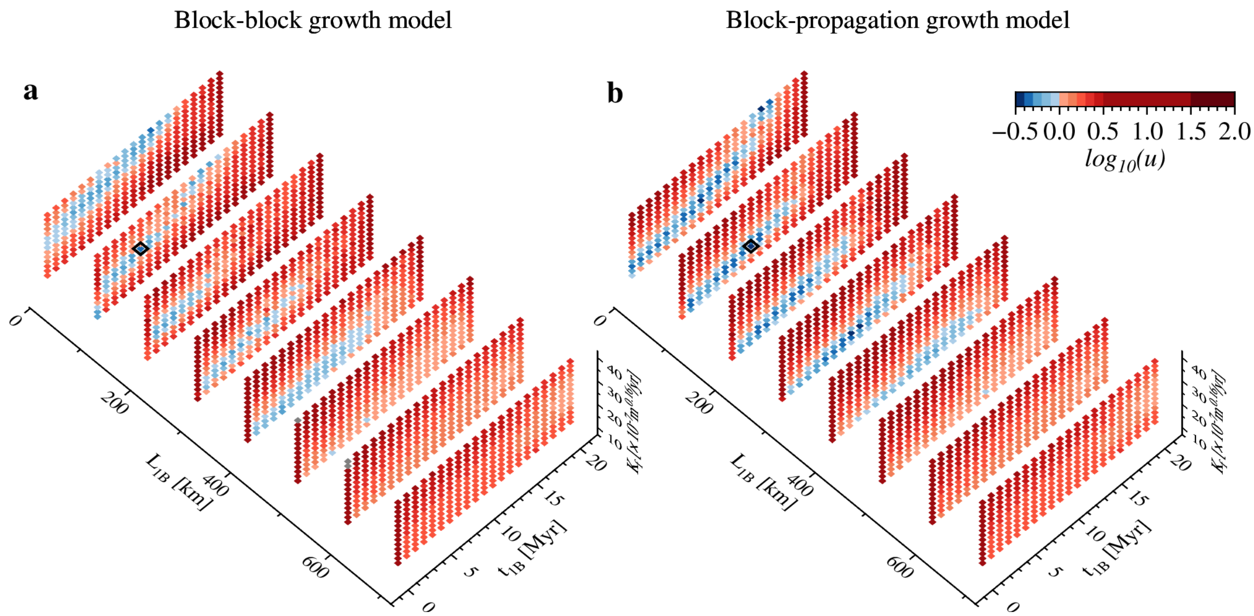

Figure 4. Modeled misfits of two growth models with each model 2352 forward analyses. (a) Block-block growth model. A black box marks one of the best-fit parameter sets (K_f = 29 × 10^{-7} $m^{0.16}$/yr, L_{1B} = 100 km, and t_{1B} = 5 Myr), and the smallest $log_{10}(\mu)$ value is −0.335. (b) Block-propagation growth model. A black box shows one of the best-fit parameter sets (K_f = 21 × 10^{-7} $m^{0.16}$/yr, L_{1B} = 100 km, and t_{1B} = 8 Myr), and the smallest $log_{10}(\mu)$ value is −0.439.

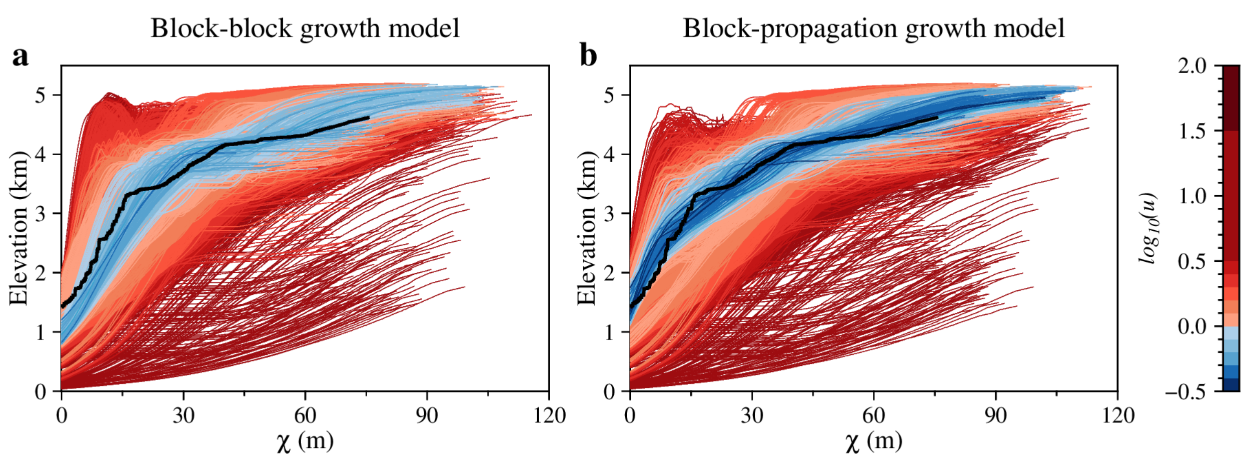

Figure 5. Modeled (colored) and observed (black) river profiles are plotted by χ. (a) In the block-block growth model, the modeled river profiles are less consistent with the observed river profile of the upstream Yellow River. (b) In the block-propagation growth model, several modeled river profiles with dark blue color matched well the observed river profile of the upstream Yellow River. The cooler the color, the lower the misfit values, and the better the modeling results.

4 Discussion

4.1 The best-fit growth model of the Northeastern Tibetan Plateau

This section compares one of the best-fit modeled results in each growth model to the observed results. χ-elevation plots are extracted from modeled trunks and the UYR. Although the modeled river profiles in each growth model are consistent with the upper reach of the observed river profile (with elevations >3500 m), only the modeled river profiles in the block-propagation growth model are consistent with the lower reach of the observed river profile (Figure 6b, e). In addition, the observed and modeled swath profiles of the block-propagation growth model are more consistent than that of the block-block growth model (Figure 6c, f).

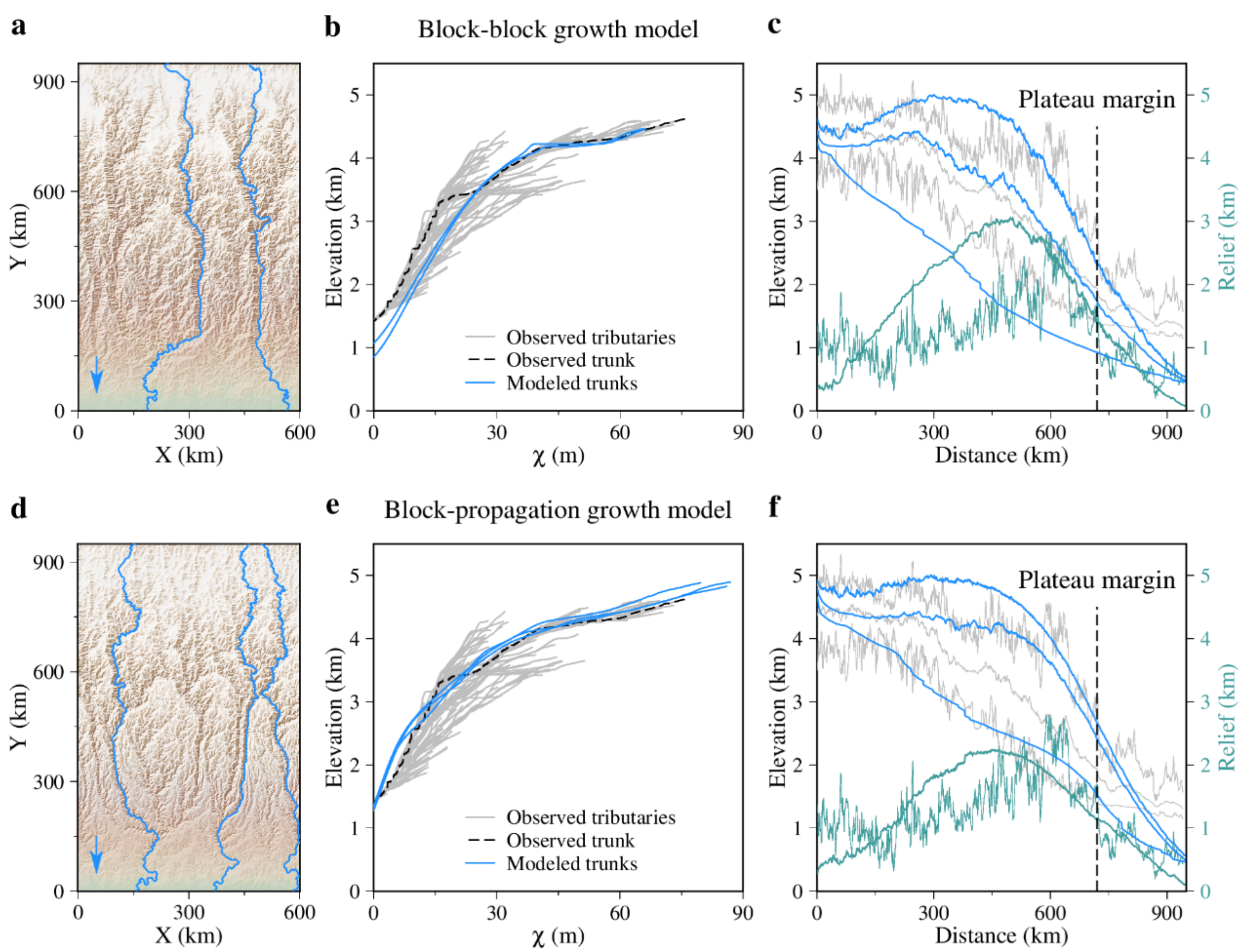

Figure 6. The comparison of geomorphic data between the best-fit model results of each growth model and the upstream Yellow River. (a, d) Modeled landscapes and trunks (blue lines). Blue arrows mark river directions. (b, e) χ-elevation plots. (c, f) Modeled and observed swaths and relief extracted from the whole

modeled domain and the blue shading area of the Northeastern Tibetan Plateau in Figure 1b, respectively. The modeled trunks are the longest channels of each modeled basin. Grey and black lines are the observed results, and blue lines are the modeled results in (b), (c), (e), and (f). In (c) and (f), green lines are the relief.

The modeled erosion rates and the trend of acceleration times of deformation are also compared to the observed results. Modeled erosion rates from the block-propagation growth model can better match most erosion rates from the plateau interior to the plateau margin (Figure 7b), which is similar to the downstream increase of incision in the Daxia River (Zhang et al., 2017a), a tributary of the UYR. Modeled age-elevation relationships show that only one synchronous acceleration occurred in the block-block growth model (Figure 8b), which differs from the observed various acceleration times of deformation (Figure 2). Examples include the East Kunlun around 8-5 Ma (Duvall et al., 2013), the Dulan Chaka Highland around 17-12 Ma (Duvall et al., 2013), the Laji Shan around 23-17 Ma (Lease et al., 2011), the Jishi Shan around 13-5 Ma (Lease et al., 2011), the East Qilian Shan around 15-12 Ma (Wang et al., 2020), and the Liupan Shan around 8-7 Ma (Zheng et al., 2006). In contrast, a northward progressive acceleration occurred in the block-propagation growth model (Figure 8c), more consistent with the initially significant activity ages which became younger to the northeast in the NETP (Figure 1c). Moreover, the significant increasing uplift rate occurred after ~5 Ma near the plateau margin (~720 km) (Figure 8c), consistent with previous studies (Zhang et al., 2023). Thus, based on the comparisons of river profiles, swath profiles, erosion rates, and the trend of significant acceleration times (e.g., initially significant activity ages and thermochronometric age-elevation relationships), the block-propagation growth model fits better with the NETP growth records.

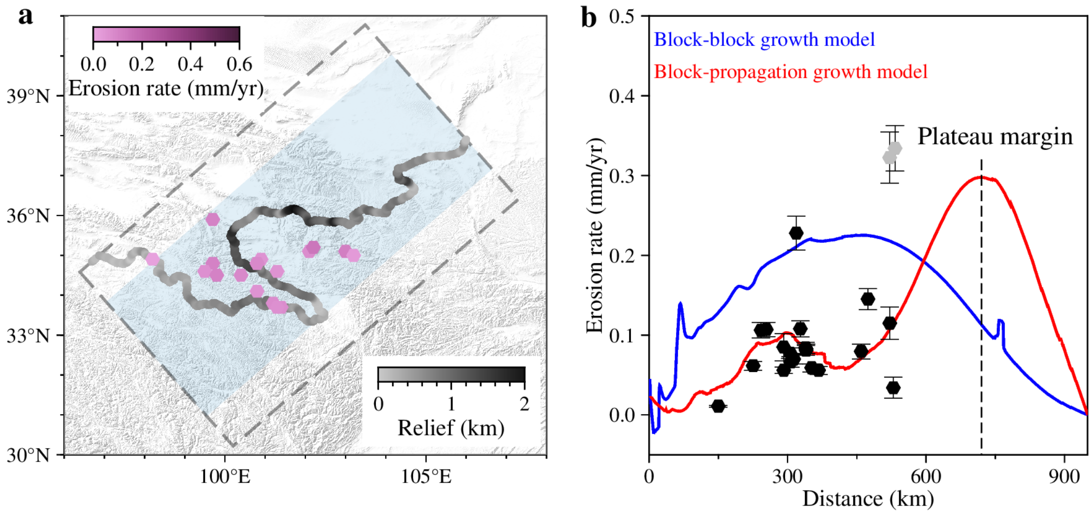

Figure 7. Comparison of the observed and modeled erosion rates. (a) Erosion rates distribution. (b) Comparisons of modeled erosion rates along the river profile. Erosion rates (Table S3) are from references (Harkins et al., 2007; Kirby and Harkins, 2013; Lal et al., 2004; Li et al., 2014b; Zhang et al., 2017a). Grey dots are influenced by transient sediments (Zhang et al., 2017a).

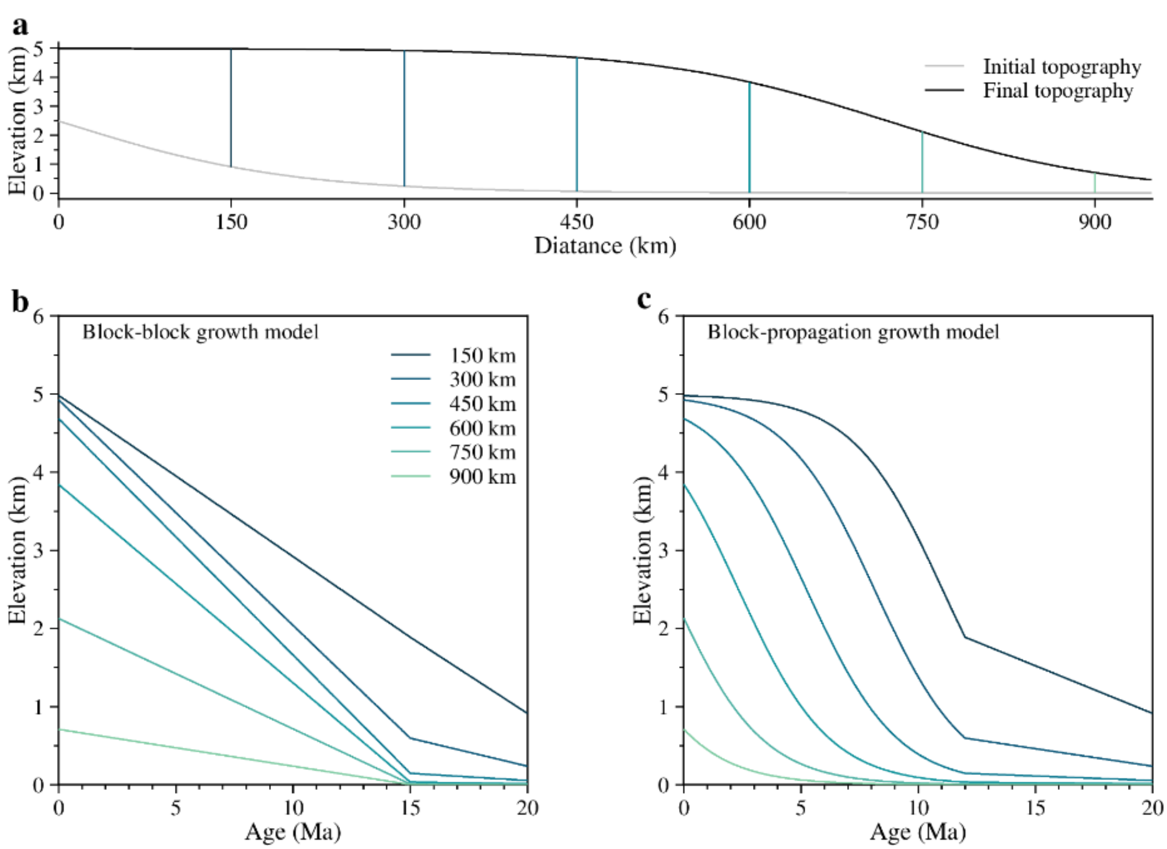

Figure 8. Modeled age-elevation relationships of two growth models. (a) Location of different distances. (b) Block-block growth model. (c) Block-propagation growth model.

4.2 Growth history of the Northeastern Tibetan Plateau

Based on our forward analyses, the block-propagation growth model matches better the NETP growth records. The major range of block uplift only occurred in the south of the modeled area before ~12 Ma (middle Miocene), with broad low elevations in most of the modeled area (Figure 9). Then, a broad propagation uplift occurred in the modeled area from ~12 Ma to the present, forming the modern plateau margin (Figure 9). High elevations (~5 km) expand northward during the plateau growth (Figure 9g).

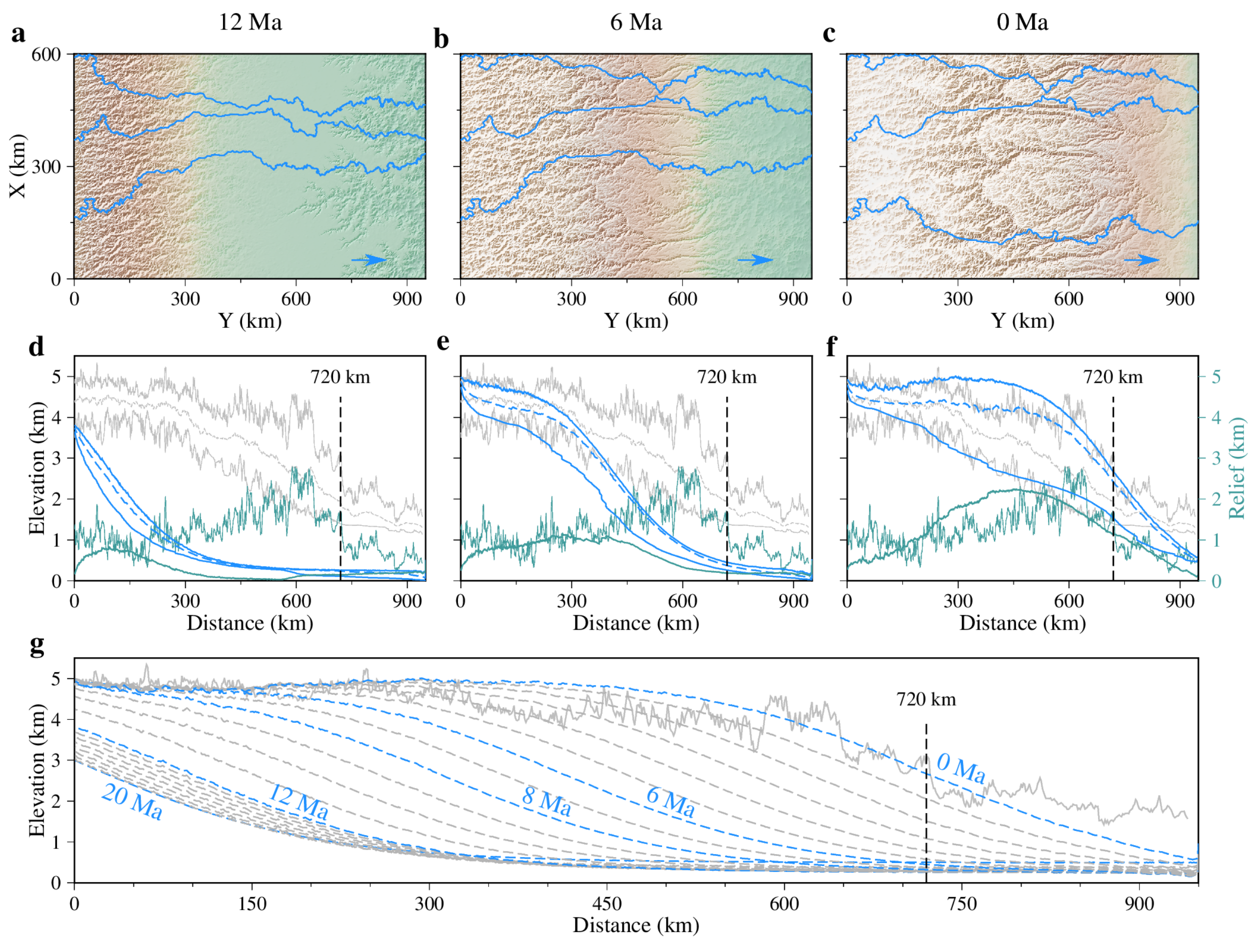

Figure 9. Typical modeled scenarios of the block-propagation growth model. Top panels are modeled landscapes and trunks (blue) at (a) 12 Ma, (b) 6 Ma, and (c) 0 Ma. Blue arrows mark river directions. Middle panels are observed (grey) and modeled (blue) swath profiles and relief (green) at (d) 12 Ma, (e) 6Ma, and (f) 0Ma. (g) The bottom panel shows the maximum elevations along modeled trunks during uplifting. Dashed lines are modeled maximum elevations from 20 Ma to 0 Ma. A grey continuous line is the observed maximum elevation at 0 Ma. The black dashed line at 720 km in (d), (e), (f), and (g) indicates the plateau margin.

Our modeled data are consistent with various observed data, including crustal deformations (Fan et al., 2019; Royden et al., 2008; Yan et al., 2006; Yu et al., 2023) and sedimentary records (Chang et al., 2015; Li et al., 2011). For example, most initial faulting ages in the NETP were after ~20 Ma, with a northward younging trend (Figure 1b, c). The initial propagation uplift time (~12 Ma) is consistent with the widespread middle-Miocene crustal deformation in the NETP (Yu et al., 2023), the formation time (Miocene) of basin-bounding faults in the NETP and the eastern segment of the NETP (Fan et al., 2019). The propagation uplift time of ~12 Ma is also consistent with most of the shortening after ~15 to 20 Ma in the NETP (Royden et al., 2008), and a clockwise rotation during 11-17 Ma in the Guide Basin (Figure 1b) (Yan et al., 2006) based on the magnetostratigraphy. The initial propagation uplift time is also close to the accumulation rate abruptly increased near ~15 Ma in the Qaidam Basin (Figure 1b) based on a stratigraphic study (Chang et al., 2015), and the progressive surface uplift since 15 Ma in the NETP based on the Nd isotopic ratio of Asian dust (Li et al., 2011).

We show the major block uplift and higher elevations occurring in the south of the NETP before ~12 Ma, with broad low elevations to the north, consistent with the observed higher elevations in the south (Polissar et al., 2009; Sun et al., 2015) and low elevations in the north of the East Kunlun fault (Hui et al., 2018). The Hoh-Xil Basin (upper part of the UYR, Figure 1b) reached 1395-2931 m before 17 Ma based on the leaf fossils from an early Miocene barberry (*Berberis*) (Sun et al., 2015), or had uplifted at least 1700-2600 m before the middle Miocene based on δD ratio of surface waters from freshwater limestones (Polissar et al., 2009). In contrast, the Zeku Basin (lower part of the UYR, Figure 1b) had 1200-1400 m elevations during the early to middle Miocene based on palynological data (Hui et al., 2018). Our results are also consistent with the observations of the south of the East Kunlun Fault (Hoh Xil Basin) reached 2-3 km before the Miocene and the modern high elevation of ~4.6 km after ~17 Ma (Staisch et al., 2016). The Hoh Xil Basin had probably reached its current elevation of ~4.6 km by ~12 Ma, considering possible uncertainties (Li and Garzione, 2023). The north of the East Kunlun Fault reached the modern high elevations after ~11 Ma (Miao et al., 2022), based on the pollen records of montane conifers. The surface uplift is not synchronous but is progressive to the north, consistent with our modeling (Figure 9g).

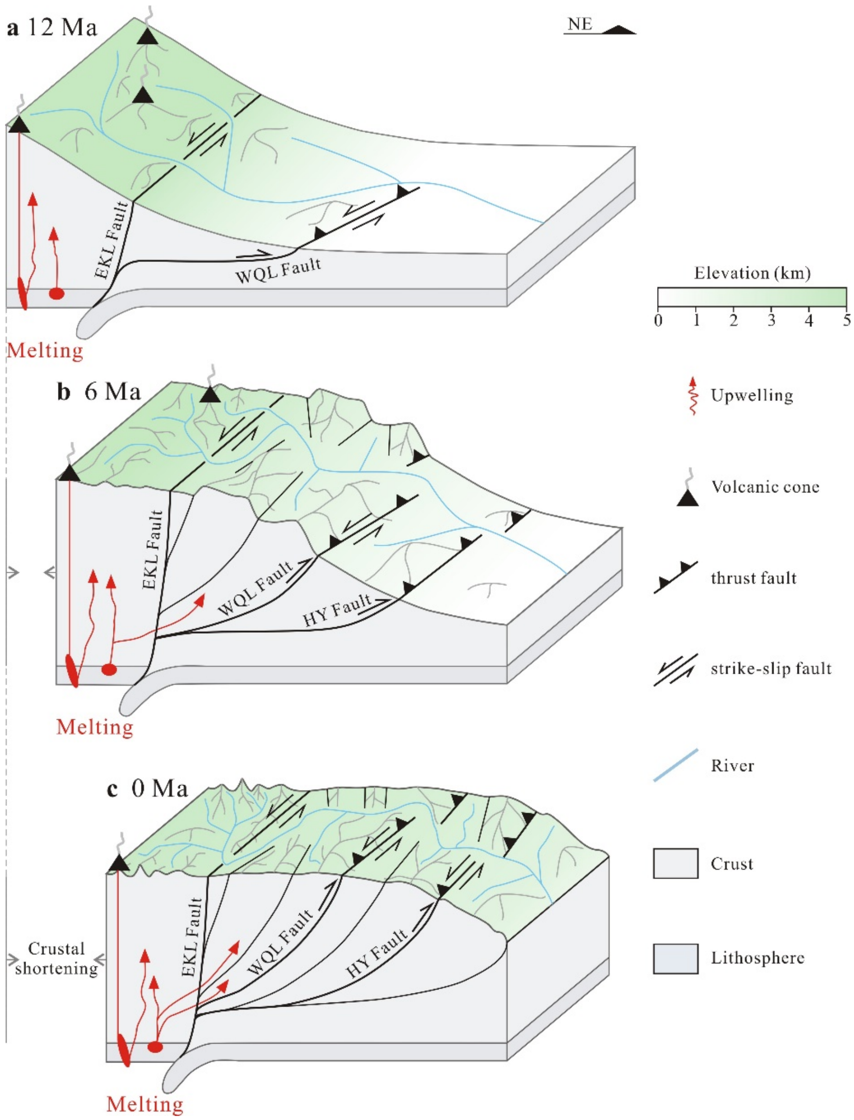

Figure 10. Schematic models illustrate different growth mechanisms on both sides of the East Kunlun Fault. (a) The scenario occurred after block growth (12 Ma) with higher elevations in the south of the East Kunlun Fault than in the north. (b) Propagation growth at 6 Ma. (c) Schematic present-day topography (0 Ma). The hypothetical elevations in the diagrams are based on the uplift process in Figure 9g. Initial significant activity ages are based on the data in Figure 1b. EKL Fault: East Kunlun Fault; WQL Fault: West Qinling Fault; HY Fault: Haiyuan Fault. Deep structures are modified from Tapponnier et al. (2001). Primary faults in the NETP are modified from references (Tapponnier et al., 2001; Yuan et al., 2013).

Different uplift processes in the south and north of the East Kunlun Fault may be related to different uplift mechanisms (Chen et al., 2017; Lease et al., 2012; Staisch et al., 2016; Tapponnier et al., 1990) (Figure 10). The East Kunlun Fault is an important rheological boundary (Karplus et al., 2011; Le Pape et al., 2012), based on a magnetotelluric profile crossing the Northern Tibetan Plateau (Unsworth et al., 2004). Because of different growth processes in the south and north of the East Kunlun fault, a Paleogene basin was partitioned into the Hoh Xil and Qaidam subbasins by the East Kunlun fault before the middle Miocene (Chen et al., 2017; Yin et al., 2008). In the south of the East Kunlun Fault, the upper crustal shortening within the Hoh Xil Basin ceased between 33.5 and 27.3 Ma (Staisch et al., 2016), and the crust thickening driven by mantle removal related to partial melting or mantle melting (Chen et al., 2017; Staisch et al., 2016) played an important role in the plateau growth since the Miocene (Figure 10a). The surface has been raised ~2 km by mantle melting since the early Miocene (25-20 Ma) (Chen et al., 2017). The magmatic activities widely occurred in the south of the East Kunlun Fault, related to opposing north-directed and south-directed continental subduction after 25 Ma (Guo and Wilson, 2019). In contrast, magmatic activities were rare in the north of the East Kunlun Fault (Yin and Harrison, 2000).

In the north of the East Kunlun Fault, some researchers suggest that the partial melt penetration probably characterizes the plateau growth (Karplus et al., 2011; Medvedev et al., 2006), but crust thickening driven by shortening played a critical role in forming the NETP through fault thrusting and folding (Hu et al., 2015; Lease et al., 2012; Tapponnier et al., 1990) (Figure 10b, c). A transition of the tectonic regime, from extrusion to the distributed shortening in the Northern Tibetan Plateau, was initiated at ~15 Ma (Lu et al., 2016). The distributed crustal shortening was one of the dominant processes in the Northern Tibetan Plateau construction (Zuza et al., 2016). For example, the Jishi Shan, between the Kunlun and Haiyuan left-lateral faults, experienced accelerated exhumation due to thrust-induced rock uplift and erosion at ~13 Ma based on thermochronological data (Lease et al., 2011). More than half of net Cenozoic crustal shortening and thickening in this area has occurred since ~13 Ma, based on cross-section reconstructions (Lease et al., 2012). A reconstruction of crustal thickness around the Jishi Shan shows the crust thickening from the middle Miocene thickness of 50 ± 4 km to the modern thickness of 56 ± 4 km (Lease et al., 2012). In addition, most of the present elevations were reached since the middle Miocene in the NETP (Hui et al., 2018; Zhuang et al., 2014). In the Zeku basin (Figure 1b), the present 60-70% elevations were mainly uplifted since the early-middle Miocene, based on palynological data in the Caergen section (Hui et al., 2018). The Qaidam Basin, near the UYR, whose present elevations of 70% were uplifted during 15-10.4 Ma, based on Leaf wax stable isotopes in the Huaitoutala section (Zhuang et al., 2014).

In summary, consistent with the above studies, our modeled results suggest that most present-day high elevations (~5 km) have been reached since the middle Miocene in the north of the East Kunlun Fault, and then the high elevations expanded northward. The plateau uplift is mostly attributed to the crustal thickening, and the gradual propagation was related to the crustal shortening through fault thrusting and folding.

4.3 Headward erosion cannot form the observed upstream Yellow River profile

The NETP growth primarily controls the UYR formation. However, the UYR formation time is debated, varying from >11.63 Ma to >0.03 Ma based on the initial incision timing (~1.8-0.03 Ma) of the upmost terraces (Craddock et al., 2010), the dating of basin sediments (~1.7 Ma) (Li et al., 2014a), the similar provenance signals in the Linxia and Lanzhou Basins (Figure 1b) (~3.6 Ma) (Nie et al., 2015), the isolation time (1.2-0.5 Ma) of the Qinghai Lake (Figure 1b) (Zhang et al., 2014), the divergence time (~0.19 Ma) of two species (Liang et al., 2018), the sediment in the Hetao Basin (Figure 1b) (~1.68 Ma) (Li et al., 2023), the termination time (~4.8 Ma) of fluviolacustrine-dominated red beds in the Xining Basin (Figure 1b) (Zhang et al., 2017b), and the initial sedimentation (>11.63 Ma) of Eocene-Miocene red bed in the Lanzhou zone (Lin et al., 2001). Among these formation timings, some studies suggest that the UYR formed over the last few million years (~2.58-0.03 Ma) since the UYR excavated basin sediments systematically upstream through headward erosion (Craddock et al., 2010; Jia et al., 2017; Su et al., 2023), with a rate of ~350 km Myr^{-1} (Craddock et al., 2010). The block-block growth model experiences headward erosion in our study because the modeled area only grows upward without horizontal motion. χ-elevation plots from all block-block growth models, compared to the UYR river profile, show that no appropriate modeled results can match the observed UYR river profile (Figure 5a). In contrast, a few block-propagation growth model results match the observed UYR river profile (Figure 5b). The high erosion rates mainly propagated downstream during the outward propagation of the NETP growth, similar to the erosion pattern that occurred in the eastern Tibetan Plateau (Yuan et al., 2023).

Next, we test whether the pure headward erosion (and retreat process) can form the UYR river profile using the landscape evolution model with various erodibilities and model run durations. To match the elevation of the observed base level of the NETP margin, we set the modeled boundary at 820 km (Figure 11). The initial topography is set to the maximum topography

(Figure 3) based on equation 2, with the amplitude white noise (<100 m). The fluvial erodibilities are set to (2, 4, 6, 8, 10, and 12) × 10^{-6} $m^{0.16}/yr$, and the model run durations are set to (2, 4, 6, 8, and 10) Myr for modeling the retreat process (Figure 11). Modeled river profiles (Figure 5a, 11) indicate that the pure headward erosion suggested by previous studies (Craddock et al., 2010; Harkins et al., 2007; Jia et al., 2017; Su et al., 2023) hardly formed the UYR river profile over a few million years.

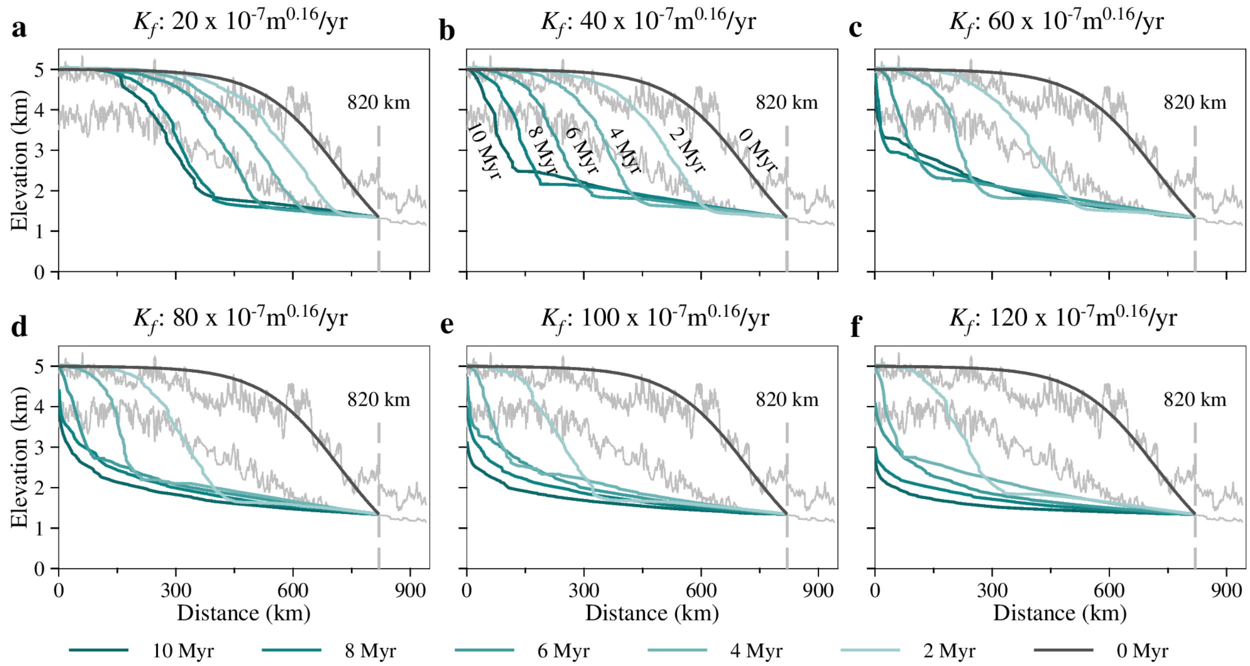

Figure 11. The observed maximum and minimum elevations (grey) and modeled (thick line) river profiles from different sets of erodibilities and model durations in each headward erosion and retreat process. We set the modeled boundary at 820 km to match the elevation of the observed and modeled base levels.

Most young formation times of the UYR are suggested based on the abandonment time (i.e., initial incision time) of the upmost terraces (Craddock et al., 2010; Jia et al., 2017; Su et al., 2023; Zhang et al., 2014). However, the divergent young ages for the inception of the Yellow River can be related to periodic climate fluctuations, and may correspond only to different re-integration events due to deglaciation or desiccation (Zhao et al., 2023). The re-integration events due to desiccation have been reported in the Yellow River middle reach (Zhao et al., 2023). In addition, the formation, abandonment, and preservation of fluvial terraces are often related to changes in tectonics and/or climate (Reusser et al., 2004; Wang et al., 2015). Modifying any external factors can rework the previously formed fluvial terraces and erase the previous geomorphic and stratigraphic records (Pan et al., 2009), and the hoarier records of fluvial terraces may be modified more easily.

On the other hand, the thermochronometric age-elevation relationships (Figure 2), responding to a long-term history of exhumation, suggest that the NETP experienced a long-term exhumation history, rather than a short-term erosion history over a few million years. Moreover, there were connections between the upstream mountain and the downstream basin before 20 Ma in the NETP (Liu, 2015). Sediments from the Anyemaqen Shan (Figure 1b) were deposited in the Guide Basin during 53-33 Ma and in the Lanzhou Basin around 43 Ma (Liu, 2015). In summary, we suggest that the UYR may have existed long accompanying the long-term NETP growth, based on our modeled results, previous studies, and thermochronometric data.

5 Conclusions

Using a numerical landscape evolution model, we quantitatively study the ~20 Ma growth history of the NETP correlated with the formation of the UYR. The block-propagation growth model, comprised of an early block uplift (~20-12 Ma) and a late propagation uplift (~12-0 Ma), is consistent with the records of the NETP based on the comparisons of the observed and modeled river profiles, swath profiles, erosion rates, the trend of acceleration times of deformation (e.g., initially significant activity ages and thermochronometric age-elevation relationships), and paleo-elevation datasets. We show that a block growth primarily occurred in the south of the NETP before ~12 Ma (middle Miocene), and a propagation growth broadly occurred in the NETP after ~12 Ma with high elevations (~5 km) expanding northward. We further suggest that pure headward erosion unlikely formed the river profile of the UYR over a few million years. Our results show that the long-term fluvial erosion in the NETP features mainly a downstream migration of high erosion rates, which is significantly different from the headward erosion of small mountain rivers. This erosion pattern in the NETP, similar to that occurred in the Eastern Tibetan Plateau (Yuan et al., 2023), may represent a common erosion pattern of outward-growing plateaus in tectonically active regions on Earth.

Acknowledgments

We thank XXX for reviewing. X.P.Y. acknowledges funding from NSFC (Grant 42272261).

Data Availability Statement

The codes used for the simulations are available in Yuan et al. (2019) and https://doi.org/10.5281/zenodo.3833983 website (Bovy & Braun, 2020). Figures were made using ParaView, CorelDRAW, and Generic Mapping Tools.

References

Allen, P. A. (2008), From landscapes into geological history: *Nature*, 451 (7176), 274-276. Doi: 10.1038/nature06586.

An, Z., Kutzbach, J. E., Prell, W. L., & Porter, S. C. (2001), Evolution of Asian monsoons and phased uplift of the Himalaya–Tibetan plateau since Late Miocene times: *Nature*, 411 (6833), 62-66. Doi: 10.1038/35075035.

Bovy, B., & Braun, J. (2020). Fastscape-lem/fastscapelib-fortran. Zenodo. Doi: 10.5281/zenodo.3833983.

Braun, J., & Willett, S. D. (2013), A very efficient O(n), implicit and parallel method to solve the stream power equation governing fluvial incision and landscape evolution: *Geomorphology*, 180-181 (170-179. Doi: 10.1016/j.geomorph.2012.10.008.

Chang, H., Li, L., Qiang, X., Garzione, C. N., Pullen, A., & An, Z. (2015), Magnetostratigraphy of Cenozoic deposits in the western Qaidam Basin and its implication for the surface uplift of the northeastern margin of the Tibetan Plateau: *Earth and Planetary Science Letters*, 430 (271-283. Doi: 10.1016/j.epsl.2015.08.029.

Chen, J.-L., Yin, A., Xu, J.-F., Dong, Y.-H., & Kang, Z.-Q. (2017), Late Cenozoic magmatic inflation, crustal thickening, and >2 km of surface uplift in central Tibet: *Geology*, 46 (1), 19-22. Doi: 10.1130/g39699.1.

Clark, M. K., Farley, K. A., Zheng, D., Wang, Z., & Duvall, A. R. (2010), Early Cenozoic faulting of the northern Tibetan Plateau margin from apatite (U–Th)/He ages: *Earth and Planetary Science Letters*, 296 (1-2), 78-88. Doi: 10.1016/j.epsl.2010.04.051.

Clark, M. K., & Royden, L. H. (2000), Topographic ooze: Building the eastern margin of Tibet by lower crustal flow: *Geology*, 28 (8), 703-706. Doi: 10.1130/0091-7613(2000)28<703:Tobtem>2.0.Co;2.

Craddock, W. H., Kirby, E., Harkins, N. W., Zhang, H., Shi, X., & Liu, J. (2010), Rapid fluvial incision along the Yellow River during headward basin integration: *Nature Geoscience*, 3 (3), 209-213. Doi: 10.1038/ngeo777.

Dai, S., Fang, X., Dupont-Nivet, G., Song, C., Gao, J., Krijgsman, W., Langereis, C., & Zhang, W. (2006), Magnetostratigraphy of Cenozoic sediments from the Xining Basin: Tectonic implications for the northeastern Tibetan Plateau: *Journal of Geophysical Research: Solid Earth*, 111 (B11). Doi: 10.1029/2005JB004187.

Dayem, K. E., Molnar, P., Clark, M. K., & Houseman, G. A. (2009), Far-field lithospheric deformation in Tibet during continental collision: *Tectonics*, 28 (6). Doi: 10.1029/2008TC002344.

Ding, L., Kapp, P., Cai, F., Garzione, C. N., Xiong, Z., Wang, H., & Wang, C. (2022), Timing and mechanisms of Tibetan Plateau uplift: *Nature Reviews Earth & Environment*, 3 (10), 652-667. Doi: 10.1038/s43017-022-00318-4.

Dupont-Nivet, G., Horton, B. K., Butler, R. F., Wang, J., Zhou, J., & Waanders, G. L. (2004), Paleogene clockwise tectonic rotation of the Xining-Lanzhou region, northeastern Tibetan Plateau: *Journal of Geophysical Research: Solid Earth*, 109 (B4). Doi: 10.1029/2003JB002620.

Duvall, A. R., Clark, M. K., Kirby, E., Farley, K. A., Craddock, W. H., Li, C., & Yuan, D.-Y. (2013), Low-temperature thermochronometry along the Kunlun and Haiyuan Faults, NE Tibetan Plateau: Evidence for kinematic change during late-stage orogenesis: *Tectonics*, 32 (5), 1190-1211. Doi: 10.1002/tect.20072.

England, P., & Houseman, G. (1989), Extension during continental convergence, with application to the Tibetan Plateau: *Journal of Geophysical Research*, 94 (B12). Doi: 10.1029/JB094iB12p17561.

Fan, L.-G., Meng, Q.-R., Wu, G.-L., Wei, H.-H., Du, Z.-M., & Wang, E. (2019), Paleogene crustal extension in the eastern segment of the NE Tibetan plateau: *Earth and Planetary Science Letters*, 514 (62-74. Doi: 10.1016/j.epsl.2019.02.036.

Fang, X., Dupont-Nivet, G., Wang, C., Song, C., Meng, Q., Zhang, W., Nie, J., Zhang, T., Mao, Z., & Chen, Y. (2020), Revised chronology of central Tibet uplift (Lunpola Basin): *Science Advances*, 6 (50), eaba7298. Doi: 10.1126/sciadv.aba7298.

Fox, M., Bodin, T., & Shuster, D. L. (2015), Abrupt changes in the rate of Andean Plateau uplift from reversible jump Markov Chain Monte Carlo inversion of river profiles: *Geomorphology*, 238 (1-14. Doi: 10.1016/j.geomorph.2015.02.022.

Goren, L., Fox, M., & Willett, S. D. (2014), Tectonics from fluvial topography using formal linear inversion: Theory and applications to the Inyo Mountains, California: *Journal of Geophysical Research: Earth Surface*, 119 (8), 1651-1681. Doi: 10.1002/2014jf003079.

Guerit, L., Yuan, X.-P., Carretier, S., Bonnet, S., Rohais, S., Braun, J., & Rouby, D. (2019), Fluvial landscape evolution controlled by the sediment deposition coefficient: Estimation from experimental and natural landscapes: *Geology*, 47 (9), 853-856. Doi: 10.1130/g46356.1.

Guo, Z., & Wilson, M. (2019), Late Oligocene–early Miocene transformation of postcollisional magmatism in Tibet: *Geology*, 47 (8), 776-780. Doi: 10.1130/g46147.1.

Guo, Z., Wilson, M., Dingwell, D. B., & Liu, J. (2021), India-Asia collision as a driver of atmospheric CO(2) in the Cenozoic: *Nature Communications*, 12 (1), 3891. Doi: 10.1038/s41467-021-23772-y.

Harkins, N., Kirby, E., Heimsath, A., Robinson, R., & Reiser, U. (2007), Transient fluvial incision in the headwaters of the Yellow River, northeastern Tibet, China: *Journal of Geophysical Research: Earth Surface*, 112 (F3). Doi: 10.1029/2006JF000570.

Hu, X., Pan, B., Kirby, E., Gao, H., Hu, Z., Cao, B., Geng, H., Li, Q., & Zhang, G. (2015), Rates and kinematics of active shortening along the eastern Qilian Shan, China, inferred from deformed fluvial terraces: *Tectonics*, 34 (12), 2478-2493. Doi: 10.1002/2015tc003978.

Hui, Z., Li, X., Ma, Z., Xiao, L., Zhang, J., & Chang, J. (2018), Miocene pollen assemblages from the Zeku Basin, northeastern Tibetan Plateau, and their palaeoecological and palaeoaltimetric implications: *Palaeogeography, Palaeoclimatology, Palaeoecology*, 511 (419-432. Doi: 10.1016/j.palaeo.2018.09.009.

Jammes, S., & Huismans, R. S. (2012), Structural styles of mountain building: Controls of lithospheric rheologic stratification and extensional inheritance: *Journal of Geophysical Research: Solid Earth*, 117 (B10). Doi: 10.1029/2012JB009376.

Jia, L., Hu, D., Wu, H., Zhao, X., Chang, P., You, B., Zhang, M., Wang, C., Ye, M., Wu, Z., & Liang, X. (2017), Yellow

River terrace sequences of the Gonghe–Guide section in the northeastern Qinghai–Tibet: Implications for plateau uplift: *Geomorphology*, 295 (323-336. Doi: 10.1016/j.geomorph.2017.06.007.

Karplus, M. S., Zhao, W., Klemperer, S. L., Wu, Z., Mechie, J., Shi, D., Brown, L. D., & Chen, C. (2011), Injection of Tibetan crust beneath the south Qaidam Basin: Evidence from INDEPTH IV wide-angle seismic data: *Journal of Geophysical Research*, 116 (B7). Doi: 10.1029/2010jb007911.

Kirby, E., & Harkins, N. (2013), Distributed deformation around the eastern tip of the Kunlun fault: *International Journal of Earth Sciences*, 102 (7), 1759-1772. Doi: 10.1007/s00531-013-0872-x.

Kirby, E., Whipple, K. X., Tang, W., & Chen, Z. (2003), Distribution of active rock uplift along the eastern margin of the Tibetan Plateau: Inferences from bedrock channel longitudinal profiles: *Journal of Geophysical Research: Solid Earth*, 108 (B4). Doi: 10.1029/2001jb000861.

Klaus, S., Morley, R. J., Plath, M., Zhang, Y.-P., & Li, J.-T. (2016), Biotic interchange between the Indian subcontinent and mainland Asia through time: *Nature Communications*, 7 (1), 12132. Doi: 10.1038/ncomms12132.

Kutzbach, J. E., Prell, W. L., & Ruddiman, W. F. (1993), Sensitivity of Eurasian Climate to Surface Uplift of the Tibetan Plateau: *The Journal of Geology*, 101 (2), 177-190. Doi: 10.1086/648215.

Lal, D., Harris, N. B. W., Sharma, K. K., Gu, Z., Ding, L., Liu, T., Dong, W., Caffee, M. W., & Jull, A. J. T. (2004), Erosion history of the Tibetan Plateau since the last interglacial: constraints from the first studies of cosmogenic 10Be from Tibetan bedrock: *Earth and Planetary Science Letters*, 217 (1), 33-42. Doi: 10.1016/S0012-821X(03)00600-9.

Law, R., & Allen, M. B. (2020), Diachronous Tibetan Plateau landscape evolution derived from lava field geomorphology: *Geology*, 48 (3), 263-267. Doi: 10.1130/g47196.1.

Le Pape, F., Jones, A. G., Vozar, J., & Wenbo, W. (2012), Penetration of crustal melt beyond the Kunlun Fault into northern Tibet: *Nature Geoscience*, 5 (5), 330-335. Doi: 10.1038/ngeo1449.

Lease, R. O., Burbank, D. W., Clark, M. K., Farley, K. A., Zheng, D., & Zhang, H. (2011), Middle Miocene reorganization of deformation along the northeastern Tibetan Plateau: *Geology*, 39 (4), 359-362. Doi: 10.1130/g31356.1.

Lease, R. O., Burbank, D. W., Zhang, H., Liu, J., & Yuan, D. (2012), Cenozoic shortening budget for the northeastern edge of the Tibetan Plateau: Is lower crustal flow necessary?: *Tectonics*, 31 (3). Doi: 10.1029/2011TC003066.

Li, B., Chen, X., Zuza, A. V., Hu, D., Ding, W., Huang, P., & Xu, S. (2019), Cenozoic cooling history of the North Qilian Shan, northern Tibetan Plateau, and the initiation of the Haiyuan fault: Constraints from apatite- and zircon-fission track thermochronology: *Tectonophysics*, 751 (109-124. Doi: 10.1016/j.tecto.2018.12.005.

Li, B., Feng, Q., Wang, X., Li, Z., Wang, F., Zhao, C., Yu, T., & Chen, W. (2023), Formation of the upper reaches of the Yellow River: Provenance evidence from the strata of the Yellow River sedimentary basin: *Global and Planetary Change*, 229 (104224. Doi: 10.1016/j.gloplacha.2023.104224.

Li, B., Wang, Y., Zuza, A. V., Chen, X., Shao, Z., Wang, Z.-Z., Sun, Y., & Wu, C. (2022), Cenozoic deformation in the eastern domain of the North Qaidam thrust belt, northern Tibetan Plateau: *GSA Bulletin*, 135 (1-2), 331-350. Doi: 10.1130/b36215.1.

Li, G., Pettke, T., & Chen, J. (2011), Increasing Nd isotopic ratio of Asian dust indicates progressive uplift of the north

Tibetan Plateau since the middle Miocene: *Geology*, 39 (3), 199-202. Doi: 10.1130/g31734.1.

Li, J., Fang, X., Song, C., Pan, B., Ma, Y., & Yan, M. (2014a), Late Miocene–Quaternary rapid stepwise uplift of the NE Tibetan Plateau and its effects on climatic and environmental changes: *Quaternary Research*, 81 (3), 400-423. Doi: 10.1016/j.yqres.2014.01.002.

Li, L., & Garzione, C. N. (2023), Upward and outward growth of north-central Tibet: Mechanisms that build high-elevation, low-relief plateaus: *Science Advances*, 9 (27), eadh3058. Doi: 10.1126/sciadv.adh3058.

Li, Y., Li, D., Liu, G., Harbor, J., Caffee, M., & Stroeven, A. P. (2014b), Patterns of landscape evolution on the central and northern Tibetan Plateau investigated using in-situ produced 10Be concentrations from river sediments: *Earth and Planetary Science Letters*, 398 (77-89. Doi: 10.1016/j.epsl.2014.04.045.

Liang, H. Y., Feng, Z. P., Pei, B., Li, Y., & Yang, X. T. (2018), Demographic expansion of two Tamarix species along the Yellow River caused by geological events and climate change in the Pleistocene: *Scientific Reports*, 8 (1), 60. Doi: 10.1038/s41598-017-19034-x.

Lin, A., Yang, Z., Sun, Z., & Yang, T. (2001), How and when did the Yellow River develop its square bend?: *Geology*, 9 (10), 951–954. Doi: 10.1130/0091-7613(2001)029<0951:HAWDTY>2.0.CO;2.

Liu, P. (2015), Spatio-temporal evolution of Northeastern Tibetan Plateau: integrated provenance study of the Guide, Lanzhou and Wushan-Tianshui basins [Doctor: Lanzhou University.

Lu, H., Fu, B., Shi, P., Ma, Y., & Li, H. (2016), Constraints on the uplift mechanism of northern Tibet: *Earth and Planetary Science Letters*, 453 (108-118. Doi: 10.1016/j.epsl.2016.08.010.

Märki, L., Lupker, M., France-Lanord, C., Lavé, J., Gallen, S., Gajurel, A. P., Haghipour, N., Leuenberger-West, F., & Eglinton, T. (2021), An unshakable carbon budget for the Himalaya: *Nature Geoscience*, 14 (10), 745-750. Doi: 10.1038/s41561-021-00815-z.

Medvedev, S., Beaumont, C., Law, R. D., Searle, M. P., & Godin, L. (2006), Growth of continental plateaus by channel injection: models designed to address constraints and thermomechanical consistency, Channel Flow, Ductile Extrusion and Exhumation in Continental Collision Zones, Volume 268, Geological Society of London, p. 147-164.

Miao, Y., Fang, X., Sun, J., Xiao, W., Yang, Y., Wang, X., Farnsworth, A., Huang, K., Ren, Y., Wu, F., Qiao, Q., Zhang, W., Meng, Q., Yan, X., Zheng, Z., Song, C., & Utescher, T. (2022), A new biologic paleoaltimetry indicating Late Miocene rapid uplift of northern Tibet Plateau: *Science*, 378 (6624), 1074-1079. Doi: doi:10.1126/science.abo2475.

Nie, J., Stevens, T., Rittner, M., Stockli, D., Garzanti, E., Limonta, M., Bird, A., Ando, S., Vermeesch, P., Saylor, J., Lu, H., Breecker, D., Hu, X., Liu, S., Resentini, A., Vezzoli, G., Peng, W., Carter, A., Ji, S., & Pan, B. (2015), Loess Plateau storage of Northeastern Tibetan Plateau-derived Yellow River sediment: *Nat Commun*, 6 (8511. Doi: 10.1038/ncomms9511.

Pan, B., Su, H., Hu, Z., Hu, X., Gao, H., Li, J., & Kirby, E. (2009), Evaluating the role of climate and tectonics during non-steady incision of the Yellow River: evidence from a 1.24Ma terrace record near Lanzhou, China: *Quaternary Science Reviews*, 28 (27), 3281-3290. Doi: 10.1016/j.quascirev.2009.09.003.

Perron, J. T., & Royden, L. (2013), An integral approach to bedrock river profile analysis: *Earth Surface Processes* *and Landforms*, 38 (6), 570-576. Doi: 10.1002/esp.3302.

Polissar, P. J., Freeman, K. H., Rowley, D. B., McInerney, F. A., & Currie, B. S. (2009), Paleoaltimetry of the Tibetan Plateau from D/H ratios of lipid biomarkers: *Earth and Planetary Science Letters*, 287 (1-2), 64-76. Doi: 10.1016/j.epsl.2009.07.037.

Pritchard, D., Roberts, G. G., White, N. J., & Richardson, C. N. (2009), Uplift histories from river profiles: *Geophysical Research Letters*, 36 (24). Doi: 10.1029/2009gl040928.

Racano, S., Schildgen, T. F., Cosentino, D., & Miller, S. R. (2021), Temporal and Spatial Variations in Rock Uplift From River-Profile Inversions at the Central Anatolian Plateau Southern Margin: *Journal of Geophysical Research: Earth Surface*, 126 (8), e2020JF006027. Doi: 10.1029/2020JF006027.

Reusser, L. J., Bierman, P. R., Pavich, M. J., Zen, E.-a., Larsen, J., & Finkel, R. (2004), Rapid Late Pleistocene Incision of Atlantic Passive-Margin River Gorges: *Science*, 305 (5683), 499-502. Doi: doi:10.1126/science.1097780.

Roberts, G. G., White, N. J., Martin-Brandis, G. L., & Crosby, A. G. (2012), An uplift history of the Colorado Plateau and its surroundings from inverse modeling of longitudinal river profiles: *Tectonics*, 31 (4), n/a-n/a. Doi: 10.1029/2012tc003107.

Rowley, D. B., & Currie, B. S. (2006), Palaeo-altimetry of the late Eocene to Miocene Lunpola basin, central Tibet: *Nature*, 439 (7077), 677-681. Doi: 10.1038/nature04506.

Royden, L. H., Burchfiel, B. C., King, R. W., Wang, E., Chen, Z., Shen, F., & Liu, Y. (1997), Surface Deformation and Lower Crustal Flow in Eastern Tibet: *Science*, 276 (5313), 788-790. Doi: 10.1126/science.276.5313.788.

Royden, L. H., Burchfiel, B. C., & van der Hilst, R. D. (2008), The geological evolution of the Tibetan Plateau: *Science*, 321 (5892), 1054-1058. Doi: 10.1126/science.1155371.

Shen, X., Braun, J., & Yuan, X. (2022), Southeastern margin of the Tibetan Plateau stopped expanding in the late Miocene: *Earth and Planetary Science Letters*, 583 (117446. Doi: 10.1016/j.epsl.2022.117446.

Staisch, L. M., Niemi, N. A., Clark, M. K., & Chang, H. (2016), Eocene to late Oligocene history of crustal shortening within the Hoh Xil Basin and implications for the uplift history of the northern Tibetan Plateau: *Tectonics*, 35 (4), 862-895. Doi: 10.1002/2015tc003972.

Su, Q., Wang, X., Yuan, D., Xie, H., Li, H., & Huang, X. (2023), Fluvial entrenchment of the Gonghe Basin and integration of the upper Yellow River - Evidence from the cosmogenically dated geomorphic surfaces: *Geomorphology*, 429 (Doi: 10.1016/j.geomorph.2023.108654.

Su, T., Farnsworth, A., Spicer, R. A., Huang, J., Wu, F.-X., Liu, J., Li, S.-F., Xing, Y.-W., Huang, Y.-J., Deng, W.-Y.-D., Tang, H., Xu, C.-L., Zhao, F., Srivastava, G., Valdes, P. J., Deng, T., & Zhou, Z.-K. (2019), No high Tibetan Plateau until the Neogene: *Science Advances*, 5 (3), eaav2189. Doi: 10.1126/sciadv.aav2189.

Sun, B., Wang, Y. F., Li, C. S., Yang, J., Li, J. F., Li, Y. L., Deng, T., Wang, S. Q., Zhao, M., Spicer, R. A., Ferguson, D. K., & Mehrotra, R. C. (2015), Early Miocene elevation in northern Tibet estimated by palaeobotanical evidence: *Scientific Reports*, 5 (10379. Doi: 10.1038/srep10379.

Tapponnier, P., Meyer, B., Avouac, J. P., Peltzer, G., Gaudemer, Y., Guo, S., Xiang, H., Yin, K., Chen, Z., Cai, S., & Dai, H. (1990), Active thrusting and folding in the Qilian Shan, and decoupling between upper crust and mantle in northeastern Tibet: *Earth and Planetary Science Letters*, 97 (3), 382-403. Doi: 10.1016/0012-821X(90)90053-

Z.

Tapponnier, P., Zhiqin, X., Roger, F., Meyer, B., Arnaud, N., Wittlinger, G., & Jingsui, Y. (2001), Oblique Stepwise Rise and Growth of the Tibet Plateau: *Science*, 294 (5547), 1671-1677. Doi: 10.1126/science.105978.

Unsworth, M., Wei, W., Jones, A., Li, S., Bedrosian, P., Booker, J., Jin, S., Deng, M., & Tan, H. (2004), Crustal and upper mantle structure of northern Tibet imaged with magnetotelluric data: *Journal of Geophysical Research-Solid Earth*, 109 (Doi: 10.1029/2002JB002305.

Wang, C., Dai, J., Zhao, X., Li, Y., Graham, S. A., He, D., Ran, B., & Meng, J. (2014), Outward-growth of the Tibetan Plateau during the Cenozoic: A review: *Tectonophysics*, 621 (1-43. Doi: 10.1016/j.tecto.2014.01.036.

Wang, W., Zhang, P., Garzione, C. N., Liu, C., Zhang, Z., Pang, J., Wang, Y., Zheng, D., Zheng, W., & Zhang, H. (2022), Pulsed rise and growth of the Tibetan Plateau to its northern margin since ca. 30 Ma: *Proc Natl Acad Sci U S A*, 119 (8). Doi: 10.1073/pnas.2120364119.

Wang, W., Zheng, D., Li, C., Wang, Y., Zhang, Z., Pang, J., Wang, Y., Yu, J., Wang, Y., Zheng, W., Zhang, H., & Zhang, P. (2020), Cenozoic Exhumation of the Qilian Shan in the Northeastern Tibetan Plateau: Evidence From Low-Temperature Thermochronology: *Tectonics*, 39 (4). Doi: 10.1029/2019tc005705.

Wang, W., Zheng, W., Zhang, P., Li, Q., Kirby, E., Yuan, D., Zheng, D., Liu, C., Wang, Z., Zhang, H., & Pang, J. (2017), Expansion of the Tibetan Plateau during the Neogene: *Nature Communications*, 8 (15887. Doi: 10.1038/ncomms15887.

Wang, X., Vandenberghe, J., Yi, S., Van Balen, R., & Lu, H. (2015), Climate-dependent fluvial architecture and processes on a suborbital timescale in areas of rapid tectonic uplift: An example from the NE Tibetan Plateau: *Global and Planetary Change*, 133 (318-329. Doi: 10.1016/j.gloplacha.2015.09.009.

Whipple, K. X., & Tucker, G. E. (1999), Dynamics of the stream-power river incision model: Implications for height limits of mountain ranges, landscape response timescales, and research needs: *Journal of Geophysical Research: Solid Earth*, 104 (B8), 17661-17674. Doi: 10.1029/1999jb900120.

Wolf, S. G., Huismans, R. S., Braun, J., & Yuan, X. (2022), Topography of mountain belts controlled by rheology and surface processes: *Nature*, 606 (7914), 516-521. Doi: 10.1038/s41586-022-04700-6.

Yan, M., VanderVoo, R., Fang, X.-m., Parés, J. M., & Rea, D. K. (2006), Paleomagnetic evidence for a mid-Miocene clockwise rotation of about 25° of the Guide Basin area in NE Tibet: *Earth and Planetary Science Letters*, 241 (1-2), 234-247. Doi: 10.1016/j.epsl.2005.10.013.

Yin, A., Dang, Y.-Q., Zhang, M., Chen, X.-H., & McRivette, M. W. (2008), Cenozoic tectonic evolution of the Qaidam basin and its surrounding regions (Part 3): Structural geology, sedimentation, and regional tectonic reconstruction: *GSA Bulletin*, 120 (7-8), 847-876. Doi: 10.1130/b26232.1.

Yin, A., & Harrison, T. M. (2000), Geologic Evolution of the Himalayan-Tibetan Orogen: *Annual Review of Earth and Planetary Sciences*, 28 (1), 211-280. Doi: 10.1146/annurev.earth.28.1.211.

Yu, J., Zheng, D., Wang, W., Pang, J., Li, C., Wang, Y., Hao, Y., Zhang, H., & Zhang, P. (2023), Cenozoic tectonic development in the northeastern Tibetan Plateau: Evidence from thermochronological and sedimentological records: *Global and Planetary Change*, 224 (104098. Doi: 10.1016/j.gloplacha.2023.104098.

Yuan, D. Y., Champagnac, J. D., Ge, W. P., Molnar, P., Zhang, P. Z., Zheng, W. J., Zhang, H. P., & Liu, X. W. (2011), Late Quaternary right-lateral slip rates of faults adjacent to the lake Qinghai, northeastern margin of the Tibetan Plateau: *Geological Society of America Bulletin*, 123 (9-10), 2016-2030. Doi: 10.1130/b30315.1.

Yuan, D. Y., Ge, W. P., Chen, Z. W., Li, C. Y., Wang, Z. C., Zhang, H. P., Zhang, P. Z., Zheng, D. W., Zheng, W. J., Craddock, W. H., Dayem, K. E., Duvall, A. R., Hough, B. G., Lease, R. O., Champagnac, J. D., Burbank, D. W., Clark, M. K., Farley, K. A., Garzione, C. N., Kirby, E., Molnar, P., & Roe, G. H. (2013), The growth of northeastern Tibet and its relevance to large-scale continental geodynamics: A review of recent studies: *Tectonics*, 32 (5), 1358-1370. Doi: 10.1002/tect.20081.

Yuan, X. P., Braun, J., Guerit, L., Rouby, D., & Cordonnier, G. (2019), A New Efficient Method to Solve the Stream Power Law Model Taking Into Account Sediment Deposition: *Journal of Geophysical Research: Earth Surface*, 124 (6), 1346-1365. Doi: 10.1029/2018jf004867.

Yuan, X. P., Huppert, K. L., Braun, J., Shen, X., Liu-Zeng, J., Guerit, L., Wolf, S. G., Zhang, J. F., & Jolivet, M. (2021), Propagating uplift controls on high-elevation, low-relief landscape formation in the southeast Tibetan Plateau: *Geology*, 50 (1), 60-65. Doi: 10.1130/g49022.1.

Yuan, X. P., Jiao, R., Dupont-Nivet, G., & Shen, X. (2022), Southeastern Tibetan Plateau Growth Revealed by Inverse Analysis of Landscape Evolution Model: *Geophysical Research Letters*, 49 (10). Doi: 10.1029/2021gl097623.

Yuan, X. P., Jiao, R., Liu-Zeng, J., Dupont-Nivet, G., Wolf, S. G., & Shen, X. (2023), Downstream propagation of fluvial erosion in Eastern Tibet: *Earth and Planetary Science Letters*, 605 (Doi: 10.1016/j.epsl.2023.118017.

Zhang, H., Kirby, E., Pitlick, J., Anderson, R. S., & Zhang, P. (2017a), Characterizing the transient geomorphic response to base-level fall in the northeastern Tibetan Plateau: *Journal of Geophysical Research: Earth Surface*, 122 (2), 546-572. Doi: 10.1002/2015JF003715.

Zhang, H., Zhang, P., Champagnac, J. D., Molnar, P., Anderson, R. S., Kirby, E., Craddock, W. H., & Liu, S. (2014), Pleistocene drainage reorganization driven by the isostatic response to deep incision into the northeastern Tibetan Plateau: *Geology*, 42 (4), 303-306. Doi: 10.1130/g35115.1.

Zhang, P., Burchfiel, B. C., Molnar, P., Zhang, W., Jiao, D., Deng, Q., Wang, Y., Royden, L., & Song, F. (1991), Amount and style of Late Cenozoic Deformation in the Liupan Shan Area, Ningxia Autonomous Region, China: *Tectonics*, 10 (6), 1111-1129. Doi: 10.1029/90TC02686.

Zhang, W., Zhang, T., Song, C., Erwin, A., Mao, Z., Yahui, F., Yin, L., Qingquan, M., Rongsheng, Y., Dawen, Z., Bingshuai, L., & Jiao, L. (2017b), Termination of fluvial-alluvial sedimentation in the Xining Basin, NE Tibetan Plateau, and its subsequent geomorphic evolution: *Geomorphology*, 297 (86-99. Doi: 10.1016/j.geomorph.2017.09.008.

Zhang, Y., Zhang, H., Ma, Z., Wang, Y., & Zhao, X. (2023), Inversion of Late Miocene uplift history from the transient Daxia River landscape, NE Tibetan Plateau: *Journal of the Geological Society*, 180 (6). Doi: 10.1144/jgs2023-030.

Zhao, Y., Fan, N., Nie, J., Abell, J. T., An, Y., Jin, Z., Wang, C., Zhang, J., Liu, X., & Nie, R. (2023), From Desiccation to Re-Integration of the Yellow River Since the Last Glaciation: *Geophysical Research Letters*, 50 (15), e2023GL103632. Doi: 10.1029/2023GL103632.

Zheng, D., Zhang, P.-Z., Wan, J., Yuan, D., Li, C., Yin, G., Zhang, G., Wang, Z., Min, W., & Chen, J. (2006), Rapid exhumation at ~8 Ma on the Liupan Shan thrust fault from apatite fission-track thermochronology: Implications for growth of the northeastern Tibetan Plateau margin: *Earth and Planetary Science Letters*, 248 (1-2), 198-208. Doi: 10.1016/j.epsl.2006.05.023.

Zhuang, G., Brandon, M. T., Pagani, M., & Krishnan, S. (2014), Leaf wax stable isotopes from Northern Tibetan Plateau: Implications for uplift and climate since 15 Ma: *Earth and Planetary Science Letters*, 390 (186-198. Doi: 10.1016/j.epsl.2014.01.003.

Zuza, A. V., Cheng, X., & Yin, A. (2016), Testing models of Tibetan Plateau formation with Cenozoic shortening estimates across the Qilian Shan–Nan Shan thrust belt: *Geosphere*, 12 (2), 501-532. Doi: 10.1130/ges01254.1.

Reconciling the long-term growth of the Northeastern Tibetan Plateau and the upstream Yellow River profile

X. He[1], X. P. Yuan[1*], C. Q. He[2], X. Y. Wang[3], and X. M. Shen[4]

[1]Hubei Key Laboratory of Critical Zone Evolution, School of Earth Sciences, China University of Geosciences, Wuhan, China.

[2]Department of Earth, Atmospheric and Planetary Science, Massachusetts Institute of Technology, Cambridge, USA.

[3]School of Geography and Ocean Science, Nanjing University, Nanjing, China.

[4]National Institute of Natural Hazards, Ministry of Emergency Management of China, Beijing, China

[*]Corresponding author: Xiaoping Yuan (yuanxiaoping@cug.edu.cn)

Key Points:

- The long-term growth of the Northeastern Tibetan Plateau is investigated by a landscape evolution model with two growth scenarios.
- The Northeastern Tibetan Plateau experienced an early block uplift (~20-12 Ma) and a late outward propagation uplift (~12-0 Ma).
- Our model results reconcile the long-term growth of the Northeastern Tibetan Plateau and the upstream Yellow River profile.

Abstract

The growth history of the Northeastern Tibetan Plateau (NETP) is enigmatic, with debates on when and how the NETP significantly uplifted. Here, we use a numerical landscape evolution model to quantitatively investigate the ~20 Ma growth history of the NETP by studying the formation history of the upstream Yellow River (UYR). Compared to the observed river profiles, erosion rates, the trend of acceleration time of deformation, and paleo-elevation, our modeling results suggest that the long-term growth history of the NETP consists of an early block uplift (~20-12 Ma) and a late outward propagation uplift (~12-0 Ma). Before ~12 Ma (middle Miocene), the NETP was uplifted via a block growth, with major uplift in the south part. Subsequently, the high (~5 km) NETP has been uplifted via a northward propagation growth until the present-day time. We further suggest that pure headward erosion unlikely formed the observed river profile of the UYR over the past few million years. Our modeling thus reconciles the long-term outward growth of the NETP and the UYR profile, suggesting a downstream migration of high erosion rates, which is fundamentally different from the headward erosion of small mountain rivers. The downstream propagation of fluvial erosion may commonly occur in the outward-growing plateau on Earth.

Plain Language Summary

Mountain rivers with their river profiles can record the long-term growth history of orogen. The Yellow River, the sixth longest river in the world, flows through the Northeastern Tibetan Plateau. The upstream Yellow River profile provides an opportunity to quantitatively investigate the controversial growth history of the Northeastern Tibetan Plateau. We study the formation history of the Northeastern Tibetan Plateau by a numerical landscape evolution model combining with two possible growth scenarios. Reconciling the long-term growth of the Northeastern Tibetan Plateau and the upstream Yellow River profile, our modeled results show that the Northeastern Tibetan Plateau experienced an early block uplift (~20-12 Ma) and a late outward propagation uplift (~12-0 Ma). Furthermore, the observed upstream Yellow River profile is unlikely formed by pure headward erosion over the past few million years indicated by previous studies. This work further suggests that the downstream migration pattern of high erosion rates commonly exists in tectonically active outward-growing plateaus on Earth.

1 Introduction

The Indian-Eurasian continent-continent collision (since ~55 Ma) controls the long-term growth history of the Tibetan Plateau (Yin and Harrison, 2000), influencing Asian climate change (An et al., 2001; Kutzbach et al., 1993), landscape evolution in Asia (Law and Allen, 2020; Shen et al., 2022; Yuan et al., 2021), biodiversity (Klaus et al., 2016), and carbon cycle (Guo et al., 2021; Märki et al., 2021). The critical evidence for the above research is related to when and how the Tibetan Plateau grew. However, the timing of reaching the present-day high elevations (Fang et al., 2020; Rowley and Currie, 2006; Su et al., 2019) and the mechanism of the plateau growth (Clark and Royden, 2000; England and Houseman, 1989; Royden et al., 1997; Tapponnier et al., 2001) remain highly debated.

With the growth of the Tibetan Plateau, the growth history of the NETP is still in dispute. Some researchers suggest that the Indian-Eurasian collision (since ~55 Ma) influenced the NETP soon after the collision (Clark et al., 2010; Dupont-Nivet et al., 2004), but the influences are thought to be only an immediate response to the far-field effect of collision (Dayem et al., 2009). Significant tectonic deformation and uplift of the NETP did not occur long time after the collision (Dai et al., 2006; Wang et al., 2017, 2022). For example, various sediment accumulation rates indicate that the Xining basin (Figure 1b) initiated at 55-52.5 Ma, but most tectonic activities occurred after 17 Ma (Dai et al., 2006). In the Qaidam Basin (Figure 1b), Cenozoic sediments initiated at ~25.5 Ma based on magnetostratigraphy and mammalian biostratigraphy (Wang et al., 2017), and ~30 Ma based on magnetostratigraphies combined with detrital apatite fission-track ages (Wang et al., 2022). Moreover, the initially significant activity ages in the NETP were near the Miocene (~23-5.3 Ma) (Duvall et al., 2013; Lease et al., 2011; Li et al., 2019, 2022; Yuan et al., 2011; Zhang et al., 1991; Zheng et al., 2006), and became younger to the northeast (Figure 1b, c). Additionally, how the NETP uplifted is still unclear, with contrasting views including the stepwise block extrusion and uplift to the north (Tapponnier et al., 2001) and the progressive propagation uplift to the north via the lower crustal flow (Clark and Royden, 2000).

Mountain rivers form along with the growth of orogens, thus the longitudinal river profiles can record the long-term orogenic growth history (Allen, 2008; Goren et al., 2014; Kirby et al., 2003; Pritchard et al., 2009; Whipple and Tucker, 1999). Examples include the southeastern Tibetan Plateau (Yuan et al., 2022), the Andes Orogen (Fox et al., 2015), the Anatolian Plateau (Racano et al., 2021), and the Colorado Plateau (Roberts et al., 2012). The Yellow River, the sixth longest river in the world, flows through the NETP (Figure 1), and the UYR likely recorded the long-term growth history of the NETP. Although there are still some debates on the formation time (Craddock et al., 2010; Lin et al., 2001) and the formation process (Craddock et al., 2010; Lin et al., 2001) of the UYR, its longitudinal profile offers an opportunity to reconstruct the NETP growth history by reproducing the UYR river profile.

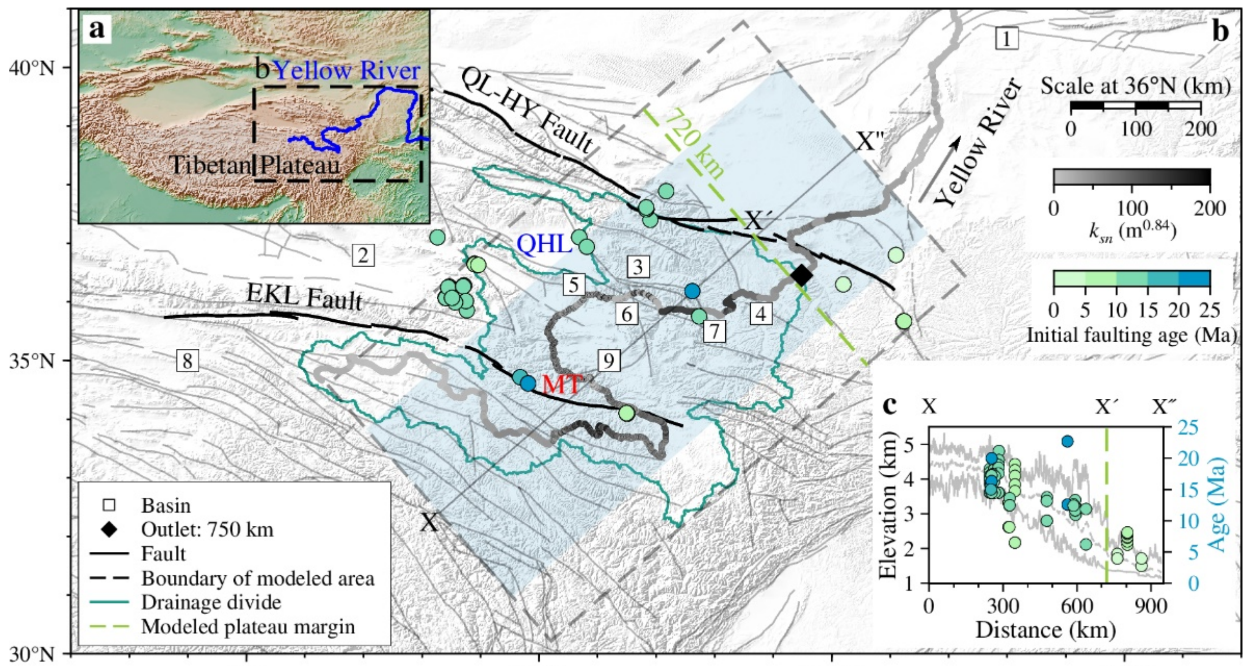

Figure 1. Geological and topographical background of the study area. (a) Topography of the Tibetan Plateau. (b) Closer view of the study area with the Yellow River in the Northeastern Tibetan Plateau. The trunk of the Yellow River is colored with the channel steepness $k_{sn} = SA^{m/n}$ with $m/n = 0.42$ (Harkins et al., 2007). QL-HY Fault: Qilian-Haiyuan Fault; EKL Fault: East Kunlun Fault; QHL: Qinghai Lake; MT: Anyemaqen Shan. Basins (square with black frames) are in (b): (1) Hetao Basin, (2) Qaidam Basin, (3) Xining Basin, (4) Lanzhou Basin, (5) Gonghe Basin, (6) Guide Basin, (7) Linxia Basin, (8) Hoh Xil Basin, and (9) Zeku Basin. The initially significant activity ages (Table S1) are from references (Duvall et al., 2013; Lease et al., 2011; Li et al., 2019, 2022; Yuan et al., 2011; Zhang et al., 1991; Zheng et al., 2006). (c) The swath profile plots (maximum, average, and minimum elevations) are based on the blue shading area in (b) with initially significant activity ages. The modeled area is 950 × 600 km^2. The width of the swath profile is 400 km. The green dashed line at 720 km indicates the plateau margin. The black arrow shows the direction of river flow.

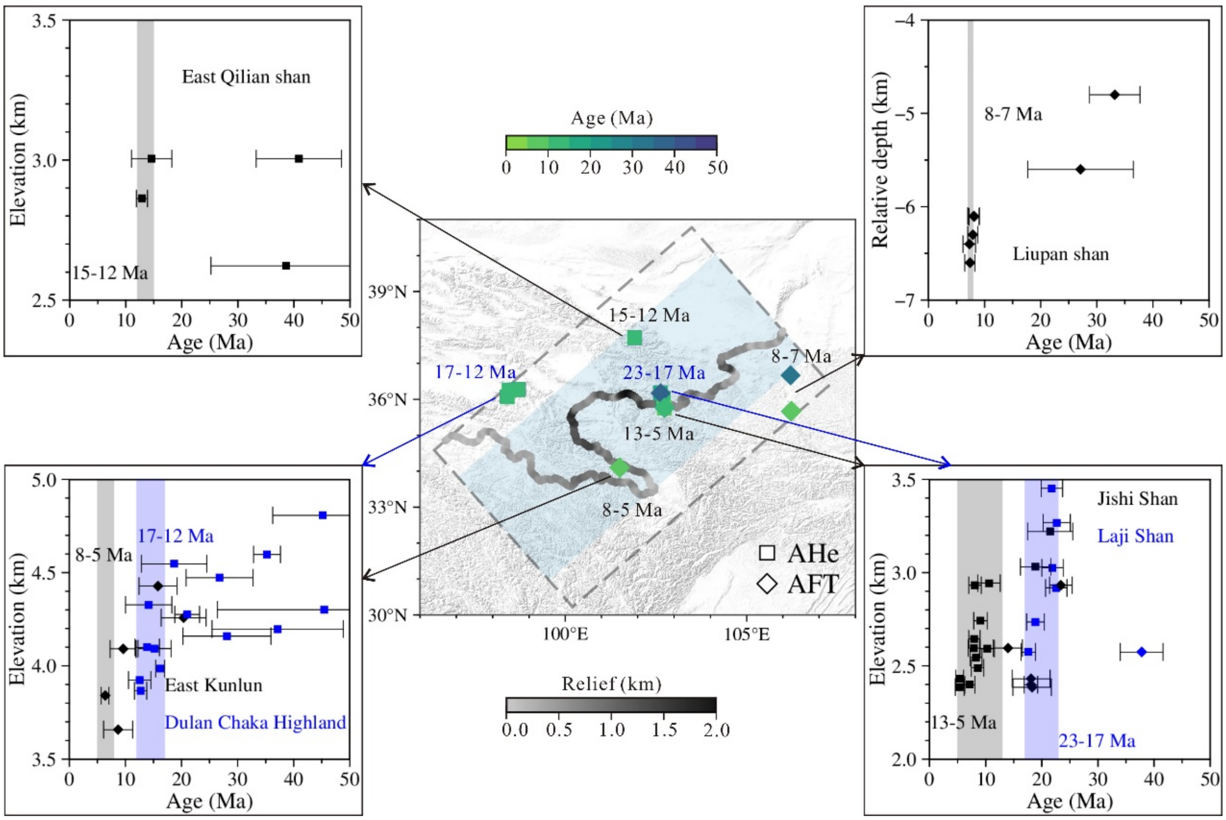

Figure 2. Thermochronometric ages and age-elevation relationships in the Northeastern Tibetan Plateau. AHe: Apatite (U-Th)/He; AFT: Apatite Fission Track. Thermochronometric ages (Table S2) are from references (Duvall et al., 2013; Lease et al., 2011; Wang et al., 2020; Zheng et al., 2006). The relief is calculated based on the difference between maximum and minimum elevations in the blue shading area.

This work aims to quantitatively study the ~20 Ma NETP growth history and the UYR formation history based on a numerical landscape evolution model (FastScape) (Braun and Willett, 2013; Yuan et al., 2019). In the NETP, we collected geomorphic data (e.g., river profile, swath profile, and relief), erosion rates, and the trend of acceleration times of deformation (e.g., initially significant activity ages and thermochronometric age-elevation relationships; Figures 1c and 2). In section 2, we propose two potential growth scenarios for the NETP growth, and then modify the numerical model to combine with two growth scenarios and several free parameters. In section 3, we test 2352 simulations with three free parameters to extract the modeled river profiles of each model. Based on the match of the observed and modeled river profiles, we obtain one of the best-fit modeled results in each growth model. Section 4 shows the NETP growth model by comparing the observed and modeled results, including the longitudinal river profiles, swath profiles, erosion rates, and the trend of acceleration times of deformation (e.g., initially significant activity ages and thermochronometric age-elevation relationships). Based on the modeled and observed results, we discuss the NETP growth history together with the UYR formation history. Furthermore, we test our results against a possibly formed UYR with a retreat process and period of pure headward erosion.

2. Methods

2.1 Landscape evolution model

The landscape evolution model FastScape (Braun and Willett, 2013; Yuan et al., 2019) is used to simulate the uplift, fluvial erosion, and sediment transport and deposition processes in the drainage basin of the UYR as

$$\frac{\partial h}{\partial t} = U - K_f \tilde{p}^m A^m S^n + \frac{G}{\tilde{p}A}\int_A \left(U - \frac{\partial h}{\partial t}\right) dA\,, \tag{1}$$

where h is the elevation, t is the time, U is the tectonic uplift rate, K_f is the erodibility, A is the drainage area, S is the local slope in the steepest-descent direction of water flow, m is the area exponent, and n is the slope exponent. Dimensionless $\tilde{p}$ represents any spatial or temporal variation in precipitation relative to the mean precipitation rate. Dimensionless G scales the deposition coefficient. To simplify the model, the dimensionless $\tilde{p}$ is assumed uniform ($\tilde{p}$ = 1), and the dimensionless G is assumed uniform (G = 1; Guerit et al., 2019; Yuan et al., 2019). We use the slope exponent $n = 1$ and $m = 0.42$ (i.e., m/n = 0.42) based on previous studies (e.g., Harkins et al., 2007). Although Harkins et al. (2007) suggest the slope exponent n is less than unity, for values of $n \neq 1$, there are some trade-offs between K_f and n (Goren et al., 2014), which should not influence the main results of our modeling (Yuan et al., 2022).

2.2 Two growth models for the Northeastern Tibetan Plateau

We apply two double-stage growth models, including a two-block stage (block-block) growth model and a block-propagation growth model (Figure 3), to explore the ~20 Ma NETP growth history. The first model is consistent with the two-stage stepwise uplift in the NETP (Tapponnier et al., 2001). The latter model is inspired by various orogenic growth models, which suggest mountain belts growing to a certain height, and then expanding laterally in an outward growth sequence characterized by a more successive marginal uplift (Jammes and Huismans, 2012; Wolf et al., 2022; Yuan et al., 2021), e.g., the outward growth of the Tibetan Plateau (Wang et al., 2014). The two growth models for the NETP with several free parameters simulate various uplift cases that predict different topographic evolutions (Figure 3). The two double-stage growth models for the NETP are likely the simplest plausible scenarios to produce our modeled results, without taking into account the complexities of the NETP, such as the influences of the strike-slip faults on the rock uplift (Tapponnier et al., 2001).

We use a logistic function of elevation (h_f) from the previous study (Yuan et al., 2021) to match the present-day maximum topography of the NETP as

$$h_f(x, L) = \frac{h_0}{1+e^{[(x-L)/W]}}, \tag{2}$$

where h_0 is the present-day maximum elevation, W is the characteristic width of the plateau margin, L is the total length of the plateau, and x is the distance to the plateau margin.

For the first stage of block uplift (Figure 3a, b), the uplift rate is

$$U_{1\mathrm{B}} = (h_{1\mathrm{B}}(x, L_{1\mathrm{B}}) - h_i)/t_{1\mathrm{B}}\,, \text{ with } h_{1\mathrm{B}}(x, L_{1\mathrm{B}}) = \frac{h_0}{1+e^{(x-L_{1\mathrm{B}})/W}}, \tag{3}$$

where h_i is the initial elevation before the block uplift, $L_{1\mathrm{B}}$ and $t_{1\mathrm{B}}$ are the length and duration of the first block uplift stage, respectively. For the second stage of block uplift (Figure 3a), the uplift rate is

$$U_{2\mathrm{B}} = \left[h_f(x, L) - h_{1\mathrm{B}}(x, L_{1\mathrm{B}})\right]/t_{2\mathrm{B}}\,, \tag{4}$$

where $t_{2\mathrm{B}}$ is the duration of the second block uplift stage. For the second stage of propagating uplift (Figure 3b), the uplift rate modified from Yuan et al. (2021) is

$$U_{2\mathrm{P}} = \frac{h_0 v_0 e^{(x-x_0)/W}}{W\left[1+e^{(x-x_0)/W}\right]^2}, \text{ with } x_0 = L_{1\mathrm{B}} + v_0 t\,, \tag{5}$$

where x_0 and v_0 are the growth length and growth velocity ($v_0 = (L - L_{1\mathrm{B}})/t_{2\mathrm{B}}$), respectively.

The uplift rate U in equation (1) is replaced by $U_{1\mathrm{B}}$, $U_{2\mathrm{B}}$, and $U_{2\mathrm{P}}$ for the block growth and propagation growth model. According to the above equations, uplift rates ($U_{1\mathrm{B}}$, $U_{2\mathrm{B}}$, and $U_{2\mathrm{P}}$) depend much on the growth duration ($t_{1\mathrm{B}}$) and distance ($L_{1\mathrm{B}}$). Thus, there are only three free parameters (i.e., K_f, $x_{1\mathrm{B}}$, and $t_{1\mathrm{B}}$) for each growth model.

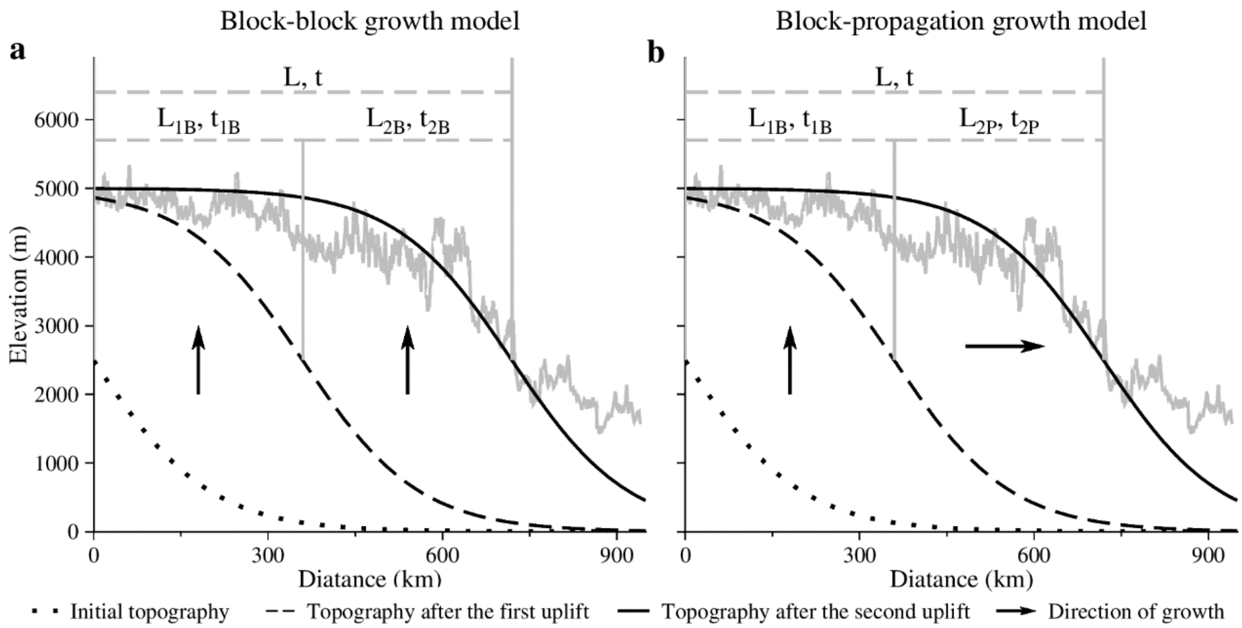

Figure 3. Diagrams for two growth models. (a) Block-block growth model. (b) Block-propagation growth model. Grey curves are the observed maximum topography within the blue shading area in Figure 1b. The present-day topography can be matched by a function in equation (2) (dark solid curve). L_{1B} and t_{1B} are the distance and duration of the first block growth, respectively. L_{2B} and t_{2B} are the distance and duration of the second block growth, respectively. L_{2P} and t_{2P} are the distance and duration of the second propagation growth, respectively. The block growth uplifts vertically, and the propagation model grows horizontally.

2.3 Model setup

In the NETP, the initially significant activity ages are younger than ~20 Ma (Figure 1b, c) (Duvall et al., 2013; Lease et al., 2011; Li et al., 2019, 2022; Yuan et al., 2011; Zhang et al., 1991; Zheng et al., 2006), and the modern high elevation was reached within ~23-11 Ma (Ding et al., 2022; Miao et al., 2022). Thus, we set the total growth duration of the two-stage uplift to 20 Myr ($t = t_1 + t_2 = 20$ Myr) cover the maximum growth age of the NETP. The total growth distance of the two-stage uplift is set to 720 km ($L = L_1 + L_2 = 720$ km) in our growth models, based on the present-day topography from the plateau interior to the plateau margin (near the Haiyuan Fault, Figure 1b, c).

To fit the present-day maximum topography of the NETP (equation 2), we set the maximum elevation to 5 km (i.e., $h_0 = 5$ km), and the characteristic width of propagation uplift to 100 km (i.e., $W = 100$ km). To model landscape evolution in the NETP, we define a rectangular domain size of 950 × 600 km (Figure 1b) with each node size of 1 × 1 km, and run the model for 20 Myr. To increase modeling efficiency, we use a time step length of 100,000 years to find one of the best-fit models and a time step length of 10,000 years to extract information from the best-fit model. The modeled river profiles are similar by testing different time steps from 10,000 to 100,000 years (Figure S1). In the NETP, initial elevations (0-2500 m) with maximum elevations in the model south boundary (Figure 3) and random white noise (≤ 500 m) are assumed, based on the maximum elevations were ~2500 ± 500 m at ~20 Ma near the south of the modeled area (Polissar et al., 2009; Sun et al., 2015).

2.4 Misfit function

The forward analyses of the landscape evolution model are used to explore the multidimensional space of free parameters (i.e., K_f, $x_{1\mathrm{B}}$, and $t_{1\mathrm{B}}$). Optimum values are found when the modeled river profile best matches the observed river profile of the UYR in the NETP. A parameter of χ was used to normalize the river profiles (Perron and Royden, 2013) at the point x:

$$\chi(x) = \int_{x_b}^{x} \left(\frac{A_0}{A(x)}\right)^{m/n} dx \,, \quad (4)$$

where x_b is the base level (outlet: 750 km; Figure 1b), A_0 (= 1 m^2) is a reference drainage area, and $A(x)$ is the drainage area of the point x. We first calculate the observed χ_i^{obs} values of the UYR at each elevation bin h_i (i = 1, 2, …, N). Then, at the final step of the model, we obtain the modeled trunks (i.e., the longest channel of each modeled basin), and calculate the modeled χ_i^{mod} values at the corresponding elevation bin h_i.

Table 1. Free parameters range in the forward analysis.

Growth model	K_f (× 10^{-7} $m^{0.16}$/yr)		L_{1B}(km)		t_{1B}(Myr)	
	Model range	Interval	Model range	Interval	Model range	Interval
Block-block growth model (Figure 3a)	15-41	2	0-700	100	0-20	1
Block-propagation growth model (Figure 3b)	15-41	2	0-700	100	0-20	1

An average misfit (μ) function compared the χ of modeled and observed river profiles:

$$\mu = \frac{1}{N_t}\sqrt{\frac{1}{N}\sum_{i=1}^{N}\frac{\left(\chi_i^{obs}-\chi_i^{mod}\right)^2}{(\delta_x)^2}}, \quad (5)$$

where δ_x (= 8 m) is the uncertainty for the χ comparison set arbitrary, N_t is the total number of all modeled trunks in the final step. For each growth model, 2352 (14 × 8 × 21) forward process models are used to constrain the best-fit sets of three free parameters (Table 1).

3 Results

We plot the misfit values μ ($log_{10}(\mu) < 2.0$) of the two growth models for three free parameters (K_f, $x_{1\mathrm{B}}$, and $t_{1\mathrm{B}}$) with different colors (Figures 4 and S2). The best-fit value of the block-block growth model is higher than that of the block-propagation growth model. In the low $log_{10}(\mu) < 0$ values (i.e., the best-fit models within uncertainty) of the block-block growth model, the distances (L_{1B}) and durations (t_{1B}) are less than 500 km and 15 Myr, respectively. The smallest $log_{10}(\mu)$ value is −0.335 marked by the black box in Figure 4a (K_f = 29 × 10^{-7} $\mathrm{m}^{0.16}$/yr, L_{1B} = 100 km, and t_{1B} = 5 Myr). There is no modeled river profile (χ-elevation plots) matching well the observed river profile for the block-block growth model, even the best-fit modeled results (Figure 5a). In the low $log_{10}(\mu) < 0$ of the block-propagation growth model, the distances (L_{1B}) and the durations (t_{1B}) are less than 500 km and 17 Myr, respectively. The smallest $log_{10}(\mu)$ value is −0.439 marked by the black box in Figure 4b (K_f = 21 × 10^{-7} $\mathrm{m}^{0.16}$/yr, L_{1B} = 100 km, and t_{1B} = 8 Myr). Several best-fit modeled river profiles matched the observed river profile well for the block-propagation growth model (Figure 5b).

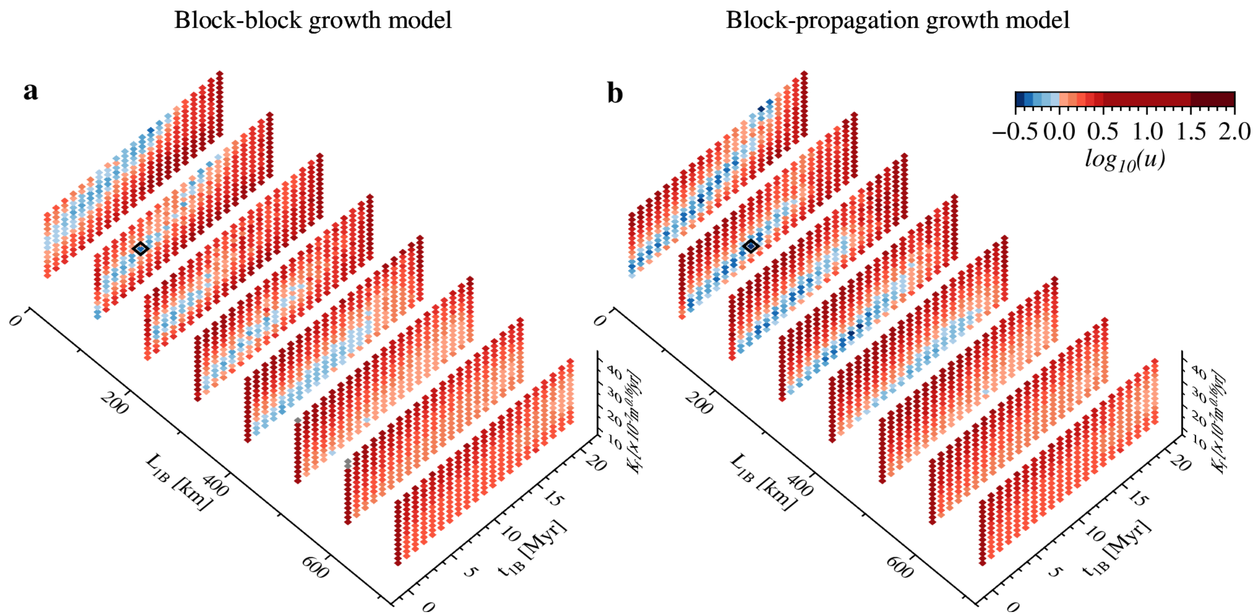

Figure 4. Modeled misfits of two growth models with each model 2352 forward analyses. (a) Block-block growth model. A black box marks one of the best-fit parameter sets (K_f = 29 × 10^{-7} $m^{0.16}$/yr, L_{1B} = 100 km, and t_{1B} = 5 Myr), and the smallest $log_{10}(\mu)$ value is −0.335. (b) Block-propagation growth model. A black box shows one of the best-fit parameter sets (K_f = 21 × 10^{-7} $m^{0.16}$/yr, L_{1B} = 100 km, and t_{1B} = 8 Myr), and the smallest $log_{10}(\mu)$ value is −0.439.

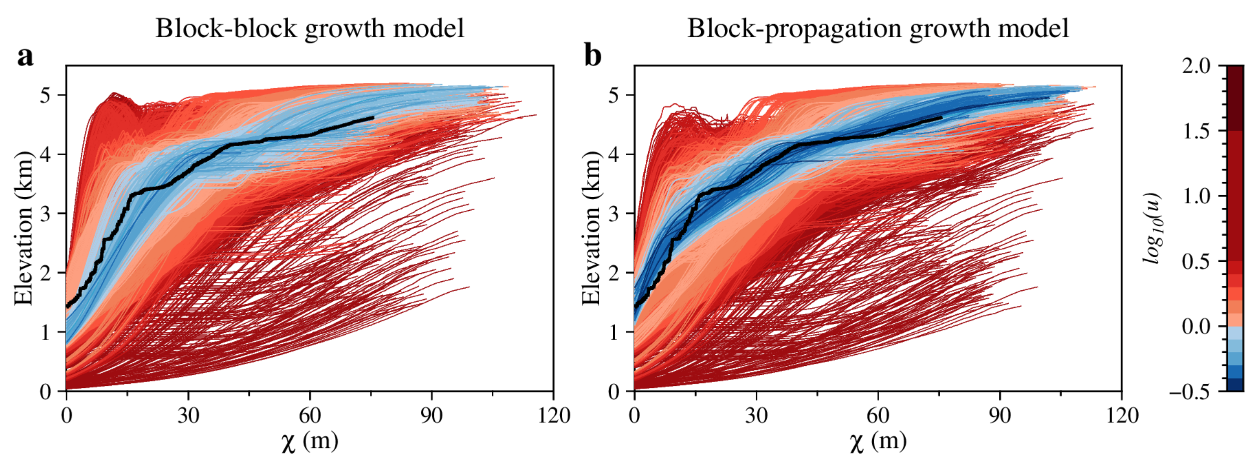

Figure 5. Modeled (colored) and observed (black) river profiles are plotted by χ. (a) In the block-block growth model, the modeled river profiles are less consistent with the observed river profile of the upstream Yellow River. (b) In the block-propagation growth model, several modeled river profiles with dark blue color matched well the observed river profile of the upstream Yellow River. The cooler the color, the lower the misfit values, and the better the modeling results.

4 Discussion

4.1 The best-fit growth model of the Northeastern Tibetan Plateau

This section compares one of the best-fit modeled results in each growth model to the observed results. χ-elevation plots are extracted from modeled trunks and the UYR. Although the modeled river profiles in each growth model are consistent with the upper reach of the observed river profile (with elevations >3500 m), only the modeled river profiles in the block-propagation growth model are consistent with the lower reach of the observed river profile (Figure 6b, e). In addition, the observed and modeled swath profiles of the block-propagation growth model are more consistent than that of the block-block growth model (Figure 6c, f).

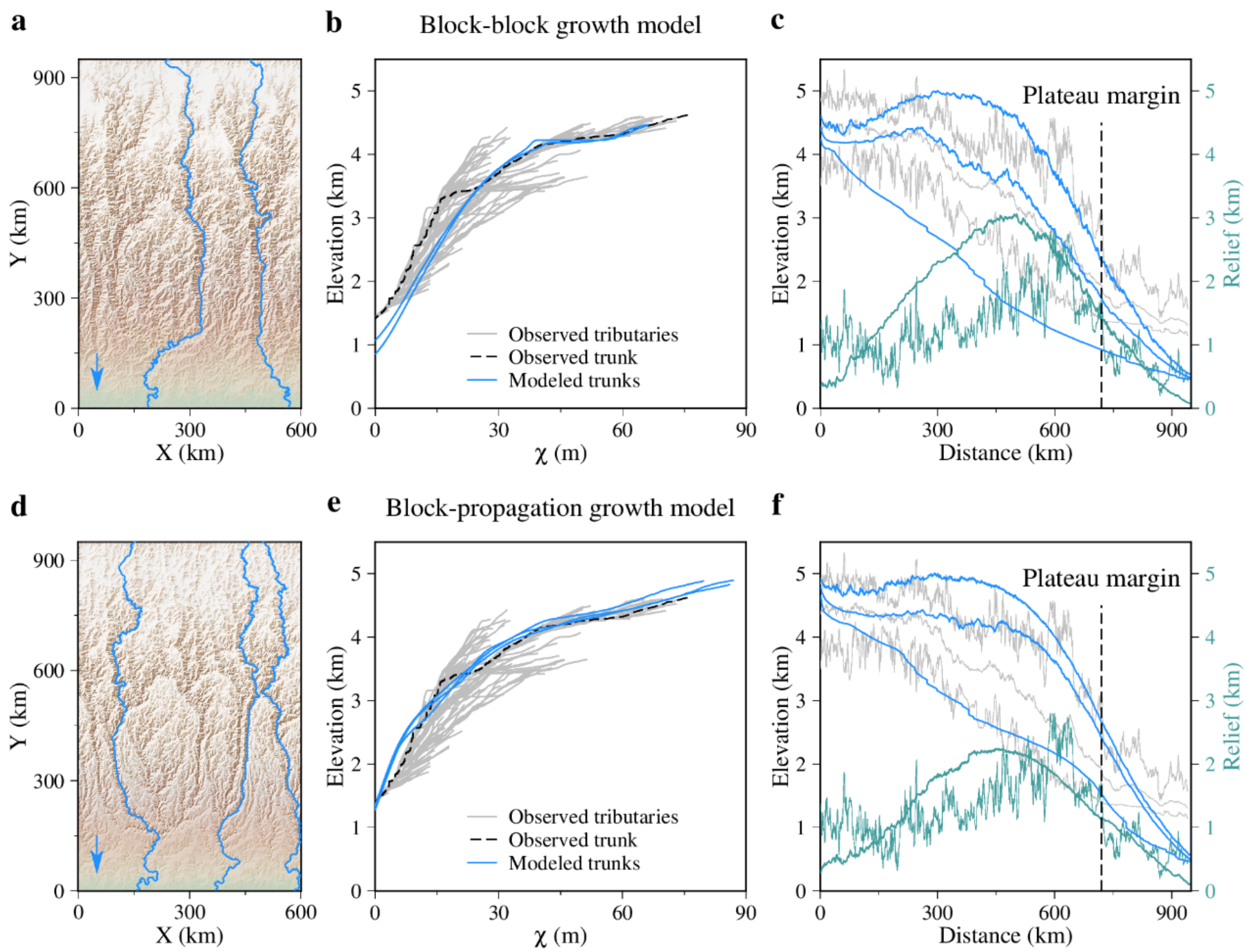

Figure 6. The comparison of geomorphic data between the best-fit model results of each growth model and the upstream Yellow River. (a, d) Modeled landscapes and trunks (blue lines). Blue arrows mark river directions. (b, e) χ-elevation plots. (c, f) Modeled and observed swaths and relief extracted from the whole

modeled domain and the blue shading area of the Northeastern Tibetan Plateau in Figure 1b, respectively. The modeled trunks are the longest channels of each modeled basin. Grey and black lines are the observed results, and blue lines are the modeled results in (b), (c), (e), and (f). In (c) and (f), green lines are the relief.

The modeled erosion rates and the trend of acceleration times of deformation are also compared to the observed results. Modeled erosion rates from the block-propagation growth model can better match most erosion rates from the plateau interior to the plateau margin (Figure 7b), which is similar to the downstream increase of incision in the Daxia River (Zhang et al., 2017a), a tributary of the UYR. Modeled age-elevation relationships show that only one synchronous acceleration occurred in the block-block growth model (Figure 8b), which differs from the observed various acceleration times of deformation (Figure 2). Examples include the East Kunlun around 8-5 Ma (Duvall et al., 2013), the Dulan Chaka Highland around 17-12 Ma (Duvall et al., 2013), the Laji Shan around 23-17 Ma (Lease et al., 2011), the Jishi Shan around 13-5 Ma (Lease et al., 2011), the East Qilian Shan around 15-12 Ma (Wang et al., 2020), and the Liupan Shan around 8-7 Ma (Zheng et al., 2006). In contrast, a northward progressive acceleration occurred in the block-propagation growth model (Figure 8c), more consistent with the initially significant activity ages which became younger to the northeast in the NETP (Figure 1c). Moreover, the significant increasing uplift rate occurred after ~5 Ma near the plateau margin (~720 km) (Figure 8c), consistent with previous studies (Zhang et al., 2023). Thus, based on the comparisons of river profiles, swath profiles, erosion rates, and the trend of significant acceleration times (e.g., initially significant activity ages and thermochronometric age-elevation relationships), the block-propagation growth model fits better with the NETP growth records.

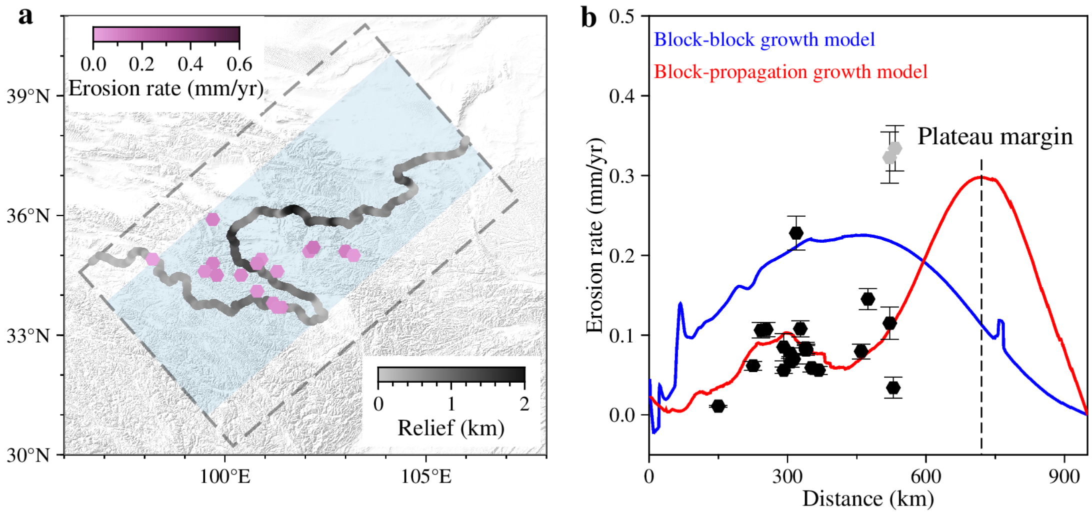

Figure 7. Comparison of the observed and modeled erosion rates. (a) Erosion rates distribution. (b) Comparisons of modeled erosion rates along the river profile. Erosion rates (Table S3) are from references (Harkins et al., 2007; Kirby and Harkins, 2013; Lal et al., 2004; Li et al., 2014b; Zhang et al., 2017a). Grey dots are influenced by transient sediments (Zhang et al., 2017a).

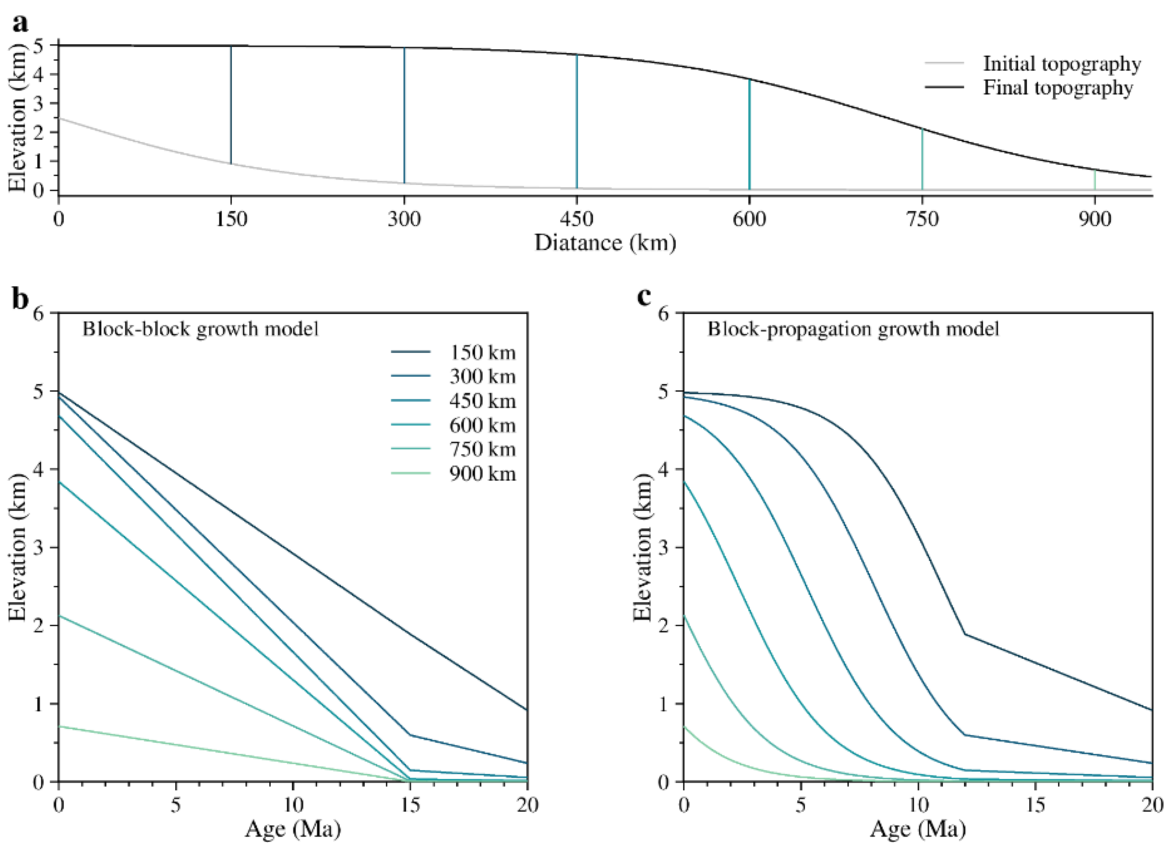

Figure 8. Modeled age-elevation relationships of two growth models. (a) Location of different distances. (b) Block-block growth model. (c) Block-propagation growth model.

4.2 Growth history of the Northeastern Tibetan Plateau

Based on our forward analyses, the block-propagation growth model matches better the NETP growth records. The major range of block uplift only occurred in the south of the modeled area before ~12 Ma (middle Miocene), with broad low elevations in most of the modeled area (Figure 9). Then, a broad propagation uplift occurred in the modeled area from ~12 Ma to the present, forming the modern plateau margin (Figure 9). High elevations (~5 km) expand northward during the plateau growth (Figure 9g).

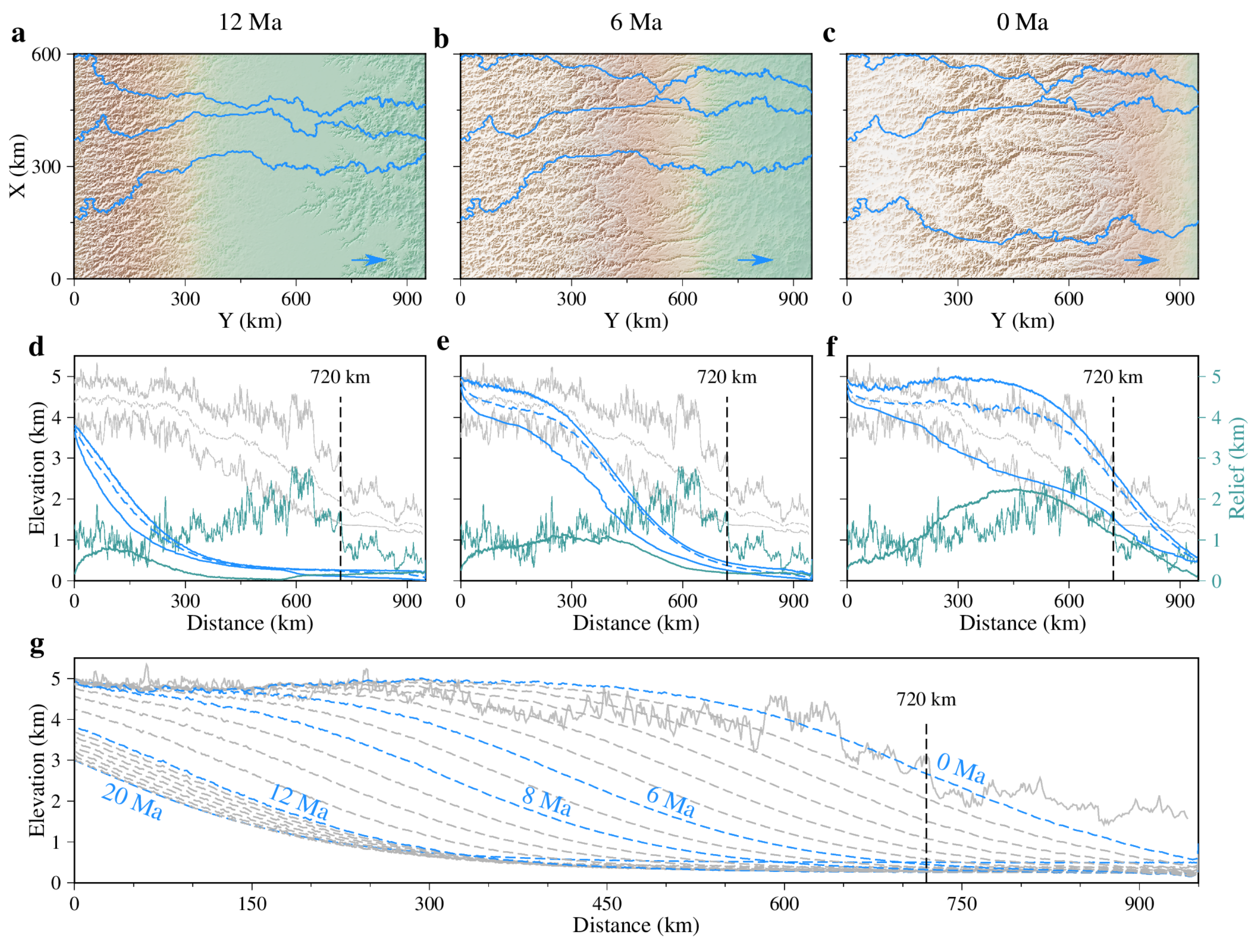

Figure 9. Typical modeled scenarios of the block-propagation growth model. Top panels are modeled landscapes and trunks (blue) at (a) 12 Ma, (b) 6 Ma, and (c) 0 Ma. Blue arrows mark river directions. Middle panels are observed (grey) and modeled (blue) swath profiles and relief (green) at (d) 12 Ma, (e) 6Ma, and (f) 0Ma. (g) The bottom panel shows the maximum elevations along modeled trunks during uplifting. Dashed lines are modeled maximum elevations from 20 Ma to 0 Ma. A grey continuous line is the observed maximum elevation at 0 Ma. The black dashed line at 720 km in (d), (e), (f), and (g) indicates the plateau margin.

Our modeled data are consistent with various observed data, including crustal deformations (Fan et al., 2019; Royden et al., 2008; Yan et al., 2006; Yu et al., 2023) and sedimentary records (Chang et al., 2015; Li et al., 2011). For example, most initial faulting ages in the NETP were after ~20 Ma, with a northward younging trend (Figure 1b, c). The initial propagation uplift time (~12 Ma) is consistent with the widespread middle-Miocene crustal deformation in the NETP (Yu et al., 2023), the formation time (Miocene) of basin-bounding faults in the NETP and the eastern segment of the NETP (Fan et al., 2019). The propagation uplift time of ~12 Ma is also consistent with most of the shortening after ~15 to 20 Ma in the NETP (Royden et al., 2008), and a clockwise rotation during 11-17 Ma in the Guide Basin (Figure 1b) (Yan et al., 2006) based on the magnetostratigraphy. The initial propagation uplift time is also close to the accumulation rate abruptly increased near ~15 Ma in the Qaidam Basin (Figure 1b) based on a stratigraphic study (Chang et al., 2015), and the progressive surface uplift since 15 Ma in the NETP based on the Nd isotopic ratio of Asian dust (Li et al., 2011).

We show the major block uplift and higher elevations occurring in the south of the NETP before ~12 Ma, with broad low elevations to the north, consistent with the observed higher elevations in the south (Polissar et al., 2009; Sun et al., 2015) and low elevations in the north of the East Kunlun fault (Hui et al., 2018). The Hoh-Xil Basin (upper part of the UYR, Figure 1b) reached 1395-2931 m before 17 Ma based on the leaf fossils from an early Miocene barberry (*Berberis*) (Sun et al., 2015), or had uplifted at least 1700-2600 m before the middle Miocene based on δD ratio of surface waters from freshwater limestones (Polissar et al., 2009). In contrast, the Zeku Basin (lower part of the UYR, Figure 1b) had 1200-1400 m elevations during the early to middle Miocene based on palynological data (Hui et al., 2018). Our results are also consistent with the observations of the south of the East Kunlun Fault (Hoh Xil Basin) reached 2-3 km before the Miocene and the modern high elevation of ~4.6 km after ~17 Ma (Staisch et al., 2016). The Hoh Xil Basin had probably reached its current elevation of ~4.6 km by ~12 Ma, considering possible uncertainties (Li and Garzione, 2023). The north of the East Kunlun Fault reached the modern high elevations after ~11 Ma (Miao et al., 2022), based on the pollen records of montane conifers. The surface uplift is not synchronous but is progressive to the north, consistent with our modeling (Figure 9g).

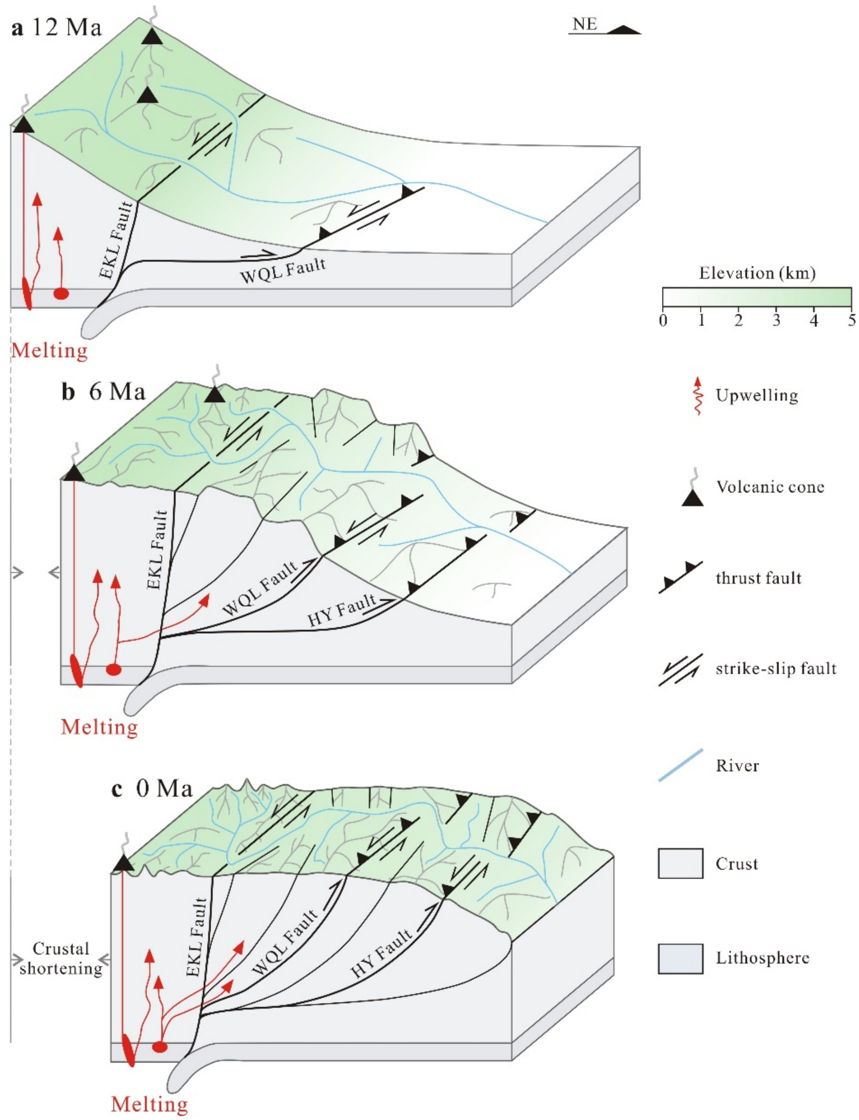

348

349 **Figure 10**. Schematic models illustrate different growth mechanisms on both sides of the East Kunlun
350 Fault. (a) The scenario occurred after block growth (12 Ma) with higher elevations in the south of the East
351 Kunlun Fault than in the north. (b) Propagation growth at 6 Ma. (c) Schematic present-day topography (0
352 Ma). The hypothetical elevations in the diagrams are based on the uplift process in Figure 9g. Initial
353 significant activity ages are based on the data in Figure 1b. EKL Fault: East Kunlun Fault; WQL Fault:
354 West Qinling Fault; HY Fault: Haiyuan Fault. Deep structures are modified from Tapponnier et al. (2001).
355 Primary faults in the NETP are modified from references (Tapponnier et al., 2001; Yuan et al., 2013).

356

357 Different uplift processes in the south and north of the East Kunlun Fault may be related to
358 different uplift mechanisms (Chen et al., 2017; Lease et al., 2012; Staisch et al., 2016; Tapponnier
359 et al., 1990) (Figure 10). The East Kunlun Fault is an important rheological boundary (Karplus et

al., 2011; Le Pape et al., 2012), based on a magnetotelluric profile crossing the Northern Tibetan Plateau (Unsworth et al., 2004). Because of different growth processes in the south and north of the East Kunlun fault, a Paleogene basin was partitioned into the Hoh Xil and Qaidam subbasins by the East Kunlun fault before the middle Miocene (Chen et al., 2017; Yin et al., 2008). In the south of the East Kunlun Fault, the upper crustal shortening within the Hoh Xil Basin ceased between 33.5 and 27.3 Ma (Staisch et al., 2016), and the crust thickening driven by mantle removal related to partial melting or mantle melting (Chen et al., 2017; Staisch et al., 2016) played an important role in the plateau growth since the Miocene (Figure 10a). The surface has been raised ~2 km by mantle melting since the early Miocene (25-20 Ma) (Chen et al., 2017). The magmatic activities widely occurred in the south of the East Kunlun Fault, related to opposing north-directed and south-directed continental subduction after 25 Ma (Guo and Wilson, 2019). In contrast, magmatic activities were rare in the north of the East Kunlun Fault (Yin and Harrison, 2000).

In the north of the East Kunlun Fault, some researchers suggest that the partial melt penetration probably characterizes the plateau growth (Karplus et al., 2011; Medvedev et al., 2006), but crust thickening driven by shortening played a critical role in forming the NETP through fault thrusting and folding (Hu et al., 2015; Lease et al., 2012; Tapponnier et al., 1990) (Figure 10b, c). A transition of the tectonic regime, from extrusion to the distributed shortening in the Northern Tibetan Plateau, was initiated at ~15 Ma (Lu et al., 2016). The distributed crustal shortening was one of the dominant processes in the Northern Tibetan Plateau construction (Zuza et al., 2016). For example, the Jishi Shan, between the Kunlun and Haiyuan left-lateral faults, experienced accelerated exhumation due to thrust-induced rock uplift and erosion at ~13 Ma based on thermochronological data (Lease et al., 2011). More than half of net Cenozoic crustal shortening and thickening in this area has occurred since ~13 Ma, based on cross-section reconstructions (Lease et al., 2012). A reconstruction of crustal thickness around the Jishi Shan shows the crust thickening from the middle Miocene thickness of 50 ± 4 km to the modern thickness of 56 ± 4 km (Lease et al., 2012). In addition, most of the present elevations were reached since the middle Miocene in the NETP (Hui et al., 2018; Zhuang et al., 2014). In the Zeku basin (Figure 1b), the present 60-70% elevations were mainly uplifted since the early-middle Miocene, based on palynological data in the Caergen section (Hui et al., 2018). The Qaidam Basin, near the UYR, whose present elevations of 70% were uplifted during 15-10.4 Ma, based on Leaf wax stable isotopes in the Huaitoutala section (Zhuang et al., 2014).

In summary, consistent with the above studies, our modeled results suggest that most present-day high elevations (~5 km) have been reached since the middle Miocene in the north of the East Kunlun Fault, and then the high elevations expanded northward. The plateau uplift is mostly attributed to the crustal thickening, and the gradual propagation was related to the crustal shortening through fault thrusting and folding.

4.3 Headward erosion cannot form the observed upstream Yellow River profile

The NETP growth primarily controls the UYR formation. However, the UYR formation time is debated, varying from >11.63 Ma to >0.03 Ma based on the initial incision timing (~1.8-0.03 Ma) of the upmost terraces (Craddock et al., 2010), the dating of basin sediments (~1.7 Ma) (Li et al., 2014a), the similar provenance signals in the Linxia and Lanzhou Basins (Figure 1b) (~3.6 Ma) (Nie et al., 2015), the isolation time (1.2-0.5 Ma) of the Qinghai Lake (Figure 1b) (Zhang et al., 2014), the divergence time (~0.19 Ma) of two species (Liang et al., 2018), the sediment in the Hetao Basin (Figure 1b) (~1.68 Ma) (Li et al., 2023), the termination time (~4.8 Ma) of fluviolacustrine-dominated red beds in the Xining Basin (Figure 1b) (Zhang et al., 2017b), and the initial sedimentation (>11.63 Ma) of Eocene-Miocene red bed in the Lanzhou zone (Lin et al., 2001). Among these formation timings, some studies suggest that the UYR formed over the last few million years (~2.58-0.03 Ma) since the UYR excavated basin sediments systematically upstream through headward erosion (Craddock et al., 2010; Jia et al., 2017; Su et al., 2023), with a rate of ~350 km Myr^{-1} (Craddock et al., 2010). The block-block growth model experiences headward erosion in our study because the modeled area only grows upward without horizontal motion. χ-elevation plots from all block-block growth models, compared to the UYR river profile, show that no appropriate modeled results can match the observed UYR river profile (Figure 5a). In contrast, a few block-propagation growth model results match the observed UYR river profile (Figure 5b). The high erosion rates mainly propagated downstream during the outward propagation of the NETP growth, similar to the erosion pattern that occurred in the eastern Tibetan Plateau (Yuan et al., 2023).

Next, we test whether the pure headward erosion (and retreat process) can form the UYR river profile using the landscape evolution model with various erodibilities and model run durations. To match the elevation of the observed base level of the NETP margin, we set the modeled boundary at 820 km (Figure 11). The initial topography is set to the maximum topography

(Figure 3) based on equation 2, with the amplitude white noise (<100 m). The fluvial erodibilities are set to (2, 4, 6, 8, 10, and 12) × $10^{-6}\ \mathrm{m}^{0.16}/\mathrm{yr}$, and the model run durations are set to (2, 4, 6, 8, and 10) Myr for modeling the retreat process (Figure 11). Modeled river profiles (Figure 5a, 11) indicate that the pure headward erosion suggested by previous studies (Craddock et al., 2010; Harkins et al., 2007; Jia et al., 2017; Su et al., 2023) hardly formed the UYR river profile over a few million years.

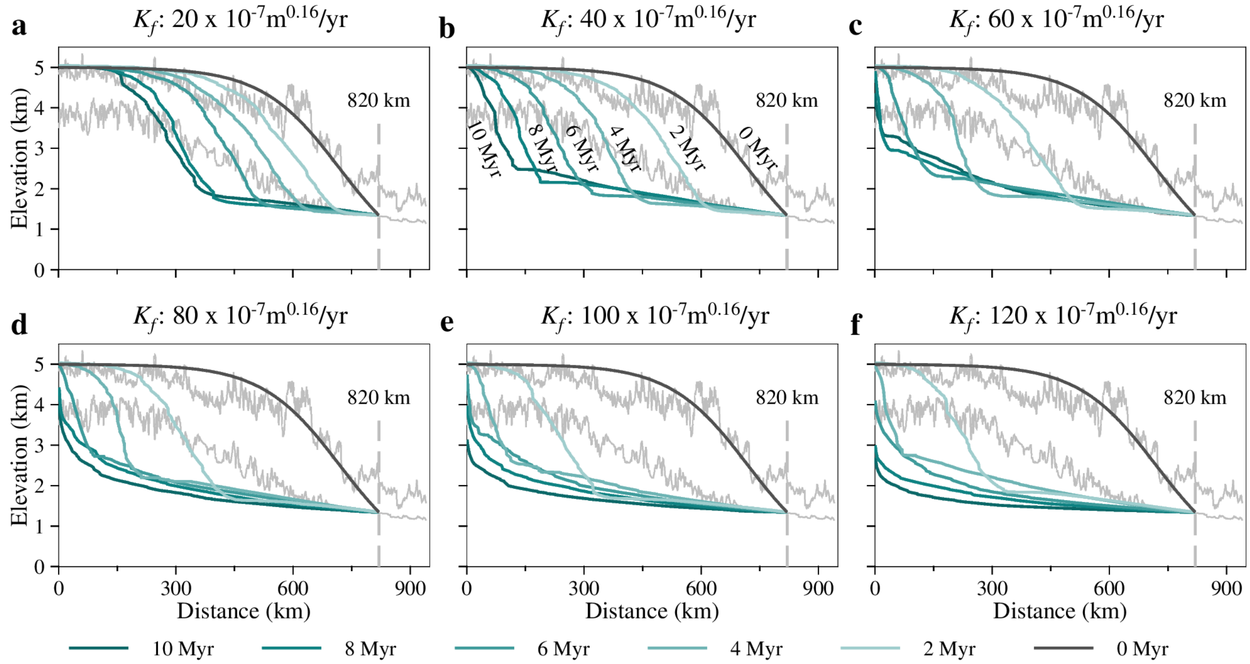

Figure 11. The observed maximum and minimum elevations (grey) and modeled (thick line) river profiles from different sets of erodibilities and model durations in each headward erosion and retreat process. We set the modeled boundary at 820 km to match the elevation of the observed and modeled base levels.

Most young formation times of the UYR are suggested based on the abandonment time (i.e., initial incision time) of the upmost terraces (Craddock et al., 2010; Jia et al., 2017; Su et al., 2023; Zhang et al., 2014). However, the divergent young ages for the inception of the Yellow River can be related to periodic climate fluctuations, and may correspond only to different re-integration events due to deglaciation or desiccation (Zhao et al., 2023). The re-integration events due to desiccation have been reported in the Yellow River middle reach (Zhao et al., 2023). In addition, the formation, abandonment, and preservation of fluvial terraces are often related to changes in tectonics and/or climate (Reusser et al., 2004; Wang et al., 2015). Modifying any external factors can rework the previously formed fluvial terraces and erase the previous geomorphic and stratigraphic records (Pan et al., 2009), and the hoarier records of fluvial terraces may be modified more easily.

On the other hand, the thermochronometric age-elevation relationships (Figure 2), responding to a long-term history of exhumation, suggest that the NETP experienced a long-term exhumation history, rather than a short-term erosion history over a few million years. Moreover, there were connections between the upstream mountain and the downstream basin before 20 Ma in the NETP (Liu, 2015). Sediments from the Anyemaqen Shan (Figure 1b) were deposited in the Guide Basin during 53-33 Ma and in the Lanzhou Basin around 43 Ma (Liu, 2015). In summary, we suggest that the UYR may have existed long accompanying the long-term NETP growth, based on our modeled results, previous studies, and thermochronometric data.

5 Conclusions

Using a numerical landscape evolution model, we quantitatively study the ~20 Ma growth history of the NETP correlated with the formation of the UYR. The block-propagation growth model, comprised of an early block uplift (~20-12 Ma) and a late propagation uplift (~12-0 Ma), is consistent with the records of the NETP based on the comparisons of the observed and modeled river profiles, swath profiles, erosion rates, the trend of acceleration times of deformation (e.g., initially significant activity ages and thermochronometric age-elevation relationships), and paleo-elevation datasets. We show that a block growth primarily occurred in the south of the NETP before ~12 Ma (middle Miocene), and a propagation growth broadly occurred in the NETP after ~12 Ma with high elevations (~5 km) expanding northward. We further suggest that pure headward erosion unlikely formed the river profile of the UYR over a few million years. Our results show that the long-term fluvial erosion in the NETP features mainly a downstream migration of high erosion rates, which is significantly different from the headward erosion of small mountain rivers. This erosion pattern in the NETP, similar to that occurred in the Eastern Tibetan Plateau (Yuan et al., 2023), may represent a common erosion pattern of outward-growing plateaus in tectonically active regions on Earth.

Acknowledgments

We thank XXX for reviewing. X.P.Y. acknowledges funding from NSFC (Grant 42272261).

Data Availability Statement

The codes used for the simulations are available in Yuan et al. (2019) and https://doi.org/10.5281/zenodo.3833983 website (Bovy & Braun, 2020). Figures were made using ParaView, CorelDRAW, and Generic Mapping Tools.

References

Allen, P. A. (2008), From landscapes into geological history: *Nature*, 451 (7176), 274-276. Doi: 10.1038/nature06586.

An, Z., Kutzbach, J. E., Prell, W. L., & Porter, S. C. (2001), Evolution of Asian monsoons and phased uplift of the Himalaya–Tibetan plateau since Late Miocene times: *Nature*, 411 (6833), 62-66. Doi: 10.1038/35075035.

Bovy, B., & Braun, J. (2020). Fastscape-lem/fastscapelib-fortran. Zenodo. Doi: 10.5281/zenodo.3833983.

Braun, J., & Willett, S. D. (2013), A very efficient O(n), implicit and parallel method to solve the stream power equation governing fluvial incision and landscape evolution: *Geomorphology*, 180-181 (170-179. Doi: 10.1016/j.geomorph.2012.10.008.

Chang, H., Li, L., Qiang, X., Garzione, C. N., Pullen, A., & An, Z. (2015), Magnetostratigraphy of Cenozoic deposits in the western Qaidam Basin and its implication for the surface uplift of the northeastern margin of the Tibetan Plateau: *Earth and Planetary Science Letters*, 430 (271-283. Doi: 10.1016/j.epsl.2015.08.029.

Chen, J.-L., Yin, A., Xu, J.-F., Dong, Y.-H., & Kang, Z.-Q. (2017), Late Cenozoic magmatic inflation, crustal thickening, and >2 km of surface uplift in central Tibet: *Geology*, 46 (1), 19-22. Doi: 10.1130/g39699.1.

Clark, M. K., Farley, K. A., Zheng, D., Wang, Z., & Duvall, A. R. (2010), Early Cenozoic faulting of the northern Tibetan Plateau margin from apatite (U–Th)/He ages: *Earth and Planetary Science Letters*, 296 (1-2), 78-88. Doi: 10.1016/j.epsl.2010.04.051.

Clark, M. K., & Royden, L. H. (2000), Topographic ooze: Building the eastern margin of Tibet by lower crustal flow: *Geology*, 28 (8), 703-706. Doi: 10.1130/0091-7613(2000)28<703:Tobtem>2.0.Co;2.

Craddock, W. H., Kirby, E., Harkins, N. W., Zhang, H., Shi, X., & Liu, J. (2010), Rapid fluvial incision along the Yellow River during headward basin integration: *Nature Geoscience*, 3 (3), 209-213. Doi: 10.1038/ngeo777.

Dai, S., Fang, X., Dupont-Nivet, G., Song, C., Gao, J., Krijgsman, W., Langereis, C., & Zhang, W. (2006), Magnetostratigraphy of Cenozoic sediments from the Xining Basin: Tectonic implications for the northeastern Tibetan Plateau: *Journal of Geophysical Research: Solid Earth*, 111 (B11). Doi: 10.1029/2005JB004187.

Dayem, K. E., Molnar, P., Clark, M. K., & Houseman, G. A. (2009), Far-field lithospheric deformation in Tibet during continental collision: *Tectonics*, 28 (6). Doi: 10.1029/2008TC002344.

Ding, L., Kapp, P., Cai, F., Garzione, C. N., Xiong, Z., Wang, H., & Wang, C. (2022), Timing and mechanisms of Tibetan Plateau uplift: *Nature Reviews Earth & Environment*, 3 (10), 652-667. Doi: 10.1038/s43017-022-00318-4.

Dupont-Nivet, G., Horton, B. K., Butler, R. F., Wang, J., Zhou, J., & Waanders, G. L. (2004), Paleogene clockwise tectonic rotation of the Xining-Lanzhou region, northeastern Tibetan Plateau: *Journal of Geophysical Research: Solid Earth*, 109 (B4). Doi: 10.1029/2003JB002620.

Duvall, A. R., Clark, M. K., Kirby, E., Farley, K. A., Craddock, W. H., Li, C., & Yuan, D.-Y. (2013), Low-temperature thermochronometry along the Kunlun and Haiyuan Faults, NE Tibetan Plateau: Evidence for kinematic change during late-stage orogenesis: *Tectonics*, 32 (5), 1190-1211. Doi: 10.1002/tect.20072.

England, P., & Houseman, G. (1989), Extension during continental convergence, with application to the Tibetan Plateau: *Journal of Geophysical Research*, 94 (B12). Doi: 10.1029/JB094iB12p17561.

Fan, L.-G., Meng, Q.-R., Wu, G.-L., Wei, H.-H., Du, Z.-M., & Wang, E. (2019), Paleogene crustal extension in the eastern segment of the NE Tibetan plateau: *Earth and Planetary Science Letters*, 514 (62-74. Doi: 10.1016/j.epsl.2019.02.036.

Fang, X., Dupont-Nivet, G., Wang, C., Song, C., Meng, Q., Zhang, W., Nie, J., Zhang, T., Mao, Z., & Chen, Y. (2020), Revised chronology of central Tibet uplift (Lunpola Basin): *Science Advances*, 6 (50), eaba7298. Doi: 10.1126/sciadv.aba7298.

Fox, M., Bodin, T., & Shuster, D. L. (2015), Abrupt changes in the rate of Andean Plateau uplift from reversible jump Markov Chain Monte Carlo inversion of river profiles: *Geomorphology*, 238 (1-14. Doi: 10.1016/j.geomorph.2015.02.022.

Goren, L., Fox, M., & Willett, S. D. (2014), Tectonics from fluvial topography using formal linear inversion: Theory and applications to the Inyo Mountains, California: *Journal of Geophysical Research: Earth Surface*, 119 (8), 1651-1681. Doi: 10.1002/2014jf003079.

Guerit, L., Yuan, X.-P., Carretier, S., Bonnet, S., Rohais, S., Braun, J., & Rouby, D. (2019), Fluvial landscape evolution controlled by the sediment deposition coefficient: Estimation from experimental and natural landscapes: *Geology*, 47 (9), 853-856. Doi: 10.1130/g46356.1.

Guo, Z., & Wilson, M. (2019), Late Oligocene–early Miocene transformation of postcollisional magmatism in Tibet: *Geology*, 47 (8), 776-780. Doi: 10.1130/g46147.1.

Guo, Z., Wilson, M., Dingwell, D. B., & Liu, J. (2021), India-Asia collision as a driver of atmospheric CO(2) in the Cenozoic: *Nature Communications*, 12 (1), 3891. Doi: 10.1038/s41467-021-23772-y.

Harkins, N., Kirby, E., Heimsath, A., Robinson, R., & Reiser, U. (2007), Transient fluvial incision in the headwaters of the Yellow River, northeastern Tibet, China: *Journal of Geophysical Research: Earth Surface*, 112 (F3). Doi: 10.1029/2006JF000570.

Hu, X., Pan, B., Kirby, E., Gao, H., Hu, Z., Cao, B., Geng, H., Li, Q., & Zhang, G. (2015), Rates and kinematics of active shortening along the eastern Qilian Shan, China, inferred from deformed fluvial terraces: *Tectonics*, 34 (12), 2478-2493. Doi: 10.1002/2015tc003978.

Hui, Z., Li, X., Ma, Z., Xiao, L., Zhang, J., & Chang, J. (2018), Miocene pollen assemblages from the Zeku Basin, northeastern Tibetan Plateau, and their palaeoecological and palaeoaltimetric implications: *Palaeogeography, Palaeoclimatology, Palaeoecology*, 511 (419-432. Doi: 10.1016/j.palaeo.2018.09.009.

Jammes, S., & Huismans, R. S. (2012), Structural styles of mountain building: Controls of lithospheric rheologic stratification and extensional inheritance: *Journal of Geophysical Research: Solid Earth*, 117 (B10). Doi: 10.1029/2012JB009376.

Jia, L., Hu, D., Wu, H., Zhao, X., Chang, P., You, B., Zhang, M., Wang, C., Ye, M., Wu, Z., & Liang, X. (2017), Yellow

River terrace sequences of the Gonghe–Guide section in the northeastern Qinghai–Tibet: Implications for plateau uplift: *Geomorphology*, 295 (323-336. Doi: 10.1016/j.geomorph.2017.06.007.

Karplus, M. S., Zhao, W., Klemperer, S. L., Wu, Z., Mechie, J., Shi, D., Brown, L. D., & Chen, C. (2011), Injection of Tibetan crust beneath the south Qaidam Basin: Evidence from INDEPTH IV wide-angle seismic data: *Journal of Geophysical Research*, 116 (B7). Doi: 10.1029/2010jb007911.

Kirby, E., & Harkins, N. (2013), Distributed deformation around the eastern tip of the Kunlun fault: *International Journal of Earth Sciences*, 102 (7), 1759-1772. Doi: 10.1007/s00531-013-0872-x.

Kirby, E., Whipple, K. X., Tang, W., & Chen, Z. (2003), Distribution of active rock uplift along the eastern margin of the Tibetan Plateau: Inferences from bedrock channel longitudinal profiles: *Journal of Geophysical Research: Solid Earth*, 108 (B4). Doi: 10.1029/2001jb000861.

Klaus, S., Morley, R. J., Plath, M., Zhang, Y.-P., & Li, J.-T. (2016), Biotic interchange between the Indian subcontinent and mainland Asia through time: *Nature Communications*, 7 (1), 12132. Doi: 10.1038/ncomms12132.

Kutzbach, J. E., Prell, W. L., & Ruddiman, W. F. (1993), Sensitivity of Eurasian Climate to Surface Uplift of the Tibetan Plateau: *The Journal of Geology*, 101 (2), 177-190. Doi: 10.1086/648215.

Lal, D., Harris, N. B. W., Sharma, K. K., Gu, Z., Ding, L., Liu, T., Dong, W., Caffee, M. W., & Jull, A. J. T. (2004), Erosion history of the Tibetan Plateau since the last interglacial: constraints from the first studies of cosmogenic 10Be from Tibetan bedrock: *Earth and Planetary Science Letters*, 217 (1), 33-42. Doi: 10.1016/S0012-821X(03)00600-9.

Law, R., & Allen, M. B. (2020), Diachronous Tibetan Plateau landscape evolution derived from lava field geomorphology: *Geology*, 48 (3), 263-267. Doi: 10.1130/g47196.1.

Le Pape, F., Jones, A. G., Vozar, J., & Wenbo, W. (2012), Penetration of crustal melt beyond the Kunlun Fault into northern Tibet: *Nature Geoscience*, 5 (5), 330-335. Doi: 10.1038/ngeo1449.

Lease, R. O., Burbank, D. W., Clark, M. K., Farley, K. A., Zheng, D., & Zhang, H. (2011), Middle Miocene reorganization of deformation along the northeastern Tibetan Plateau: *Geology*, 39 (4), 359-362. Doi: 10.1130/g31356.1.

Lease, R. O., Burbank, D. W., Zhang, H., Liu, J., & Yuan, D. (2012), Cenozoic shortening budget for the northeastern edge of the Tibetan Plateau: Is lower crustal flow necessary?: *Tectonics*, 31 (3). Doi: 10.1029/2011TC003066.

Li, B., Chen, X., Zuza, A. V., Hu, D., Ding, W., Huang, P., & Xu, S. (2019), Cenozoic cooling history of the North Qilian Shan, northern Tibetan Plateau, and the initiation of the Haiyuan fault: Constraints from apatite- and zircon-fission track thermochronology: *Tectonophysics*, 751 (109-124. Doi: 10.1016/j.tecto.2018.12.005.

Li, B., Feng, Q., Wang, X., Li, Z., Wang, F., Zhao, C., Yu, T., & Chen, W. (2023), Formation of the upper reaches of the Yellow River: Provenance evidence from the strata of the Yellow River sedimentary basin: *Global and Planetary Change*, 229 (104224. Doi: 10.1016/j.gloplacha.2023.104224.

Li, B., Wang, Y., Zuza, A. V., Chen, X., Shao, Z., Wang, Z.-Z., Sun, Y., & Wu, C. (2022), Cenozoic deformation in the eastern domain of the North Qaidam thrust belt, northern Tibetan Plateau: *GSA Bulletin*, 135 (1-2), 331-350. Doi: 10.1130/b36215.1.

Li, G., Pettke, T., & Chen, J. (2011), Increasing Nd isotopic ratio of Asian dust indicates progressive uplift of the north

Tibetan Plateau since the middle Miocene: *Geology*, 39 (3), 199-202. Doi: 10.1130/g31734.1.

Li, J., Fang, X., Song, C., Pan, B., Ma, Y., & Yan, M. (2014a), Late Miocene–Quaternary rapid stepwise uplift of the NE Tibetan Plateau and its effects on climatic and environmental changes: *Quaternary Research*, 81 (3), 400-423. Doi: 10.1016/j.yqres.2014.01.002.

Li, L., & Garzione, C. N. (2023), Upward and outward growth of north-central Tibet: Mechanisms that build high-elevation, low-relief plateaus: *Science Advances*, 9 (27), eadh3058. Doi: 10.1126/sciadv.adh3058.

Li, Y., Li, D., Liu, G., Harbor, J., Caffee, M., & Stroeven, A. P. (2014b), Patterns of landscape evolution on the central and northern Tibetan Plateau investigated using in-situ produced 10Be concentrations from river sediments: *Earth and Planetary Science Letters*, 398 (77-89. Doi: 10.1016/j.epsl.2014.04.045.

Liang, H. Y., Feng, Z. P., Pei, B., Li, Y., & Yang, X. T. (2018), Demographic expansion of two Tamarix species along the Yellow River caused by geological events and climate change in the Pleistocene: *Scientific Reports*, 8 (1), 60. Doi: 10.1038/s41598-017-19034-x.

Lin, A., Yang, Z., Sun, Z., & Yang, T. (2001), How and when did the Yellow River develop its square bend?: *Geology*, 9 (10), 951–954. Doi: 10.1130/0091-7613(2001)029<0951:HAWDTY>2.0.CO;2.

Liu, P. (2015), Spatio-temporal evolution of Northeastern Tibetan Plateau: integrated provenance study of the Guide, Lanzhou and Wushan-Tianshui basins [Doctor: Lanzhou University.

Lu, H., Fu, B., Shi, P., Ma, Y., & Li, H. (2016), Constraints on the uplift mechanism of northern Tibet: *Earth and Planetary Science Letters*, 453 (108-118. Doi: 10.1016/j.epsl.2016.08.010.

Märki, L., Lupker, M., France-Lanord, C., Lavé, J., Gallen, S., Gajurel, A. P., Haghipour, N., Leuenberger-West, F., & Eglinton, T. (2021), An unshakable carbon budget for the Himalaya: *Nature Geoscience*, 14 (10), 745-750. Doi: 10.1038/s41561-021-00815-z.

Medvedev, S., Beaumont, C., Law, R. D., Searle, M. P., & Godin, L. (2006), Growth of continental plateaus by channel injection: models designed to address constraints and thermomechanical consistency, Channel Flow, Ductile Extrusion and Exhumation in Continental Collision Zones, Volume 268, Geological Society of London, p. 147-164.

Miao, Y., Fang, X., Sun, J., Xiao, W., Yang, Y., Wang, X., Farnsworth, A., Huang, K., Ren, Y., Wu, F., Qiao, Q., Zhang, W., Meng, Q., Yan, X., Zheng, Z., Song, C., & Utescher, T. (2022), A new biologic paleoaltimetry indicating Late Miocene rapid uplift of northern Tibet Plateau: *Science*, 378 (6624), 1074-1079. Doi: doi:10.1126/science.abo2475.

Nie, J., Stevens, T., Rittner, M., Stockli, D., Garzanti, E., Limonta, M., Bird, A., Ando, S., Vermeesch, P., Saylor, J., Lu, H., Breecker, D., Hu, X., Liu, S., Resentini, A., Vezzoli, G., Peng, W., Carter, A., Ji, S., & Pan, B. (2015), Loess Plateau storage of Northeastern Tibetan Plateau-derived Yellow River sediment: *Nat Commun*, 6 (8511. Doi: 10.1038/ncomms9511.

Pan, B., Su, H., Hu, Z., Hu, X., Gao, H., Li, J., & Kirby, E. (2009), Evaluating the role of climate and tectonics during non-steady incision of the Yellow River: evidence from a 1.24Ma terrace record near Lanzhou, China: *Quaternary Science Reviews*, 28 (27), 3281-3290. Doi: 10.1016/j.quascirev.2009.09.003.

Perron, J. T., & Royden, L. (2013), An integral approach to bedrock river profile analysis: *Earth Surface Processes* *and Landforms*, 38 (6), 570-576. Doi: 10.1002/esp.3302.

Polissar, P. J., Freeman, K. H., Rowley, D. B., McInerney, F. A., & Currie, B. S. (2009), Paleoaltimetry of the Tibetan Plateau from D/H ratios of lipid biomarkers: *Earth and Planetary Science Letters*, 287 (1-2), 64-76. Doi: 10.1016/j.epsl.2009.07.037.

Pritchard, D., Roberts, G. G., White, N. J., & Richardson, C. N. (2009), Uplift histories from river profiles: *Geophysical Research Letters*, 36 (24). Doi: 10.1029/2009gl040928.

Racano, S., Schildgen, T. F., Cosentino, D., & Miller, S. R. (2021), Temporal and Spatial Variations in Rock Uplift From River-Profile Inversions at the Central Anatolian Plateau Southern Margin: *Journal of Geophysical Research: Earth Surface*, 126 (8), e2020JF006027. Doi: 10.1029/2020JF006027.

Reusser, L. J., Bierman, P. R., Pavich, M. J., Zen, E.-a., Larsen, J., & Finkel, R. (2004), Rapid Late Pleistocene Incision of Atlantic Passive-Margin River Gorges: *Science*, 305 (5683), 499-502. Doi: doi:10.1126/science.1097780.

Roberts, G. G., White, N. J., Martin-Brandis, G. L., & Crosby, A. G. (2012), An uplift history of the Colorado Plateau and its surroundings from inverse modeling of longitudinal river profiles: *Tectonics*, 31 (4), n/a-n/a. Doi: 10.1029/2012tc003107.

Rowley, D. B., & Currie, B. S. (2006), Palaeo-altimetry of the late Eocene to Miocene Lunpola basin, central Tibet: *Nature*, 439 (7077), 677-681. Doi: 10.1038/nature04506.

Royden, L. H., Burchfiel, B. C., King, R. W., Wang, E., Chen, Z., Shen, F., & Liu, Y. (1997), Surface Deformation and Lower Crustal Flow in Eastern Tibet: *Science*, 276 (5313), 788-790. Doi: 10.1126/science.276.5313.788.

Royden, L. H., Burchfiel, B. C., & van der Hilst, R. D. (2008), The geological evolution of the Tibetan Plateau: *Science*, 321 (5892), 1054-1058. Doi: 10.1126/science.1155371.

Shen, X., Braun, J., & Yuan, X. (2022), Southeastern margin of the Tibetan Plateau stopped expanding in the late Miocene: *Earth and Planetary Science Letters*, 583 (117446. Doi: 10.1016/j.epsl.2022.117446.

Staisch, L. M., Niemi, N. A., Clark, M. K., & Chang, H. (2016), Eocene to late Oligocene history of crustal shortening within the Hoh Xil Basin and implications for the uplift history of the northern Tibetan Plateau: *Tectonics*, 35 (4), 862-895. Doi: 10.1002/2015tc003972.

Su, Q., Wang, X., Yuan, D., Xie, H., Li, H., & Huang, X. (2023), Fluvial entrenchment of the Gonghe Basin and integration of the upper Yellow River - Evidence from the cosmogenically dated geomorphic surfaces: *Geomorphology*, 429 (Doi: 10.1016/j.geomorph.2023.108654.

Su, T., Farnsworth, A., Spicer, R. A., Huang, J., Wu, F.-X., Liu, J., Li, S.-F., Xing, Y.-W., Huang, Y.-J., Deng, W.-Y.-D., Tang, H., Xu, C.-L., Zhao, F., Srivastava, G., Valdes, P. J., Deng, T., & Zhou, Z.-K. (2019), No high Tibetan Plateau until the Neogene: *Science Advances*, 5 (3), eaav2189. Doi: 10.1126/sciadv.aav2189.

Sun, B., Wang, Y. F., Li, C. S., Yang, J., Li, J. F., Li, Y. L., Deng, T., Wang, S. Q., Zhao, M., Spicer, R. A., Ferguson, D. K., & Mehrotra, R. C. (2015), Early Miocene elevation in northern Tibet estimated by palaeobotanical evidence: *Scientific Reports*, 5 (10379. Doi: 10.1038/srep10379.

Tapponnier, P., Meyer, B., Avouac, J. P., Peltzer, G., Gaudemer, Y., Guo, S., Xiang, H., Yin, K., Chen, Z., Cai, S., & Dai, H. (1990), Active thrusting and folding in the Qilian Shan, and decoupling between upper crust and mantle in northeastern Tibet: *Earth and Planetary Science Letters*, 97 (3), 382-403. Doi: 10.1016/0012-821X(90)90053-

Z.

Tapponnier, P., Zhiqin, X., Roger, F., Meyer, B., Arnaud, N., Wittlinger, G., & Jingsui, Y. (2001), Oblique Stepwise Rise and Growth of the Tibet Plateau: *Science*, 294 (5547), 1671-1677. Doi: 10.1126/science.105978.

Unsworth, M., Wei, W., Jones, A., Li, S., Bedrosian, P., Booker, J., Jin, S., Deng, M., & Tan, H. (2004), Crustal and upper mantle structure of northern Tibet imaged with magnetotelluric data: *Journal of Geophysical Research-Solid Earth*, 109 (Doi: 10.1029/2002JB002305.

Wang, C., Dai, J., Zhao, X., Li, Y., Graham, S. A., He, D., Ran, B., & Meng, J. (2014), Outward-growth of the Tibetan Plateau during the Cenozoic: A review: *Tectonophysics*, 621 (1-43. Doi: 10.1016/j.tecto.2014.01.036.

Wang, W., Zhang, P., Garzione, C. N., Liu, C., Zhang, Z., Pang, J., Wang, Y., Zheng, D., Zheng, W., & Zhang, H. (2022), Pulsed rise and growth of the Tibetan Plateau to its northern margin since ca. 30 Ma: *Proc Natl Acad Sci U S A*, 119 (8). Doi: 10.1073/pnas.2120364119.

Wang, W., Zheng, D., Li, C., Wang, Y., Zhang, Z., Pang, J., Wang, Y., Yu, J., Wang, Y., Zheng, W., Zhang, H., & Zhang, P. (2020), Cenozoic Exhumation of the Qilian Shan in the Northeastern Tibetan Plateau: Evidence From Low-Temperature Thermochronology: *Tectonics*, 39 (4). Doi: 10.1029/2019tc005705.

Wang, W., Zheng, W., Zhang, P., Li, Q., Kirby, E., Yuan, D., Zheng, D., Liu, C., Wang, Z., Zhang, H., & Pang, J. (2017), Expansion of the Tibetan Plateau during the Neogene: *Nature Communications*, 8 (15887. Doi: 10.1038/ncomms15887.

Wang, X., Vandenberghe, J., Yi, S., Van Balen, R., & Lu, H. (2015), Climate-dependent fluvial architecture and processes on a suborbital timescale in areas of rapid tectonic uplift: An example from the NE Tibetan Plateau: *Global and Planetary Change*, 133 (318-329. Doi: 10.1016/j.gloplacha.2015.09.009.

Whipple, K. X., & Tucker, G. E. (1999), Dynamics of the stream-power river incision model: Implications for height limits of mountain ranges, landscape response timescales, and research needs: *Journal of Geophysical Research: Solid Earth*, 104 (B8), 17661-17674. Doi: 10.1029/1999jb900120.

Wolf, S. G., Huismans, R. S., Braun, J., & Yuan, X. (2022), Topography of mountain belts controlled by rheology and surface processes: *Nature*, 606 (7914), 516-521. Doi: 10.1038/s41586-022-04700-6.

Yan, M., VanderVoo, R., Fang, X.-m., Parés, J. M., & Rea, D. K. (2006), Paleomagnetic evidence for a mid-Miocene clockwise rotation of about 25° of the Guide Basin area in NE Tibet: *Earth and Planetary Science Letters*, 241 (1-2), 234-247. Doi: 10.1016/j.epsl.2005.10.013.

Yin, A., Dang, Y.-Q., Zhang, M., Chen, X.-H., & McRivette, M. W. (2008), Cenozoic tectonic evolution of the Qaidam basin and its surrounding regions (Part 3): Structural geology, sedimentation, and regional tectonic reconstruction: *GSA Bulletin*, 120 (7-8), 847-876. Doi: 10.1130/b26232.1.

Yin, A., & Harrison, T. M. (2000), Geologic Evolution of the Himalayan-Tibetan Orogen: *Annual Review of Earth and Planetary Sciences*, 28 (1), 211-280. Doi: 10.1146/annurev.earth.28.1.211.

Yu, J., Zheng, D., Wang, W., Pang, J., Li, C., Wang, Y., Hao, Y., Zhang, H., & Zhang, P. (2023), Cenozoic tectonic development in the northeastern Tibetan Plateau: Evidence from thermochronological and sedimentological records: *Global and Planetary Change*, 224 (104098. Doi: 10.1016/j.gloplacha.2023.104098.

Yuan, D. Y., Champagnac, J. D., Ge, W. P., Molnar, P., Zhang, P. Z., Zheng, W. J., Zhang, H. P., & Liu, X. W. (2011), Late Quaternary right-lateral slip rates of faults adjacent to the lake Qinghai, northeastern margin of the Tibetan Plateau: *Geological Society of America Bulletin*, 123 (9-10), 2016-2030. Doi: 10.1130/b30315.1.

Yuan, D. Y., Ge, W. P., Chen, Z. W., Li, C. Y., Wang, Z. C., Zhang, H. P., Zhang, P. Z., Zheng, D. W., Zheng, W. J., Craddock, W. H., Dayem, K. E., Duvall, A. R., Hough, B. G., Lease, R. O., Champagnac, J. D., Burbank, D. W., Clark, M. K., Farley, K. A., Garzione, C. N., Kirby, E., Molnar, P., & Roe, G. H. (2013), The growth of northeastern Tibet and its relevance to large-scale continental geodynamics: A review of recent studies: *Tectonics*, 32 (5), 1358-1370. Doi: 10.1002/tect.20081.

Yuan, X. P., Braun, J., Guerit, L., Rouby, D., & Cordonnier, G. (2019), A New Efficient Method to Solve the Stream Power Law Model Taking Into Account Sediment Deposition: *Journal of Geophysical Research: Earth Surface*, 124 (6), 1346-1365. Doi: 10.1029/2018jf004867.

Yuan, X. P., Huppert, K. L., Braun, J., Shen, X., Liu-Zeng, J., Guerit, L., Wolf, S. G., Zhang, J. F., & Jolivet, M. (2021), Propagating uplift controls on high-elevation, low-relief landscape formation in the southeast Tibetan Plateau: *Geology*, 50 (1), 60-65. Doi: 10.1130/g49022.1.

Yuan, X. P., Jiao, R., Dupont-Nivet, G., & Shen, X. (2022), Southeastern Tibetan Plateau Growth Revealed by Inverse Analysis of Landscape Evolution Model: *Geophysical Research Letters*, 49 (10). Doi: 10.1029/2021gl097623.

Yuan, X. P., Jiao, R., Liu-Zeng, J., Dupont-Nivet, G., Wolf, S. G., & Shen, X. (2023), Downstream propagation of fluvial erosion in Eastern Tibet: *Earth and Planetary Science Letters*, 605 (Doi: 10.1016/j.epsl.2023.118017.

Zhang, H., Kirby, E., Pitlick, J., Anderson, R. S., & Zhang, P. (2017a), Characterizing the transient geomorphic response to base-level fall in the northeastern Tibetan Plateau: *Journal of Geophysical Research: Earth Surface*, 122 (2), 546-572. Doi: 10.1002/2015JF003715.

Zhang, H., Zhang, P., Champagnac, J. D., Molnar, P., Anderson, R. S., Kirby, E., Craddock, W. H., & Liu, S. (2014), Pleistocene drainage reorganization driven by the isostatic response to deep incision into the northeastern Tibetan Plateau: *Geology*, 42 (4), 303-306. Doi: 10.1130/g35115.1.

Zhang, P., Burchfiel, B. C., Molnar, P., Zhang, W., Jiao, D., Deng, Q., Wang, Y., Royden, L., & Song, F. (1991), Amount and style of Late Cenozoic Deformation in the Liupan Shan Area, Ningxia Autonomous Region, China: *Tectonics*, 10 (6), 1111-1129. Doi: 10.1029/90TC02686.

Zhang, W., Zhang, T., Song, C., Erwin, A., Mao, Z., Yahui, F., Yin, L., Qingquan, M., Rongsheng, Y., Dawen, Z., Bingshuai, L., & Jiao, L. (2017b), Termination of fluvial-alluvial sedimentation in the Xining Basin, NE Tibetan Plateau, and its subsequent geomorphic evolution: *Geomorphology*, 297 (86-99. Doi: 10.1016/j.geomorph.2017.09.008.

Zhang, Y., Zhang, H., Ma, Z., Wang, Y., & Zhao, X. (2023), Inversion of Late Miocene uplift history from the transient Daxia River landscape, NE Tibetan Plateau: *Journal of the Geological Society*, 180 (6). Doi: 10.1144/jgs2023-030.

Zhao, Y., Fan, N., Nie, J., Abell, J. T., An, Y., Jin, Z., Wang, C., Zhang, J., Liu, X., & Nie, R. (2023), From Desiccation to Re-Integration of the Yellow River Since the Last Glaciation: *Geophysical Research Letters*, 50 (15), e2023GL103632. Doi: 10.1029/2023GL103632.

Zheng, D., Zhang, P.-Z., Wan, J., Yuan, D., Li, C., Yin, G., Zhang, G., Wang, Z., Min, W., & Chen, J. (2006), Rapid exhumation at ~8 Ma on the Liupan Shan thrust fault from apatite fission-track thermochronology: Implications for growth of the northeastern Tibetan Plateau margin: *Earth and Planetary Science Letters*, 248 (1-2), 198-208. Doi: 10.1016/j.epsl.2006.05.023.

Zhuang, G., Brandon, M. T., Pagani, M., & Krishnan, S. (2014), Leaf wax stable isotopes from Northern Tibetan Plateau: Implications for uplift and climate since 15 Ma: *Earth and Planetary Science Letters*, 390 (186-198. Doi: 10.1016/j.epsl.2014.01.003.

Zuza, A. V., Cheng, X., & Yin, A. (2016), Testing models of Tibetan Plateau formation with Cenozoic shortening estimates across the Qilian Shan–Nan Shan thrust belt: *Geosphere*, 12 (2), 501-532. Doi: 10.1130/ges01254.1.

Journal of Geophysical Research: Solid Earth

Supporting Information for

Reconciling the long-term growth of the Northeastern Tibetan Plateau and the upstream Yellow River profile

X. He[1], X. P. Yuan[1*], C. Q. He[2], X. Y. Wang[3], and X. M. Shen[4]

[1]Hubei Key Laboratory of Critical Zone Evolution, School of Earth Sciences, China University of Geosciences, Wuhan, China.

[2]Department of Earth, Atmospheric and Planetary Science, Massachusetts Institute of Technology, Cambridge, USA.

[3]School of Geography and Ocean Science, Nanjing University, Nanjing, China.

[4]National Institute of Natural Hazards, Ministry of Emergency Management of China, Beijing, China

Contents of this file

Introduction

This Supplementary Information contains two figures and three tables, supporting the analysis in the main text.

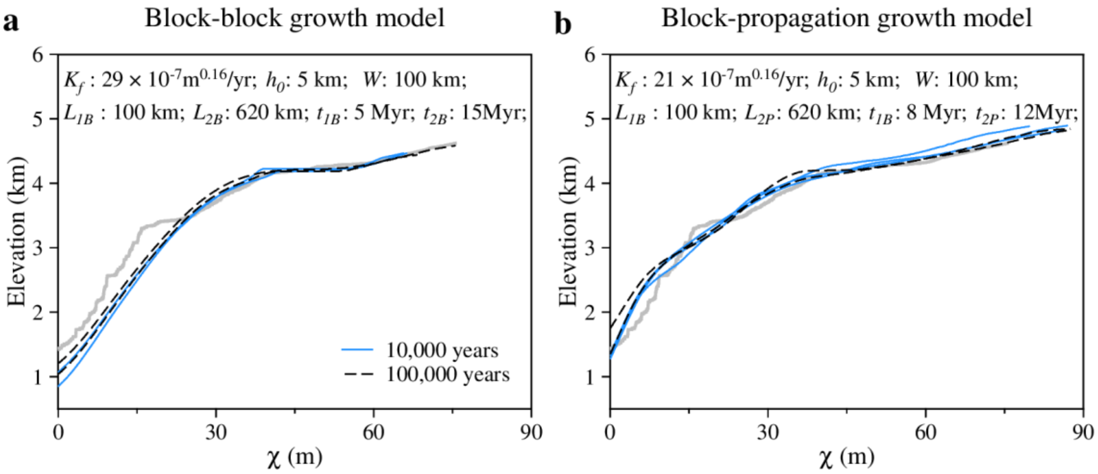

Figure S1. Comparison of χ from different time steps. (a) Block-block growth model. (b) Block-propagation growth model. The grey line is an observed river profile. The dashed lines are 100,000 years of a time step. The blue solid lines are 10,000 years of a time step. L_{1B} and t_{1B} are the distance and duration of the first block growth, respectively. L_{2B} and t_{2B} are the distance and duration of the second block growth, respectively. L_{2P} and t_{2P} are the distance and duration of the second propagation growth, respectively. River profiles resulting from different time steps are similar.

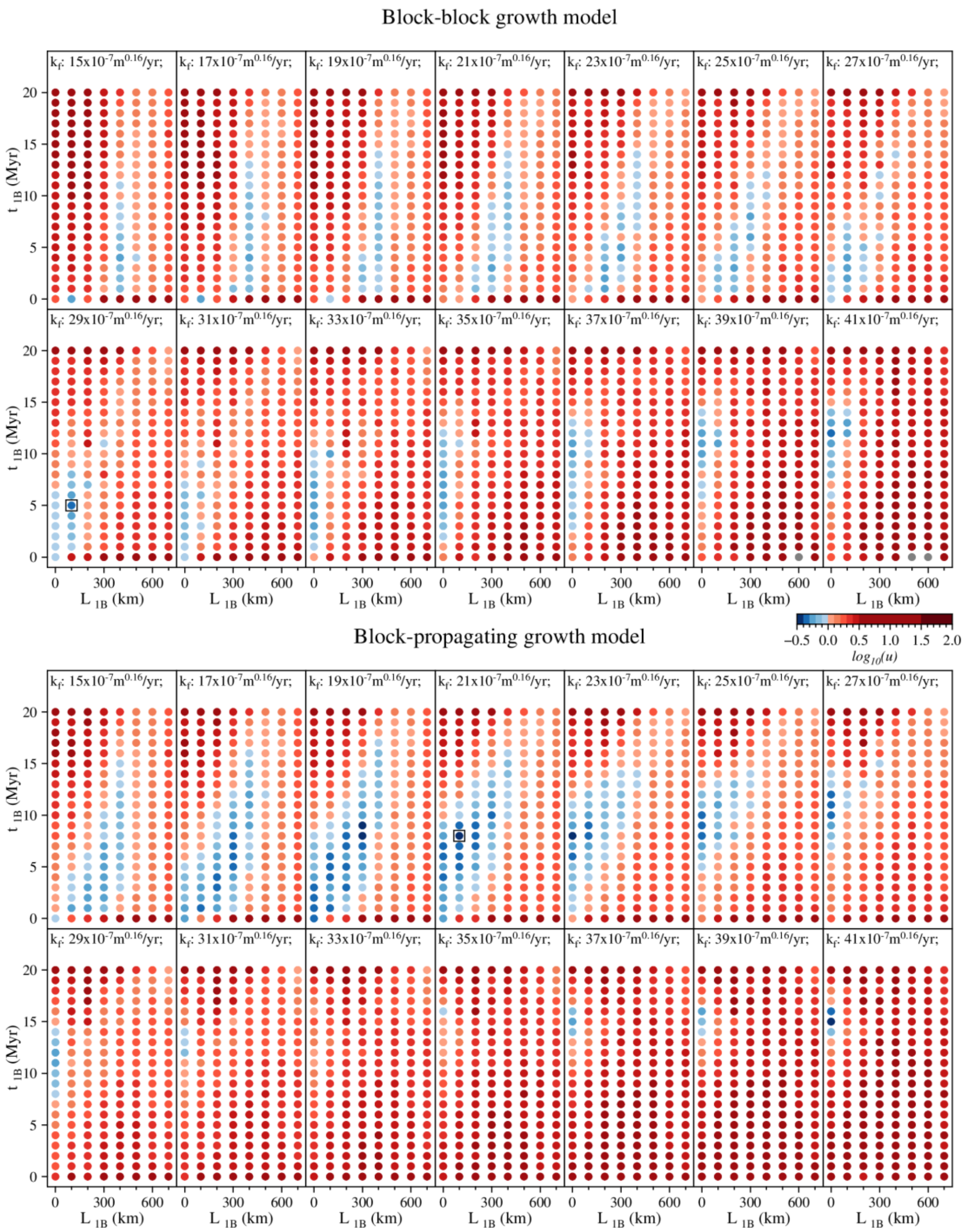

Figure S2. The detailed distribution of misfit $log_{10}(\mu)$ for three free parameters. In the block-block growth model. A black box marks one of the best-fit parameter sets (K_f = 29 × 10^{-7} $m^{0.16}$/yr, L_{1B} = 100 km, t_{1B} = 5 Myr), and the smallest $log_{10}(\mu)$ value is −0.335. In the block-propagation growth model. A black box marks one of the best-fit parameter sets (K_f = 21 × 10^{-7} $m^{0.16}$/yr, L_{1B} = 100 km, t_{1B} = 8 Myr), and the smallest $log_{10}(\mu)$ value is −0.439.

Table S1. A compilation of initial faulting ages.

Lat (°N)	Lon (°E)	Age (Ma)	Error	Data type	Reference
34.717	99.679	15.00	0.00	Thermochronometric ages	Duvall et al. (2013)
34.609	99.814	20.00	0.00		
34.094	101.508	6.50	1.50		
34.095	101.505	6.50	1.50		
34.096	101.502	6.50	1.50		
34.098	101.499	6.50	1.50		
34.103	101.497	6.50	1.50		
36.073	98.405	14.50	2.50		
36.071	98.407	14.50	2.50		
36.069	98.406	14.50	2.50		
36.066	98.406	14.50	2.50		
36.064	98.409	14.50	2.50		
36.256	98.472	14.50	2.50		
36.258	98.467	14.50	2.50		
36.254	98.460	14.50	2.50		
36.250	98.454	14.50	2.50		
36.248	98.450	14.50	2.50		
36.280	98.719	14.50	2.50		
36.277	98.712	14.50	2.50		
36.270	98.708	14.50	2.50		
36.267	98.711	14.50	2.50		
36.263	98.705	14.50	2.50		
35.856	98.769	14.50	2.50		
36.015	98.751	14.50	2.50		
35.992	98.566	14.50	2.50		
36.067	98.513	14.50	2.50		
37.401	101.902	12.41	1.50	Thermochronometric ages	Li et al. (2019)
37.580	101.839	11.68	1.94		
37.580	101.828	11.64	2.12		
37.611	101.832	10.96	2.07		
37.889	102.173	11.89	1.98		
35.666	106.229	8.06	1.02	Thermochronometric ages	Zheng et al. (2006)
35.670	106.230	8.16	0.90		
35.668	106.233	7.90	0.90		
35.670	106.235	7.30	1.10		
35.669	106.239	7.40	0.90		
36.300	105.200	~3.96	/	Stratigraphic relations	Zhang et al. (1991)
36.800	106.100	~3.96	/		
36.184	102.620	~22.00	/	Thermochronometric ages	Lease et al. (2011)
35.751	102.736	~13.00	/		
36.649	98.898	9.00	0.00	Fault signatures	Yuan et al. (2011)
36.641	98.903	9.00	0.00		
36.629	98.962	9.00	0.00		
37.103	100.686	10.00	3.00		
36.941	100.817	10.00	3.00		
37.100	98.267	12.50	2.50	Thermochronometric ages and fault signatures	Li et al. (2022)

Table S2. A compilation of thermochronometric ages (since 50 Ma).

Lat (°N)	Lon (°N)	Distance (km)	Height (km)	AHe (Age)	error	AFT (Age)	error	Acceleration time	Reference
102.611	36.178	561.76	3.45	21.80	1.90			23-17 Ma	Laji Shan (Lease et al., 2011)
102.620	36.184	562.80	3.27	22.70	2.40				
102.627	36.184	563.32	3.03	21.90	1.90				
102.631	36.184	563.62	2.92	22.60	1.90				
102.630	36.171	562.74	2.74	18.90	1.60				
102.633	36.171	562.96	2.58	17.60	1.30	37.80	3.80		
102.730	35.768	545.16	2.93	8.10	1.10	23.40	2.00	13-5 Ma	Jishi Shan (Lease et al., 2011)
102.736	35.769	545.67	2.74	9.10	1.20				
102.733	35.746	544.02	2.65	8.00	1.00				
102.738	35.767	545.70	2.60	7.90	1.00	14.00	2.60		
102.736	35.751	544.56	2.59	10.30	1.30				
102.739	35.766	545.71	2.55	8.30	1.10				
102.741	35.753	545.06	2.49	8.60	1.10				
102.744	35.757	545.53	2.40	7.20	0.90	18.10	1.20		
102.741	35.765	545.80	2.43	5.40	0.70	18.10	3.40		
102.743	35.763	545.83	2.39	5.40	0.80	18.30	3.40		
102.688	36.028	558.18	3.22	21.50	4.00				
102.709	36.028	559.75	3.03	18.90	2.70				
102.711	36.030	560.02	2.94	10.60	2.00				
101.508	34.094	348.01	4.43			15.80	3.40	8-5 Ma	East Kunlun (Duvall et al., 2013)
101.505	34.095	347.85	4.26			20.40	4.00		
101.502	34.096	347.68	4.09			9.60	2.30		
101.499	34.098	347.58	3.84			6.40	0.70		
101.497	34.103	347.75	3.66			8.70	2.60		
98.405	36.073	246.51	4.30	45.49	19.10			17-12 Ma	Dulan Chaka Highland (Duvall et al., 2013)
98.407	36.071	246.50	4.20	37.15	11.72				
98.406	36.069	246.29	4.09	15.20	2.96				
98.406	36.066	246.07	3.99	16.18	0.78				
98.409	36.064	246.13	3.87	12.70	1.09				
98.472	36.256	264.69	4.60	35.26	2.41				
98.467	36.258	264.52	4.47	26.81	5.95				
98.460	36.254	263.75	4.28	21.02	2.19				
98.454	36.250	263.06	4.10	13.88	2.17				
98.450	36.248	262.64	3.92	12.55	1.99				
98.719	36.280	282.91	4.81	45.22	8.95				
98.712	36.277	282.22	4.55	18.70	5.85				
98.711	36.267	281.42	4.33	14.16	4.11				
98.705	36.263	280.72	4.16	28.09	7.86				
101.908	37.714	605.84	3.01	40.90	7.60			15-12 Ma	East Qilian Shan (Wang et al., 2020)
101.909	37.711	605.73	2.86	12.90	1.00				
101.908	37.714	605.84	3.01	14.60	3.60				
101.919	37.712	606.52	2.62	38.60	13.40				
106.211	36.664	861.93	-4.80[a]			33.20	4.50	8-7Ma	Liupan Shan, (Zheng et al., 2006)
106.217	35.664	803.31	-5.60[a]			27.10	9.40		
106.229	35.666	804.35	-6.10[a]			8.06	1.02		
106.230	35.670	804.66	-6.11[a]			8.16	0.90		
106.233	35.668	804.77	-6.30[a]			7.90	0.90		
106.235	35.670	805.04	-6.40[a]			7.30	1.10		
106.239	35.669	805.29	-6.60[a]			7.40	0.90		

Note: AHe: Apatite (U-Th)/He; AFT: Apatite Fission Track. [a]Relative depth.

Table S3. A compilation of erosion rates.

Lat (°N)	Lon (°E)	Rate (mm/yr)	Error	Reference
36.700	99.700	0.01	0.00	Lal et al. (2004)
34.884	98.171	0.01	0.00	
33.820	97.149	0.02	0.00	Li et al. (2014)
35.891	99.694	0.11	0.01	
34.100	100.761	0.06	0.00	
34.898	100.885	0.06	0.01	
34.799	100.811	0.08	0.01	
34.797	100.811	0.08	0.01	Harkins et al. (2007)
34.777	100.813	0.08	0.01	
34.526	100.394	0.09	0.02	
34.752	99.693	0.11	0.01	
33.693	101.388	0.07	0.01	
34.598	101.341	0.06	0.01	
33.765	101.226	0.08	0.01	
33.724	101.271	0.07	0.01	Kirby and Harkins (2013)
34.557	99.481	0.06	0.01	
34.479	99.778	0.11	0.01	
34.689	100.623	0.23	0.02	
35.070	102.990	0.11	0.02	
35.120	102.130	0.08	0.01	
35.000	103.150	0.03	0.01	Zhang et al. (2017)
35.220	102.240	0.15	0.01	
35.310	102.790	0.32[a]	0.03	
35.400	102.870	0.33[a]	0.03	

Note: [a]Two high erosion rates are influenced by transient sediments.

References

Duvall, A. R., Clark, M. K., Kirby, E., Farley, K. A., Craddock, W. H., Li, C., & Yuan, D.-Y. (2013), Low-temperature thermochronometry along the Kunlun and Haiyuan Faults, NE Tibetan Plateau: Evidence for kinematic change during late-stage orogenesis: *Tectonics*, 32 (5), 1190-1211. Doi: 10.1002/tect.20072.

Harkins, N., Kirby, E., Heimsath, A., Robinson, R., & Reiser, U. (2007), Transient fluvial incision in the headwaters of the Yellow River, northeastern Tibet, China: *Journal of Geophysical Research: Earth Surface*, 112 (F3). Doi: 10.1029/2006JF000570.

Kirby, E., & Harkins, N. (2013), Distributed deformation around the eastern tip of the Kunlun fault: *International Journal of Earth Sciences*, 102 (7), 1759-1772. Doi: 10.1007/s00531-013-0872-x.

Lal, D., Harris, N. B. W., Sharma, K. K., Gu, Z., Ding, L., Liu, T., Dong, W., Caffee, M. W., & Jull, A. J. T. (2004), Erosion history of the Tibetan Plateau since the last interglacial: constraints from the first studies of cosmogenic 10Be from Tibetan bedrock: *Earth and Planetary Science Letters*, 217 (1), 33-42. Doi: 10.1016/S0012-821X(03)00600-9.

Lease, R. O., Burbank, D. W., Clark, M. K., Farley, K. A., Zheng, D., & Zhang, H. (2011), Middle Miocene reorganization of deformation along the northeastern Tibetan Plateau: *Geology*, 39 (4), 359-362. Doi: 10.1130/g31356.1.

Li, B., Chen, X., Zuza, A. V., Hu, D., Ding, W., Huang, P., & Xu, S. (2019), Cenozoic cooling history of the North Qilian Shan, northern Tibetan Plateau, and the initiation of the Haiyuan fault: Constraints from apatite- and zircon-fission track thermochronology: *Tectonophysics*, 751 (109-124. Doi: 10.1016/j.tecto.2018.12.005.

Li, B., Wang, Y., Zuza, A. V., Chen, X., Shao, Z., Wang, Z.-Z., Sun, Y., & Wu, C. (2022), Cenozoic deformation in the eastern domain of the North Qaidam thrust belt, northern Tibetan Plateau: *GSA Bulletin*, 135 (1-2), 331-350. Doi: 10.1130/b36215.1.

Li, Y., Li, D., Liu, G., Harbor, J., Caffee, M., & Stroeven, A. P. (2014), Patterns of landscape evolution on the central and northern Tibetan Plateau investigated using in-situ produced 10Be concentrations from river sediments: *Earth and Planetary Science Letters*, 398 (77-89. Doi: 10.1016/j.epsl.2014.04.045.

Wang, W., Zheng, D., Li, C., Wang, Y., Zhang, Z., Pang, J., Wang, Y., Yu, J., Wang, Y., Zheng, W., Zhang, H., & Zhang, P. (2020), Cenozoic Exhumation of the Qilian Shan in the Northeastern Tibetan Plateau: Evidence From Low-Temperature Thermochronology: *Tectonics*, 39 (4). Doi: 10.1029/2019tc005705.

Yuan, D. Y., Champagnac, J. D., Ge, W. P., Molnar, P., Zhang, P. Z., Zheng, W. J., Zhang, H. P., & Liu, X. W. (2011), Late Quaternary right-lateral slip rates of faults adjacent to the lake Qinghai, northeastern margin of the Tibetan Plateau: *Geological Society of America Bulletin*, 123 (9-10), 2016-2030. Doi: 10.1130/b30315.1.

Zhang, H., Kirby, E., Pitlick, J., Anderson, R. S., & Zhang, P. (2017), Characterizing the transient geomorphic response to base-level fall in the northeastern Tibetan Plateau: *Journal of Geophysical Research: Earth Surface*, 122 (2), 546-572. Doi: 10.1002/2015JF003715.

Zhang, P., Burchfiel, B. C., Molnar, P., Zhang, W., Jiao, D., Deng, Q., Wang, Y., Royden, L., & Song, F.

(1991), Amount and style of Late Cenozoic Deformation in the Liupan Shan Area, Ningxia Autonomous Region, China: *Tectonics*, 10 (6), 1111-1129. Doi: 10.1029/90TC02686.

Zheng, D., Zhang, P.-Z., Wan, J., Yuan, D., Li, C., Yin, G., Zhang, G., Wang, Z., Min, W., & Chen, J. (2006), Rapid exhumation at ~8 Ma on the Liupan Shan thrust fault from apatite fission-track thermochronology: Implications for growth of the northeastern Tibetan Plateau margin: *Earth and Planetary Science Letters*, 248 (1-2), 198-208. Doi: 10.1016/j.epsl.2006.05.023.